Jogundas Armaitis

HYDRODYNAMICS OF BOSE GASES
WITH INTERNAL DEGREES OF FREEDOM

2015

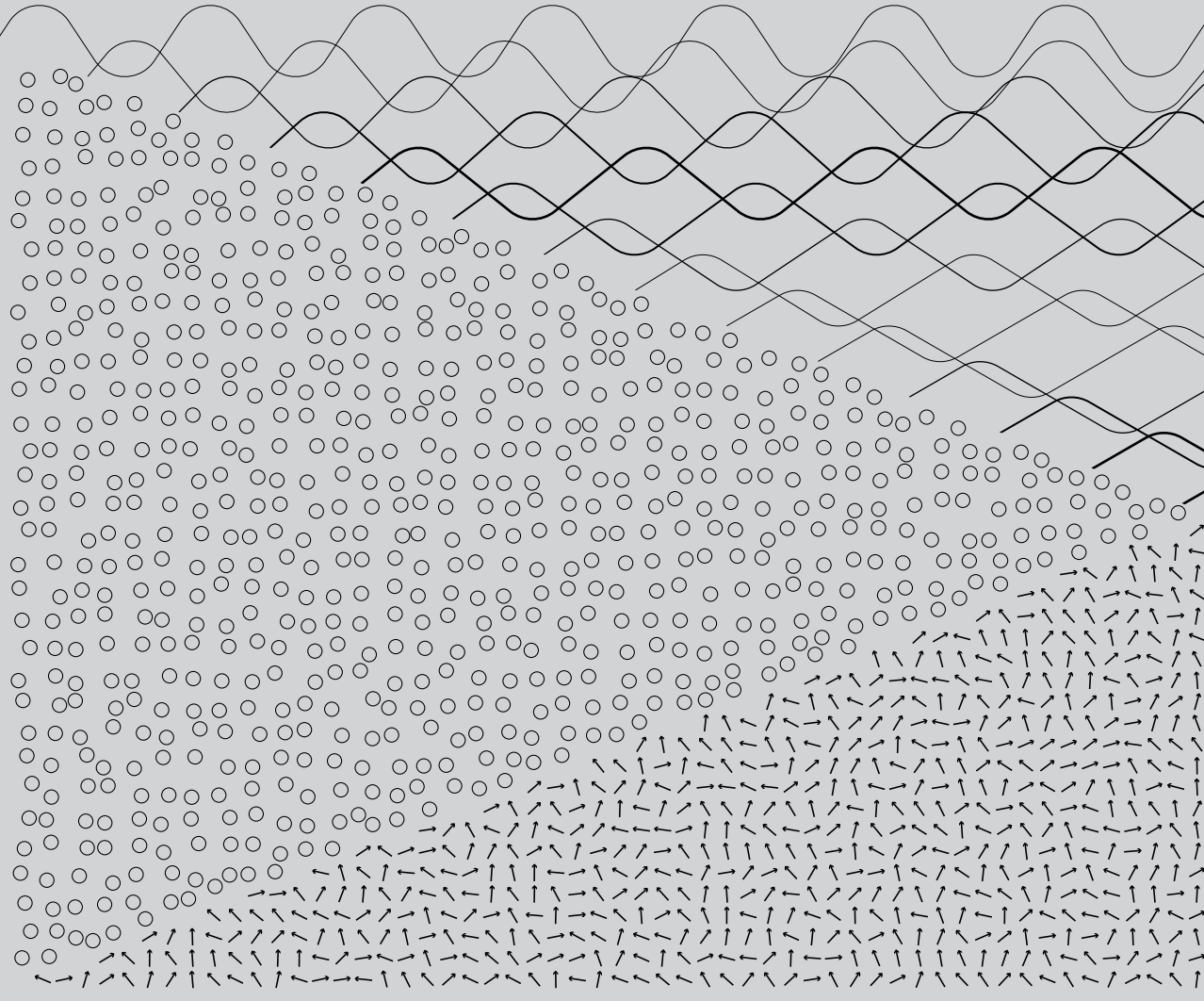

ISBN: 978-90-393-6338-6.
Cover design by Aurimas Baužys.
Printed by Ipskamp Drukkers, Enschede, The Netherlands.

Hydrodynamics of Bose gases with internal degrees of freedom

Hydrodynamische theorie voor Bose gassen met interne vrijheidsgraden

(met een samenvatting in het Nederlands)

Proefschrift

ter verkrijging van de graad van doctor aan de Universiteit Utrecht op gezag van de rector magnificus, prof. dr. G.J. van der Zwaan, ingevolge het besluit van het college voor promoties in het openbaar te verdedigen op woensdag 3 juni 2015 des middags te 2.30 uur

door

Jogundas Armaitis

geboren op 23 februari 1987 te Vilnius, Litouwen

PROMOTOR: Prof. dr. ir. H. T. C. Stoof
COPROMOTOR: Dr. R. A. Duine

This work is part of the research programme of the Foundation for Fundamental Research on Matter (FOM), which is part of the Netherlands Organisation for Scientific Research (NWO).

to L. Z.

CONTENTS

PUBLICATIONS

This thesis is partially based on the following papers:

- Chapter 2 is based on J. Armaitis, H. T. C. Stoof, and R. A. Duine, *Magnetization Relaxation and Geometric Forces in a Bose Ferromagnet*, Phys. Rev. Lett. 110, 260404 (2013), arXiv:1303.6791.
- Chapter 3 is based on J. Armaitis, H. T. C. Stoof, and R. A. Duine, *Hydrodynamic Modes of Partially-Condensed Bose Mixtures*, accepted for publication in Phys. Rev. A, arXiv:1502.03138.
- Chapter 5 is based on J. Armaitis, R. A. Duine, and H. T. C. Stoof, *Quantum Rotor Model for a Bose-Einstein Condensate of Dipolar Molecules*, Phys. Rev. Lett. 111, 215301 (2013), arXiv:1306.0398.

The author has also contributed to the following publication:

- J. E. Baarsma, J. Armaitis, R. A. Duine, and H. T. C. Stoof, *Polarons in Extremely Polarized Fermi Gases: The Strongly Interacting 6Li-40K Mixture*, Phys. Rev. A 85, 033631 (2012), arXiv:1110.3143.

1 INTRODUCTION

Just a couple decades ago bosonic low-temperature physics was synonymous with one particular liquid at a temperature of several degrees Kelvin. This liquid, helium-4, and its famous Helium-II phase, has revealed remarkable quantum properties such as quantized vortices and second sound [1, 2, 3, 4]. Yet, despite many things learned by investigating helium, its study has certain limitations. On the one hand, helium is a strongly interacting liquid, which makes first-principles theoretical research challenging. To name one example, establishing a connection between the non-interacting condensate state described by Bose and Einstein, and the helium properties observed in the lab took decades [5, 6, 7]. Furthermore, helium is a specific chemical element, and hence there is no surprise that its physical properties are fixed by nature. However, every particular chemical element has particular physical properties, so for a long time it seemed that it was as good as it gets.

The picture has changed drastically when the first Bose-Einstein condensate (BEC) was observed in an ultracold atomic gas. "Low temperature" has become synonymous with "ultracold", and the latter implies temperatures on the order of nanokelvins. Most strikingly, the relationship between what is fixed by nature and what is experimentally changeable has evolved. In particular, systems of different particle statistics, spin, and interactions have been engineered using ultracold vapours of various alkali atoms [4, 8]. This versatile manipulation not only makes emulating various condensed-matter physics models in a controlled system without impurities possible, but also opens a path towards novel phenomena that are at present not achievable in any other manner.

In order to understand the physical regime in which the ultracold-atom systems reside, it is useful to discuss some typical orders of magnitude of the physical quantities involved. The density of particles n in an ultracold-atom cloud is up to 10^{21} m^{-3}, which is around 10^5 times less dense than air (or 10^7 times less than helium). Therefore, the typical distance between atoms in an ultracold gas cloud is 100 nm. Since the thermal de Broglie wavelength of atoms at the typical temperature of 100 nK is 1 μm, their wave functions overlap substantially leading to quantum-degenerate behavior. Furthermore, the scattering between pairs of atoms is described by a short-range repulsion and a long-range attraction. This potential has a typical range of 10 nm, which is much less than both the inter-particle spacing and the de Broglie wavelength. A profound consequence of this last statement is that only s-wave (zero relative angular momentum) scattering is possible. Thus, the two-particle interaction is described by a single quantity (which depends on the specifics

of the aforementioned potential), the scattering length a. Though the scattering length can be artificially controlled using so-called Feshbach resonances [9, 10], its unaltered typical magnitude is 10 nm as well. Hence, the dimensionless number that expresses the strength of interactions, $n^{1/3}a \lesssim 0.1$, is much less than one, and the interactions are weak. All in all, a cloud of ultracold gas is a very sparse object, comprised of degenerate weakly interacting atoms scattering off each other in a simple manner.

1.1 INTERNAL DEGREES OF FREEDOM IN ULTRACOLD GAS: SPIN

Another important comparison to make is the one between the internal states of the atom and the thermal energy. Since we are interested primarily in alkali atoms, their single-particle state is fully described by electronic and hyperfine quantum numbers. However, since the distance between the ground state and the first excited electronic state is on the order of an electronvolt (eV), whereas the thermal energy is 100 nK $\simeq 10^{-11}$ eV, the electronic excitations cannot be generated by thermal means, even though they play an important role in laser trapping and other interactions with light. Contrary to that, hyperfine states within one multiplet are degenerate when no magnetic field is present, and are therefore populated equally by thermal excitations.

However, the occupancy of various hyperfine states can be engineered in a controlled manner. In order to achieve that, it is important that different hyperfine states respond to magnetic field differently: some are inert with respect to the magnetic field, while the energy of other states either increases or decreases with the magnetic field (Zeeman effect). These properties allow to exert different forces on different hyperfine states. In addition, introducing a finite magnetic field results in an energy gap between certain hyperfine states. Therefore, working in a sufficiently high magnetic field may limit the availability of the states accessible by thermal fluctuations to a single one. However, it is possible to transfer the atoms between non-degenerate hyperfine states by applying a radio-frequency (RF) pulse, since it resonantly couples the two hyperfine states. To sum up, depending on the experimental sequence used, it is possible to prepare diverse occupations of the hyperfine states.

An alternative way to think about the hyperfine state labels is imagining particles with an effective spin (or pseudospin). Indeed, this behavior has all the hallmarks of spin. When no magnetic field is present, the appropriate symmetry leaves the system invariant under rotations in the spin space. Moreover, the magnetic field induces the Zeeman splitting. Besides that, it is possible to introduce an artificial spin-orbit coupling by carefully coupling different hyperfine states through two-photon processes or magnetic field pulses that impart momentum to the atom. One difference of this effective spin as compared to the spin of the elementary particles is the missing connection between spin and statistics. In particular, an atom has its statistics

determined by the particles it is composed of. These particles (protons, neutrons, and electrons) also determine its total spin, which obviously satisfies the spin-statistics theorem. However, by populating only two hyperfine states and choosing a field configuration such that the other hyperfine states are virtually inaccessible to the dynamics of the system one can create an effective spin-1/2 Bose system.

1.2 SPIN-1/2 BOSE GAS

In order to make the preceding discussion more concrete, we will describe a spin-1/2 Bose gas with contact interactions in some detail in the mean-field approximation[1]. In particular, we will compute and discuss the phase diagram of this ferromagnetically coupled gas, since it is a simple system which nevertheless has two order parameters. During a ferromagnetic transition, rotational symmetry is spontaneously broken, and a preferred direction is chosen by the magnetization vector, which is the order parameter of the ferromagnetic phase. During the Bose-Einstein condensation, the phase symmetry of the wave function is spontaneously broken. The order parameter in this case is the expectation value of the annihilation operator, which, if it is nonzero, signals a macroscopic occupation of the ground state. The system can also occupy a paramagnetic normal phase, where both these order parameters are equal to zero: there is no magnetization, and none of the single-particle states are macroscopically occupied in the thermodynamic limit.

The action of this system is

$$S = \int_0^{\hbar\beta} d\tau \int d\boldsymbol{x} \Bigg[\sum_{\sigma=\uparrow,\downarrow} \phi_\sigma^* \left(\hbar\partial_\tau - \frac{\hbar^2 \boldsymbol{\nabla}^2}{2M} - \mu \right) \phi_\sigma + \sum_{\sigma=\uparrow,\downarrow} \frac{g_0}{4} \left(\phi_\sigma^* \phi_\sigma\right)^2 + \frac{g_2}{4} \left(\sum_{\sigma,\sigma'=\uparrow,\downarrow} \phi_\sigma^* \boldsymbol{\tau}_{\sigma\sigma'} \cdot \boldsymbol{\Omega} \phi_{\sigma'} \right)^2 \Bigg], \tag{1.1}$$

where ϕ_σ is the bosonic field with the spin σ evaluated at position $\boldsymbol{x}$ and at imaginary time τ, $\boldsymbol{\tau}$ is a vector of the Pauli matrices, M is the mass of a particle, and μ is the chemical potential. Note that the chemical potential in a non-interacting bosonic system can only be negative or zero, as opposed to a fermionic system, where the chemical potential is positive at low temperatures. The constants $g_0 = 4\pi\hbar^2 a_0/M$ and $g_2 = -4\pi\hbar^2 a/M$ are known as the T matrices (even though they are real numbers in this case) and define the two types of interactions present in the system. As discussed earlier, the s-wave scattering lengths a and a_0 determine the interaction strengths. We limit ourselves to the ferromagnetic case $a > 0$ with the other interaction being repulsive $a_0 > 0$ in this discussion. In order to treat these interaction

1 A similar treatment was presented in Ref. [11].

terms, we perform two Hubbard-Stratonivich transformations, introducing new fields with the following averages

$$\langle \boldsymbol{m} \rangle = \langle m\boldsymbol{\Omega} \rangle = \sum_{\sigma,\sigma'=\uparrow,\downarrow} \langle \phi^*_\sigma \boldsymbol{\tau}_{\sigma\sigma'} \phi_{\sigma'} \rangle / 2, \tag{1.2}$$

$$\langle n \rangle = \sum_{\sigma=\uparrow,\downarrow} \langle \phi^*_\sigma \phi_\sigma \rangle, \tag{1.3}$$

where the first field is the magnetization, and the second field is the total particle density. Furthermore, from now on we consider only the average values of $\boldsymbol{m}$ and n for simplicity, and neglect their fluctuations. Since we are working in a homogeneous space, we will assume that these averages are constant in space and time, which still is an approximation. After the transformation, the action in momentum space becomes

$$S = \sum_{\boldsymbol{k},n} \left[(-i\hbar\omega_n + \varepsilon_{\boldsymbol{k}} - \mu + g_0 n/2) \sum_{\sigma=\uparrow,\downarrow} \phi^*_\sigma \phi_\sigma + \sum_{\sigma,\sigma'=\uparrow,\downarrow} g_2 \boldsymbol{m} \cdot \boldsymbol{\tau}_{\sigma\sigma'} \phi^*_\sigma \phi_{\sigma'} \right] - \hbar\beta V (g_0 n^2/4 + g_2 \boldsymbol{m}^2), \tag{1.4}$$

where ϕ_σ is now the Fourier-transformed field which is thus evaluated at the momentum $\hbar\boldsymbol{k}$ and the bosonic Matsubara frequency $\omega_n = 2\pi n/\hbar\beta$. Moreover, $\varepsilon_{\boldsymbol{k}} = \hbar^2\boldsymbol{k}^2/2M$ is the kinetic energy, $\beta = 1/k_B T$ is the inverse energy associated with the temperature T, and k_B is Boltzmann's constant.

For our purposes it will suffice to consider the terms containing the fields ϕ_σ. We therefore neglect the last two terms in the action, since they correspond to a shift in energy. Hence, the term $\sum_{\sigma=\uparrow,\downarrow} g_0 n \phi^*_\sigma \phi_\sigma / 2$ merely shifts the chemical potential by an amount that is equal for the two spin species. Therefore, we account for this term by redefining the chemical potential

$$\mu - g_0 n/2 \to \mu. \tag{1.5}$$

By defining a vector of bosonic operators

$$\boldsymbol{\phi} = (\phi_\uparrow, \phi_\downarrow), \tag{1.6}$$

and its conjugate, we can write the action in a convenient matrix form:

$$S = \sum_{\boldsymbol{k},n} \boldsymbol{\phi}^\dagger \cdot \begin{pmatrix} -i\hbar\omega_n + \varepsilon_{\boldsymbol{k}} - \mu + g_2 m_z & g_2(m_x - i m_y) \\ g_2(m_x + i m_y) & -i\hbar\omega_n + \varepsilon_{\boldsymbol{k}} - \mu - g_2 m_z \end{pmatrix} \cdot \boldsymbol{\phi}. \tag{1.7}$$

Since the matrix in the action is the interacting inverse Green's function, i.e.,

$$S = -\hbar \sum_{\boldsymbol{k},n} \boldsymbol{\phi}^\dagger \cdot \boldsymbol{G}^{-1} \cdot \boldsymbol{\phi}, \tag{1.8}$$

it is instructive to separate the free part from the part due to the interactions:

$$-\hbar \boldsymbol{G}^{-1} = -\hbar \boldsymbol{G}_0^{-1} + \hbar \boldsymbol{\Sigma}, \tag{1.9}$$

where the inverse non-interacting Green's function is

$$-\hbar \boldsymbol{G}_0^{-1} = (-i\hbar\omega_n + \varepsilon_{\boldsymbol{k}} - \mu) \begin{pmatrix} 1 & 0 \\ 0 & 1 \end{pmatrix}, \tag{1.10}$$

and the self energy is

$$\hbar\boldsymbol{\Sigma} = \begin{pmatrix} g_2 m_z & g_2(m_x - i m_y) \\ g_2(m_x + i m_y) & -g_2 m_z \end{pmatrix}. \tag{1.11}$$

The action can be diagonalized by a rotation $\boldsymbol{R}$ in spin space which brings us to a coordinate system where the magnetization points along the z axis:

$$\boldsymbol{\psi} = \boldsymbol{R} \cdot \boldsymbol{\phi} = (\psi_+, \psi_-), \tag{1.12}$$

where ψ_σ are the new bosonic fields. In terms of these fields, the action becomes

$$S = \sum_{\sigma=\pm} \sum_{\boldsymbol{k},n} (-i\hbar\omega_n + \varepsilon_{\boldsymbol{k}} - \mu + \sigma g_2 m) \psi_\sigma^\dagger \psi_\sigma, \tag{1.13}$$

where $m \equiv |\boldsymbol{m}|$ is the length of the magnetization vector. We see that as a result of this mean-field procedure the magnetic interaction has introduced an energy difference of $2g_2 m$ between the two spin species. However, the new bosonic fields ψ_σ are now decoupled, so we can perform the Matsubara sum and obtain the densities

$$n_\sigma = \frac{1}{V} \sum_{\boldsymbol{k}} \langle \psi_\sigma^\dagger \psi_\sigma \rangle = \frac{1}{V} \sum_{\boldsymbol{k} \neq 0} \left[e^{\beta(\varepsilon_{\boldsymbol{k}} - \mu + \sigma g_2 m)} - 1 \right]^{-1} + n_\sigma^c, \tag{1.14}$$

where $n_\pm^c$ is the condensate density. The total density is simply the sum of the densities of the two components:

$$n = n_+ + n_-, \tag{1.15}$$

while the magnetization is equal to one half of their difference:

$$m = (n_+ - n_-)/2 \geq 0. \tag{1.16}$$

Above the condensation temperature T_{BEC}, there are no condensed atoms ($n_\sigma^c = 0$) by definition. In that case, the densities of the two species become

$$n_\sigma \Lambda^3 = \mathrm{Li}_{3/2}\left(\exp[\beta\mu - \beta\sigma g_2 m]\right), \tag{1.17}$$

where we have introduced the thermal de Broglie wavelength $\Lambda^2 = 2\pi\hbar^2\beta/M$ and a polylogarithm function $\mathrm{Li}_s(z)$ which is defined as $\mathrm{Li}_s(z) = \sum_{x=1}^{\infty} z^x / x^s$. We also define the dimensionless density $\bar{n} = n\Lambda^3$, the dimensionless magnetization $\bar{m} = m\Lambda^3$, and the dimensionless chemical potential $\bar{\mu} = \beta\mu$. These

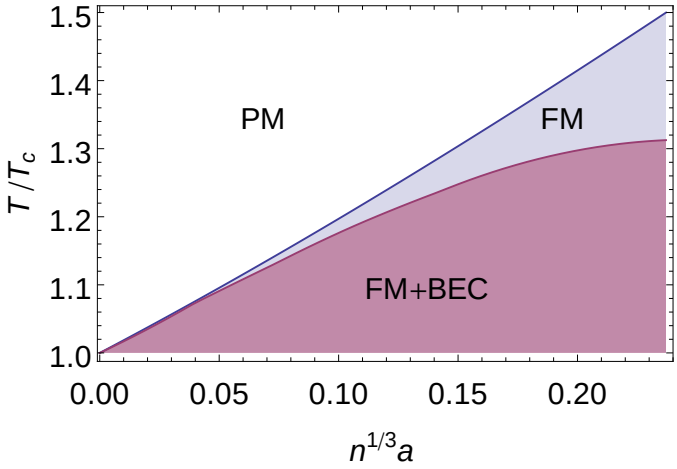

FIGURE 1: Phase diagram of the spin-1/2 Bose gas with a ferromagnetic coupling in terms of the temperature and the interaction strength. The temperature axis is scaled with the Bose-Einstein condensation temperature of the non-interacting gas. The white area is the paramagnetic (PM) phase, the light blue region is the ferromagnetic (FM) phase, and the dark purple zone is the ferromagnetic phase with the Bose-Einstein condensate (FM+BEC).

definitions allow us to rewrite the density equations in a manner suitable for numerical solution:

$$\bar{n} \pm 2\bar{m} = 2\,\mathrm{Li}_{3/2}\left(\exp[\bar{\mu} \pm 2(a/\Lambda)\bar{m}]\right). \tag{1.18}$$

Hence, fixing the density n and the temperature T, we can solve these two equations for the chemical potential μ and the magnetization m. In turn, this procedure allows us to find the phase diagram of the system (see Fig. 1), since the ferromagnetic order is signaled by $m > 0$, and the Bose-Einstein condensation occurs when

$$\mu - g_2 m = 0, \tag{1.19}$$

which is equal to $\bar{\mu} + 2(a/\Lambda)\bar{m} = 0$ in dimensionless units, and equivalent to the familiar condition $\mu = 0$ for the non-interacting Bose gas[2] .

It is immediately clear that nonzero magnetization increases the condensation temperature, as the critical chemical potential is lowered, compared to the non-interacting gas. On the other hand, the Eqns. (1.18) always have a solution with a non-zero magnetization in some temperature range above the condensation temperature. Hence, the ferromagnetic transition always occurs at a temperature higher than the condensation temperature, therefore

2 Note that in terms of the real chemical potential, the condensation condition is $\mu - g_0 n/2 - g_2 m = 0$.

validating our approach to the problem (as we assumed no condensate when solving the equations in question).

Furthermore, only one of the two components (+) can form a condensate in this system, since the other species (−) condenses at a chemical potential of $\mu = -g_2 m$, which would imply at an effective chemical potential of $-2g_2 m > 0$ for the + species, that is positive and therefore impossible.

Also note that the phase diagram that we have found is qualitatively similar to the phase diagrams of certain solid-state materials, known as the ferromagnetic superconductors [12]. These materials display both superconductivity and ferromagnetism, just like the Bose gas considered here, albeit the atoms are neutral so they are superfluid rather than superconducting. However, there are important differences, too. For example, the relevant Bose-condensed particles in the superconducting materials are the Cooper pairs, and not atoms. Nevertheless, studing the Bose ferromagnet might provide some insights into the physics of the ferromagnetic superconductors. The system of spin-1/2 bosons and its phases are further studied in the Chapters 2, 3 and 4 of this thesis.

1.3 EXPERIMENTAL STATUS

One of the goals of the theoretical work presented in this thesis is to motivate and give predictions for present and future experiments. Therefore, for the sake of understanding what is possible in the experimental realm, we discuss two experiments in this section. Since many experiments have been performed with various Bose gases, the choice is somewhat arbitrary, and, obviously, not exhaustive. However, these two particular experiments illustrate the key concepts permeating this thesis: symmetry breaking and ultracold vapor hydrodynamics.

1.3.1 *Spontaneous symmetry breaking in an experiment*

Different phases and phase diagrams play a central role in this thesis, therefore, it is useful to understand how spontaneous symmetry breaking looks in the lab. One illustration of this process was provided by the Berkeley group [13]. They prepared approximately one million rubidium (^{87}Rb) atoms in an anisotropic harmonic trap, resulting in a disk-shaped cloud with the dimensions of $1\mu\text{m} \times 10\mu\text{m} \times 100\mu\text{m}$. Since the spin healing length was $\xi = \sqrt{\hbar^2/2m|g_2|n_0} \simeq 1\mu\text{m}$, where $n_0 \simeq 10^{20} m^{-3}$ was the peak density, the strong anisotropy of the cloud confined the spin dynamics to only two directions, and therefore allowed direct imaging of all three magnetization components in the whole system by non-destructive optical means. The temperature of the cloud during the experiment was 40 nK, therefore resulting in a nearly pure BEC. Rubidium has three states (spin-1) in its lowest hyperfine manifold.

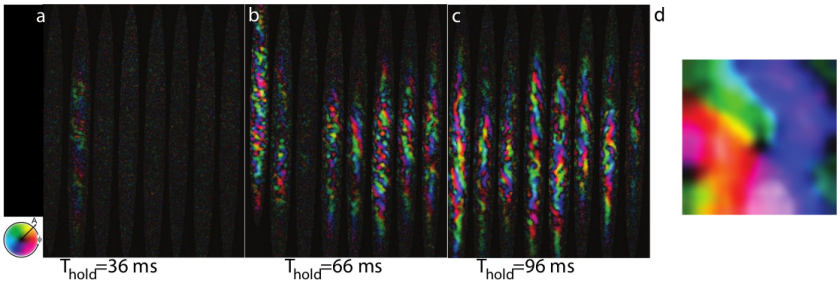

FIGURE 2: Transverse magnetization imaged at different hold times after the quench (a) – (c), where the brightness shows the magnitude of the transverse magnetization, and the hue shows its direction, as indicated by the color wheel in the left bottom corner. Parallel images at the same hold time show different realizations of the experiment. Spin vortices with winding number one (d) often appear after the quench. Images taken from Ref. [14].

Since an optical dipole trap was used, all the spin states were trapped equally, and no imbalance between them was introduced that way, as opposed to a magnetic trap.

The spin-dependent interaction in rubidium has the same ferromagnetic character as the one we described in the previous chapter. Hence, at zero temperature and no magnetic field, the ground state of the system is a ferromagnetic condensate. However, in addition to the optical trap, an external magnetic field was applied. The interaction with the magnetic field in rubidium (Zeeman effect) is such, that in a high magnetic field the rotational spin symmetry in the transverse spin plane is unbroken, and thus no magnetization transverse to the magnetic field develops. Therefore, by preparing the sample in a high magnetic field, and then suddenly switching (quenching) the magnetic field off, the experimentalists were able to observe a spontaneous symmetry breaking event as the system developed a non-zero transverse magnetization.

Several observations hint that a phase transition driven by quantum fluctuations occurred in this experiment. Immediately after the quench, no transverse magnetization was observed, since it was below the experimental threshold. However, in a phase transition driven by quantum fluctuations, the exponential growth of the fluctuations should proceed after the quench with a characteristic instability timescale of $\tau = \hbar/\sqrt{2|g_2|\langle n\rangle}$, where $\langle n\rangle$ is an appropriate average of the particle density in the system. It turns out that this number is on the order of 10 ms, and indeed the first finite magnetization was observed on a similar timescale (Fig. 2 (a) – (c)). Furthermore, domains with different transverse magnetization arose with unmagnetized domain walls between them. The typical initial size of the domains was also in a good agreement with the instability length $l = \sqrt{\hbar^2\pi^2/2m|g_2|\langle n\rangle} \simeq 10\mu$m. Since the domain walls are not topologically protected in this system, they are sup-

posed to decay through vortex formation. Indeed, multiple spin vortices with an integer winding number were observed (see Fig. 2 (d) for an example). The typical size of the core of the vortex in the experiment was approximately equal to the spin healing length.

To sum up, a quantum-fluctuation-driven phase transition to the ferromagnetic BEC was observed in the Berkeley experiment. Furthermore, magnetic domain walls and spin vortices were observed. Finally, typical times and sizes of these objects matched well the appropriate quantities from the simple Hamiltonian of the spinful Bose gas.

1.3.2 *Hydrodynamic vapor in an experiment*

At first sight the combination of words "hydrodynamic vapor" might sound as an oxymoron. The word "hydrodynamic" seems to refer to liquids, while vapor (or gas) is definitively distinct from a liquid. Intuitively, gas seems to be a form of matter where particles collide rather rarely, whereas in liquids local equilibrium is always promptly established by frequent interactions. However, it turns out that in an ultracold gas it is possible to continuously tune the system from the situation where the particles rarely ever collide (the collisionless regime), to the one where collisions are frequent (the hydrodynamic regime). This controlled transition was described in a series of experiments by the Utrecht group [15, 16, 17, 18].

In order to increase the frequency of interactions, reducing the dimensionality of the system and increasing its density looks promising. The former is achieved by creating a highly anisotropic trap, and the latter can be done by loading more atoms into the trap. In the simplest case, such a trap has a cylindrical symmetry. This cigar-shaped trap is described by a shallow axial potential and a steep radial potential. However, a more narrow radial confinement and a higher density of particles also leads to increased three-body losses. Three-body losses result from collisions of three particles, as opposed to the usual collisions where only two particles participate. This is important, since in a three-particle collision two particles may form a molecule, and the third particle carries away the binding energy by escaping the trap. Even worse, in a sample where collisions are frequent, the energetic particle may hit other particles and start an avalanche, resulting in a rapid depletion of the cloud. Therefore, three-body losses decrease the effective density, limiting the frequency of collisions.

A three-body collision requires three atoms to be present at the same position, an event which is quantified by the three-particle correlation function G_3. Three-particle correlations typically scale with the density to the third power ($G_3 \sim n^3$). However, it turns out that the presence of a Bose-Einstein condensate suppresses these correlations [19, 4]. Hence, by cooling down a relatively low-density cloud to the condensation temperature, and then com-

pressing it to increase the density, prevents the three-body losses, and allows achieving the deep hydrodynamic regime.

In order to quantify how hydrodynamic the cloud is, it is convenient to introduce the dimensionless hydrodynamicity $\tilde{\gamma}$. In the case of a highly anisotropic trap, this quantity is defined by a ratio of the collision rate γ and the weakest trapping frequency ω (which defines the longest trap axis): $\tilde{\gamma} = \gamma/\omega$. Note that $\tilde{\gamma}$ describes the hydrodynamicity only in the longest (axial) direction of the sample, and the motion in the other directions stays collisionless. The collision rate $\gamma = nv\sigma$ is in turn defined as a product of the appropriate particle density n, the average relative velocity of two particles v and the collision cross-section $\sigma = 8\pi a^2$, where a is the s-wave scattering length that has already been discussed. Most of the ultracold atom experiments, including the Berkeley experiment described in the previous subsection, operate in the collisionless regime $\tilde{\gamma} \ll 1$. Physically, this means that the mean free path is larger than the size of the sample. In other words, while an atom travels from one end of the trap to the other, it experiences less than one collision on average.

In contrast to a typical ultracold gas experiment, in the Utrecht experiment the hydrodynamicity is much more than one: $\tilde{\gamma} \simeq 10$. That is to say, an atom collides almost ten times before reaching the opposite side of the trap. This high hydrodynamicity is achieved by loading almost a billion ultracold sodium atoms into the trap. The radial frequency of the trap is $\omega_r \simeq 2\pi \times 100$ Hz, while the axial frequency is $\omega_a \simeq 2\pi \times 1$ Hz. The peak density of the cloud is almost $10^{21}\mathrm{m}^{-3}$, which results in a collision rate of $\gamma \simeq 100$ Hz. The sample is extremely anisotropic, as the length of the cloud is more than a millimeter, whereas its radius is on the order of tens of microns.

One way to illustrate that the gas kinetics strongly depends on the hydrodynamicity is investigating the heat flow. By shining a laser beam with a small radius (much smaller than the axial size of the cloud) on one end of the cloud, a lump of hot atoms is created. Thus, a thermal gradient across the cloud arises. The time evolution of the temperature profile depends on the kinetics of the gas. In this particular experiment, the gas is slightly above the condensation temperature, while the lifetime (limited by the three-body decay) of the cloud is around one minute even at the highest hydrodynamicity. Since the relevant thermal dynamics occurs at the timescales of one second, the lifetime of the cloud is fully sufficient to observe the effects in question.

In particular, close to the collisionless regime ($\tilde{\gamma} \simeq 1$, Fig. 3 a) the lump of the hot atoms rocks from one end of the trap to the other a couple of times with the frequency of the trap. The damping of this motion comes from the fact that the system is not fully collisionless, and the lump of hot atoms eventually reaches thermal equilibrium with the rest of the system. As hydrodynamicity of the system is increased, the damping of this thermal dipole mode increases with it, and the frequency of the motion eventually reaches zero ($\tilde{\gamma} \simeq 3$, Fig. 3 b). In this critically damped regime the oscilla-

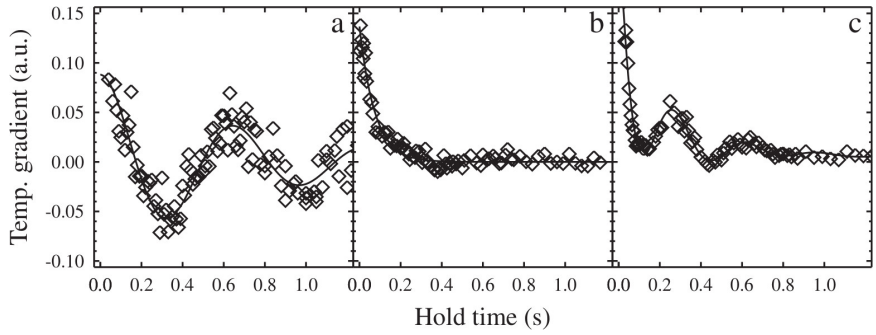

FIGURE 3: Temperature gradient imaged at different hold times for three values of the hydrodynamicity: $\tilde{\gamma} \simeq 1$ (a), $\tilde{\gamma} \simeq 3$ (b), and $\tilde{\gamma} \simeq 7.5$ (c). Figure taken from Ref. [16].

tion ceases, signaling the onset of the diffusive thermal transport. Here, due to frequent collisions the lump of the hot atoms thermalizes with its neighbors before it reaches the opposite end of the trap. Finally, increasing the hydrodynamicity even further ($\tilde{\gamma} \simeq 7.5$, Fig. 3 c) results in an even faster (double-exponential) initial decay of the temperature gradient. Furthermore, for later times a hydrodynamic standing-wave sound mode is excited in this particular experiment. The frequency of this mode is distinct from the trap frequency, and this mode is only available in the hydrodynamic regime.

Therefore, the Utrecht group was able to tune an ultracold gas from the (usual) collisionless regime to the (novel) hydrodynamic regime in the long (axial) direction of the trap, even in the absence of the condensate. These different regimes were illustrated by distinct thermal dynamics. The ability to achieve the hydrodynamic regime in the spinless Bose gas has opened the path towards exploring hydrodynamic modes and their interplay with other well-controlled aspects of the ultracold gas, such as spin, temperature, and interactions.

1.4 DIPOLE MOMENT: A DIFFERENT KIND OF INTERNAL DEGREE OF FREEDOM

The only kind of internal degrees of freedom discussed so far were the hyperfine states of the atom, or (pseudo)spin. However, there also exists a possibility to consider dipolar degrees of freedom. They are important in atoms with a large magnetic moment (magnetic dipoles), e.g., chromium and dysprosium, and in molecules (electric dipoles). In these systems, each particle possesses an anisotropic charge distribution, resulting in a dipole-dipole interaction between the dipolar particles. Theoretical study of these systems is in part motivated by the recent progress in the field of ultracold molecules and by the observation of the Bose-Einstein condensates of several species of atoms with large magnetic moments.

Arguably, the most pronounced theoretical difference between spinful systems and systems with the (non-magnetic) dipolar degrees of freedom is the absence of time-reversal symmetry in the former. However, other important differences exist, too. In particular, the dipole-dipole interaction is the only long-range interaction between neutral particles which cannot be replaced by a contact pseudopotential even at ultracold temperatures. Furthermore, the dipole-dipole interaction is anisotropic. Perhaps unsurprisingly, these remarkable features are also apparent in many-body properties of dipolar systems.

In the realm of classical physics, several interesting effects due to dipolar interactions have been discussed and observed. One such example is the melting of two-dimensional (2D) crystals of particles with dipole-dipole interactions. Experimentally, it has been observed using colloidal particles with radii of the order of microns confined to the water-air interface [20]. It turns out that these crystals melt through an intermediate phase with a long-range orientational order but only short-range translational order (the hexatic phase). The process of melting can be explained through the formation and unbinding of topological defects, in a manner similar to the Kosterlitz-Thouless-Berezinski theory [8] of the superfluid to normal transition in 2D. Even though the first theoretical steps have already been taken in studying the quantum version of the two-dimensional dipolar-crystal theory [21], quantum counterparts of many other effects have remained largely unexplored.

On the other hand, some fascinating quantum phenomena have already been investigated using ultracold dipolar gases. In particular, experiments with ultracold molecules have allowed researchers to observe tunneling-driven (as opposed to thermally-activated) chemical reactions [22], as well as direction-dependent reactions [23], where the reaction rate was suppressed by almost two orders of magnitude as the molecules approached each other only "side-by-side". Our work on the quantum-fluctuation disordered ferroelectric in a dipolar BEC (Chapter 5) proceeds along a similar line of thought, describing a system with no classical analog.

1.5 OUTLINE

In the chapters that follow, the ideas touched upon in the introduction are developed in more detail. In Chapter 2 we develop a hydrodynamic description of the ferromagnetic spin-1/2 Bose gas at arbitrary temperatures. We study magnetization relaxation and geometric forces. In particular, we consider the topological Hall effect due to the presence of a skyrmion[3]. In Chapter 3 we investigate the miscible (non-ferromagnetic) spin-1/2 Bose gas at arbitrary temperatures, construct its hydrodynamic description, calculate the thermodynamic properties, and study the collective modes of this system. In

3 This effect was shortly thereafter observed experimentally by the Seoul group [24].

Chapter 4 we discuss the influence of the off-diagonal Berry curvature on the Bose-Einstein condensation temperature. Finally, in Chapter 5 we study a Bose-Einstein condensate of dipolar molecules in a weak electric field and find it to be described by a quantum rotor model. Moreover, we show that the molecular Bose-Einstein condensate is a ferroelectric material that is fully disordered by quantum fluctuations.

2

MAGNETIZATION RELAXATION AND GEOMETRIC FORCES IN A BOSE FERROMAGNET

We construct the hydrodynamic theory for spin-1/2 Bose gases at arbitrary temperatures[1]. This theory describes the coupling between the magnetization, and the normal and superfluid components of the gas. In particular, our theory contains the geometric forces on the particles that arise from their spin's adiabatic following of the magnetization texture. The phenomenological parameters of the hydrodynamic theory are calculated in the Bogoliubov approximation and using the Boltzmann equation in the relaxation-time approximation. We consider the topological Hall effect due to the presence of a skyrmion, and show that this effect manifests itself in the collective modes of the system. The dissipative coupling between the magnetization and the normal component is shown to give rise to magnetization relaxation that is fourth order in spatial gradients of the magnetization direction.

2.1 INTRODUCTION

Geometric forces are abundant in virtually all areas of physics, from the classical conical pendulum [25] to a single quantum spin [26]. In particular after the advent of the Berry phase [27], a large number of manifestations of geometric forces, including the optical Magnus effect [28], the topological Hall effect [29, 30] and geometric forces due to synthetic gauge fields [31] have been predicted and observed.

In metallic ferromagnets, magnetization dynamics leads to forces on quasiparticles of geometric origin called spin motive forces, that have gained considerable attention recently [32, 33, 34, 35, 36]. Furthermore, spin textures with nonzero chirality, such as the skyrmion lattice observed recently [37, 38] induce the so-called topological Hall effect [29, 30]. In addition, the coupling between magnetization and quasiparticles has also been shown to give rise to novel forms of magnetization relaxation in this case. A prominent example is inhomogeneous Gilbert damping [39, 40, 41]. This effect is important in clean solid-state systems. We therefore expect these effects to be particularly important for gases of ultracold atoms, that, in contrast to conventional condensed-matter systems, are free of impurities.

The field of ultracold atoms is characterised by exquisite experimental control [42, 43, 10]. Relevant for our focus is the great amount of recent activity on spinor Bose gases. Firstly, it has been discovered that these gases can be ei-

1 This chapter is directly based on J. Armaitis, H. T. C. Stoof, and R. A. Duine, *Magnetization Relaxation and Geometric Forces in a Bose Ferromagnet*, Phys. Rev. Lett. 110, 260404 (2013).

ther ferromagnetic or antiferromagnetic depending on the details of the scattering lengths [44, 45]. Furthermore, numerous studies at zero temperature, based on the Gross-Pitaevskii equation, have elucidated the long-wavelength properties of spinor gases [46, 47]. Other areas of current interest in the field include topological excitations, magnetic dipole-dipole interactions and non-equilibrium quantum dynamics [48]. The recent progress in the understanding of ferromagnetic spinor gases and their manipulation by light has also enabled detailed studies of magnetization dynamics [13, 49].

Despite these activities, a theory that describes simultaneously all phases of ferromagnetic spinor Bose gases and includes both geometric and dissipative coupling between superfluid, ferromagnetic order parameter and quasiparticles is lacking. The purpose of this chapter is to put forward such a theory. This theory is needed to determine properties of collective modes at arbitrary temperatures that consist of combined dynamics of the ferromagnetic and superfluid order with the normal component of the gas. These results can e.g. be used to detect the presence of skyrmions and their dynamics in the gas. We choose to work in the hydrodynamic regime, where the coupling between the magnetization, and the normal and superfluid components of the gas is controlled by a gradient expansion. This approach is valid in the regime where local equilibrium is enforced by frequent collisions. In addition, we make a connection between long-wavelength and microscopic physics by calculating all the hydrodynamic parameters from first principles. In the microscopic determination of the parameters, we focus on the spin-1/2 case leaving higher spin for future work.

2.2 HYDRODYNAMIC EQUATIONS

Describing a ferromagnetic Bose gas requires considering three phases: unpolarized normal fluid, normal ferromagnet and superfluid ferromagnet. These three phases have different sets of relevant hydrodynamic variables, that have to be taken into account in order to fully describe the behavior of the system. A complete set of relevant variables includes the order parameters and the conserved quantities. The order parameters of a homogeneous Bose ferromagnet are the superfluid velocity $\boldsymbol{v}_s$ and the magnetization density $Pn\Omega^\alpha$. Here P is the polarization, and Ω^α is the dimensionless magnetization direction, normalized such that $\Omega^\alpha\Omega^\alpha = 1$. (We use the Einstein summation convention throughout the chapter.) The conserved quantities are the total particle density n, the total particle current $\boldsymbol{j}$, the magnetization density $Pn\Omega^\alpha$ and the energy. In the hydrodynamic approach we write for each conserved quantity

a continuity equation. Not considering energy conservation for simplicity, we therefore have the following set of hydrodynamic equations:

$$\partial_t n + \boldsymbol{\nabla} \cdot \boldsymbol{j} = 0, \tag{2.1}$$

$$\partial_t \left(P n \Omega^\alpha \right) + \boldsymbol{\nabla} \cdot \left((\boldsymbol{j}^{\perp}_{\text{spin}})^\alpha + (\boldsymbol{j}^{\parallel}_{\text{spin}})^\alpha \right) = 0, \tag{2.2}$$

$$m \partial_t \boldsymbol{j} + m \boldsymbol{\nabla} \cdot \boldsymbol{\Pi} + n \boldsymbol{\nabla} V - P n \boldsymbol{E} - P \boldsymbol{j} \times \boldsymbol{B} = 0. \tag{2.3}$$

In these equations, m is the particle mass, $\boldsymbol{\Pi} = n_n \boldsymbol{v}_n \boldsymbol{v}_n + n_s \boldsymbol{v}_s \boldsymbol{v}_s + \mathbf{1}\, p/m$ is the energy-momentum tensor, and V is the trapping potential. We have also introduced the pressure p, the normal fluid velocity $\boldsymbol{v}_n$ and the normal fluid density n_n, and equivalent quantities $\boldsymbol{v}_s$ and n_s for the superfluid. We use these quantities to define the normal and superfluid particle currents $\boldsymbol{j}_n = n_n \boldsymbol{v}_n$ and $\boldsymbol{j}_s = n_s \boldsymbol{v}_s$, such that $\boldsymbol{j} = \boldsymbol{j}_n + \boldsymbol{j}_s$. The total density is then $n = n_s + n_n$. Note that coordinate space tensors and vectors are denoted by bold font, while spin space vector components are denoted by Greek superscripts.

The coupling between magnetization and normal fluid leads to geometric forces [50, 51]. These can e.g. be understood as resulting from the Berry curvature and spin Berry phases that the atoms pick up as their spin adiabatically follows the magnetization texture. More concretely, there exist now an artificial electric field

$$\boldsymbol{E} = \hbar \varepsilon^{\alpha\beta\gamma} \Omega^\alpha (\partial_t \Omega^\beta)(\boldsymbol{\nabla} \Omega^\gamma)/2 \tag{2.4}$$

and an artificial magnetic field

$$\boldsymbol{B} = -\hbar \varepsilon^{\alpha\beta\gamma} \Omega^\alpha (\boldsymbol{\nabla} \Omega^\beta) \times (\boldsymbol{\nabla} \Omega^\gamma)/4, \tag{2.5}$$

where we have introduced the totally antisymmetric Levi-Civita tensor $\varepsilon^{\alpha\beta\gamma}$. As we have already seen in Eq. (2.3), these fields enter the hydrodynamic equations as the electric and magnetic parts of the Lorentz force, respectively, acting on the particle current.

A more detailed discussion on the spin currents is now in order. The longitudinal spin current describes spin transport with spin polarization along the magnetization direction due to particle currents: $(\boldsymbol{j}^{\parallel}_{\text{spin}})^\alpha = P \boldsymbol{j} \Omega^\alpha$. The transverse spin current has, to lowest order in the gradient expansion, terms proportional to the spin stiffness A_s and a parameter proportional to the transverse spin diffusion constant $\eta_\perp$ [52]:

$$(\boldsymbol{j}^{\perp}_{\text{spin}})^\alpha = -\varepsilon^{\alpha\beta\gamma} \frac{1}{n} \eta_\perp \Omega^\beta (n \partial_t + \boldsymbol{j} \cdot \boldsymbol{\nabla}) \boldsymbol{\nabla} \Omega^\gamma - A_s \varepsilon^{\alpha\beta\gamma} \Omega^\beta \boldsymbol{\nabla} \Omega^\gamma. \tag{2.6}$$

The first term describes transverse spin relaxation. It contains the usual hydrodynamic derivative and illustrates the fact that only gradients of magnetization relax because spin is conserved in our system. The second term represents non-dissipative transverse spin transport. Note that the above results

can be understood as containing all symmetry-allowed terms up to second order in gradients. The superfluid velocity obeys the Josephson relation

$$m\partial_t \boldsymbol{v}_s + \boldsymbol{\nabla}\left[mv_s^2/2 + V + \mu\right] - \boldsymbol{E} = 0, \tag{2.7}$$

where μ is the chemical potential, and also the Mermin-Ho relation

$$m\boldsymbol{\nabla} \times \boldsymbol{v}_s = -\boldsymbol{B}. \tag{2.8}$$

This completes the set of hydrodynamic equations.

Our hydrodynamic equations correctly describe the system at any temperature relevant for cold-atom experiments. At sufficiently low temperatures both order parameters are non-zero, and we have a ferromagnetic Bose-Einstein condensate with a negligible normal fluid density. Setting the normal fluid density and its velocity to zero, and setting the polarization to $P = 1$, we obtain the well-known $T = 0$ limit [48]. At higher temperatures, where the normal fluid density is sizable, we have to use the full set of equations. Heating the system even further results in the disappearance of the Bose-Einstein condensate at T_{BEC}. (Note that in general the critical temperature for Bose-Einstein condensation is lower than the ferromagnetic transition temperature, as shown in Ref. [12].) We then have to discard Eqs. (2.7) and (2.8), and set the superfluid density as well as its velocity to zero. Finally, in the high temperature limit $T > T_{\mathrm{FM}}$, the average magnetization is zero, and the distinction between longitudinal and transverse spin polarization disappears. In addition, there are no artificial electromagnetic fields and consequently the geometric forces vanish. For those reasons, the spin current becomes $j^{\alpha}_{\mathrm{spin}} = -D_s\boldsymbol{\nabla}(n\Omega^{\alpha})$, where D_s is the spin diffusion constant, which is related to the longitudinal spin relaxation time determined previously[53].

2.3 COLLECTIVE MODES

As a first application of the above, we consider the collective modes. Following the usual procedure, we linearize the equations and put in a plane-wave ansatz for the hydrodynamical variables. Solving for frequency ω as a function of momentum k results in

$$\omega = k\sqrt{\frac{1}{m}\frac{\partial p}{\partial n}} \equiv ck, \tag{2.9}$$

$$\omega = \frac{A_s(Pnk^2 - i\eta_\perp k^4)}{\eta_\perp^2 k^4 + (Pn)^2} \xrightarrow{k\to 0} \frac{A_s}{Pn}k^2 - \frac{i\eta_\perp A_s}{(Pn)^2}k^4. \tag{2.10}$$

The first equation describes a density wave, first sound, which propagates at the speed of sound c as expected. The second equation gives the dispersion for the spin waves and includes their damping. We remark that in the long-wavelength limit it reduces to a quadratic dispersion with quartic damping,

which is in agreement with previous results for conventional (Fermi) ferromagnets [54]. Finally, we did not consider energy as a hydrodynamic variable and hence neglected the resulting heat diffusion. Thus, our theory does not properly predict the velocity of second sound.

2.4 SKYRMION DYNAMICS AND TOPOLOGICAL HALL EFFECT

To illustrate the importance of geometrical forces, we investigate the motion of a 2D or baby skyrmion (Fig. 4). There are several reasons warranting a closer look at this 2D skyrmion. Firstly, we expect to see a topological Hall effect, due to the artificial electromagnetic fields generated by the spin texture. Moreover, due to the interplay between magnetization relaxation and spin gradients, we anticipate irreversible dynamics. Lastly, baby skyrmions have been experimentally realized in spinor Bose gases [55], suggesting that our theory could be confronted with experiments in the near future.

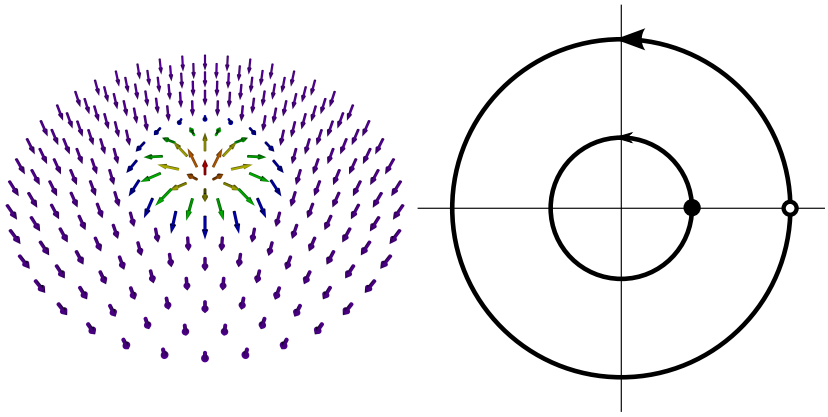

FIGURE 4: A baby skyrmion in a two-dimensional ferromagnetic cloud (*left*). In an isotropic trap, which has its center in the middle of the picture (*right*), the skyrmion (empty circle) precesses around the center of the trap. The center of the cloud (filled circle) also moves around the center of the trap due to the topological Hall effect. The amplitude of the motion of the center of the cloud has been enhanced for clarity.

Considering a rigid skyrmion texture $\Omega^\alpha = \Omega^\alpha(\boldsymbol{x} - \boldsymbol{x}_{\mathrm{sk}})$ with a velocity $\boldsymbol{v}_{\mathrm{sk}} = (\dot{x}_{\mathrm{sk}}, \dot{y}_{\mathrm{sk}})$, we derive its equations of motion from our hydrodynamic description of the dynamics of the atomic cloud. To that end, we take a cross product of Ω^α with Eq. (2.2), then take an inner product with $\boldsymbol{\nabla}\Omega^\alpha$ and finally perform an integral over the coordinate space. Moreover, we assume a pancake-like geometry at a low temperature, and a Thomas-Fermi density profile for this calculation. We define the trap to be isotropic and harmonic in the xy-plane with the frequency ω_d. Furthermore, $\eta_\perp$ is taken to be constant, $A_s(\boldsymbol{x}) = n(\boldsymbol{x})a_s$, and $a_s = \hbar P/2m$ as is shown below. We also introduce the

density in the center of the cloud n_0, the density in the center of the skyrmion n_{sk} and the radius of the cloud R. The equations of motion ultimately read

$$\begin{aligned}
\ddot{x} + \omega_d^2 x - \Delta\dot{y} P\hbar I_{12}^1 n_{\mathrm{sk}}/\pi m n_0 R^2 &= 0,\\
\ddot{y} + \omega_d^2 y + \Delta\dot{x} P\hbar I_{12}^1 n_{\mathrm{sk}}/\pi m n_0 R^2 &= 0,\\
\Delta\dot{x}(\eta_\perp I_{12}^2 + n_{\mathrm{sk}} P I_{12}^1) + \Delta\dot{y}\eta_\perp I_{22}^2 + \Delta y n_0 a_s I^3/R^2 &= 0,\\
\Delta\dot{y}(\eta_\perp I_{12}^2 - n_{\mathrm{sk}} P I_{12}^1) + \Delta\dot{x}\eta_\perp I_{11}^2 + \Delta x n_0 a_s I^3/R^2 &= 0,
\end{aligned}$$

where $\Delta x = x_{\mathrm{sk}} - x$ and $\Delta y = y_{\mathrm{sk}} - y$ are the skyrmion coordinates relative to the center of the cloud. The quantities I_{ij}^1, I_{ij}^2 and I^3 are real and only depend on the texture[2], where i, j can be 1 or 2, corresponding to the x or y direction, respectively. The integral I_{12}^1 is determined by a topological invariant known as the skyrmion number or the winding number: $W = I_{12}^1/4\pi = 1$. Furthermore, for cylindrically symmetric skyrmion textures, $I^3 = h$ and $I_{ij}^2 = -\tilde{h}\delta_{ij}/l^2$, where h and $\tilde{h}$ are dimensionless numbers, while l is the length associated with the size of the skyrmion[3]. The latter integrals are therefore not determined by the topology of the magnetization texture only.

Following the procedure described above, we find, in addition to the dipole mode with frequency ω_d, a collective mode pertaining to the motion of the skyrmion with the frequency

$$\omega_{\mathrm{sk}} = \frac{h n_0 \hbar \left(4 n_{\mathrm{sk}} P\pi + i\tilde{h}\eta_\perp/l^2\right)}{2mR^2\left(16 n_{\mathrm{sk}}^2 P^2\pi^2 + \tilde{h}^2\eta_\perp^2/l^4\right)}. \tag{2.11}$$

The real part of the frequency implies that the skyrmion is moving around the center of the trap, c.f. Fig. 4, while the positive imaginary part means that the skyrmion is spiraling out and is pushed away from the center of the trap.

We now turn our attention to the case of no damping ($\eta_\perp = 0$). The eigenvectors of the various modes, written in the form $(x, y, \Delta x, \Delta y)$, are $(1,0,0,0)$, $(0,1,0,0)$, $(-i\alpha, \alpha, -i, 1)$ and $(i\alpha, \alpha, i, 1)$ with

$$\alpha = \frac{32 h n_{\mathrm{sk}}^2 P^2 \pi\hbar^2}{64 m^2 n_{\mathrm{sk}}^2 P^2\pi^2 R^4 \omega_d^2 - h^2 n_0^2 \hbar^2}. \tag{2.12}$$

The first two eigenvectors describe the dipole mode, where the cloud and the skyrmion move in phase in either the x or the y direction, respectively. In order to investigate the implications of the third and fourth eigenvectors, we set the initial coordinates $\Delta x(0) \neq 0$ and $x(0) = \alpha\Delta x(0)$ with $y(0) =$

2 $I_{ij}^1 = \int_{\boldsymbol{x}} (\nabla_i \Omega^\alpha)(\nabla_j \Omega^\beta)\Omega^\gamma \varepsilon^{\alpha\beta\gamma}$, $I_{ij}^2 = \int_{\boldsymbol{x}} [(\nabla_i\Omega^\beta)(\nabla_k\Omega^\beta)(\nabla_j\Omega^\gamma)(\nabla_k\Omega^\gamma) - (\nabla_i\nabla_k\Omega^\gamma)(\nabla_j\nabla_k\Omega^\gamma)]$, $I^3 = \int_{\boldsymbol{x}} (\nabla_k\Omega^\gamma)(\nabla_k\Omega^\gamma)$.

3 For a magnetization texture $\Omega^\alpha = (\sin A(r) cos\phi, \sin A(r)\sin\phi, \cos A(r))$, where $A(r) = 2\arctan(r/l)$, on a plane parameterized by polar coordinates (r, ϕ), we find $h = 8\pi$, $\tilde{h} = 16\pi/3$.

$\Delta y(0) = 0$. We set the initial velocity of the cloud to zero. In that case, x and Δx oscillate in phase with the frequency $\omega_{\mathrm{sk}} = hn_0\hbar/8mn_{\mathrm{sk}}P\pi R^2$:

$$x = \alpha\Delta x(0)\cos(\omega_{\mathrm{sk}}t), \quad \Delta x = \Delta x(0)\cos(\omega_{\mathrm{sk}}t). \tag{2.13}$$

However, both the center of the cloud and the skyrmion start moving in the y direction is as well (cf. Fig. 4):

$$y = \alpha\Delta x(0)\left[\sin(\omega_{\mathrm{sk}}t) - \frac{\omega_{\mathrm{sk}}}{\omega_d}\sin(\omega_d t)\right], \tag{2.14}$$

$$\Delta y = \Delta x(0)\sin(\omega_{\mathrm{sk}}t), \tag{2.15}$$

due to the force exerted on them by the artificial electromagnetic field, which can also be seen in the equations of motion. Physically, this effect is a Hall effect as it corresponds to transverse motion in response to a longitudinal force – in this case the restoring force of the trapping potential. Due to the nature of this particular spin texture, this effect is known as the topological Hall effect.

2.5 MICROSCOPIC THEORY

We proceed to evaluate the hydrodynamic input parameters P, A_s and $\eta_\perp$. To calculate the polarization P, we employ the Bogoliubov theory around the ferromagnetic groundstate of the gas. That amounts to populating only one of the condensate components, $n_c^\uparrow = n_c \neq 0$, while $n_c^\downarrow = 0$. Scattering amplitudes in ultracold gases are governed by the two-body T matrix g [8], which can have different components for collisions of different spin states. We only consider the case with equal T-matrix elements $g^{\uparrow\downarrow} = g^{\uparrow\uparrow} = g^{\downarrow\downarrow} = g \neq 0$. Furthermore, we investigate a balanced mixture, i.e., with equal chemical potentials $\mu^\uparrow = \mu^\downarrow = gn_c^\uparrow$. This leads to decoupling of the spin components. The $\uparrow$ particles obtain the usual Bogoliubov propagator, while the $\downarrow$ particles retain the non-interacting propagator within this approximation. We thus find the following particle densities in the non-condensate states:

$$n_{\mathrm{nc}}^\uparrow = \frac{1}{V}\sum_{k\neq 0}\left(\frac{\varepsilon_k + gn_c}{\hbar\omega_k}\,\frac{1}{e^{\beta\hbar\omega_k}-1} + \frac{\varepsilon_k + gn_c - \hbar\omega_k}{2\hbar\omega_k}\right), \tag{2.16}$$

and $n_{nc}^\downarrow = \sum_{k\neq 0}[\exp(\beta\varepsilon_k) - 1]^{-1}/V$, where the Bogoliubov dispersion $\hbar\omega_k = \sqrt{\varepsilon_k(\varepsilon_k + 2gn_c)}$, $\beta = 1/k_{\mathrm{B}}T$ is the inverse thermal energy and $\varepsilon_k = \hbar^2k^2/2m$ is the free particle dispersion. The density distributions are subject to the constraint $n = n_c + n_{nc}^\uparrow + n_{nc}^\downarrow$. We note that after fixing the total density n, temperature and interaction strength, we can solve these equations for n_c and obtain $n_{nc}^\uparrow$ as well as $n_{nc}^\downarrow$ at the same time. This gives us the polarization of the gas

$$P = (n_c + n_{nc}^\uparrow - n_{nc}^\downarrow)/n = 1 - 2n_{nc}^\downarrow/n. \tag{2.17}$$

In the intermediate temperature regime $ng \ll k_B T < k_B T_{\mathrm{BEC}}$ it is straightforward to calculate P analytically. To that end, we approximate $\hbar\omega_k \simeq \varepsilon_k + g n_c$, so that $n_{nc}^{\uparrow} = n_{nc}^{\downarrow} = \zeta(3/2)(m k_B T/2\pi\hbar^2)^{3/2}$ and

$$P = 1 - 2\zeta(3/2)(m k_B T/2\pi\hbar^2)^{3/2}/n, \tag{2.18}$$

where ζ denotes the Riemann zeta function. Note that in this approximation we have $P = 1$ at zero temperature, as the depletion of the condensate is neglected and all the ideal gas particles end up in the condensate.

We now turn to the calculation of the spin stiffness A_s. According to the Bogoliubov theory, when only one spin component is populated with a Bose-Einstein condensate, excitations in the other spin components are free particles, corresponding to spin waves. Therefore, the dispersion of the spin waves is simply $\hbar\omega_k = \varepsilon_k$. Comparing this with the real part of the dispersion relation for the spin waves given by the hydrodynamics in Eq. (2.10), we conclude that

$$A_s = \frac{\hbar}{2m} P n. \tag{2.19}$$

The only quantity that remains to be evaluated is $\eta_\perp$. An upper bound for this quantity is found by considering the non-condensed phase. In this case, we note that it is equal to the transverse spin conductivity [52]

$$\eta_\perp = \hbar\sigma_\perp. \tag{2.20}$$

We calculate $\sigma_\perp$ in the normal phase from a set of Boltzmann equations and use the relaxation-time approximation. For a given species, e.g. $\uparrow$, the momentum-dependent relaxation time $(\tau^{\uparrow\uparrow})_k$ is given by the well-known collision integral

$$\begin{aligned}\frac{1}{(\tau^{\uparrow\uparrow})_k} =& \frac{2\pi}{\hbar} g_{\uparrow\downarrow}^2 \int \frac{\mathrm{d}\mathbf{k}_2}{(2\pi)^3}\frac{\mathrm{d}\mathbf{k}_3}{(2\pi)^3}\frac{\mathrm{d}\mathbf{k}_4}{(2\pi)^3} f^{\downarrow\downarrow}(\mathbf{k}_2)[1 + f^{\uparrow\uparrow}(\mathbf{k}_3)] \\ &\times [1 + f^{\downarrow\downarrow}(\mathbf{k}_4)](2\pi)^3\delta^{(3)}(\mathbf{k} + \mathbf{k}_2 - \mathbf{k}_3 - \mathbf{k}_4) \\ &\times \delta(\varepsilon_k + \varepsilon_{k_2} - \varepsilon_{k_3} - \varepsilon_{k_4}),\end{aligned} \tag{2.21}$$

that can be derived using Fermi's golden rule. Here we only consider the term due to inter-species scattering, as intra-species scattering terms drive the distributions $f^{\uparrow\uparrow}$ and $f^{\downarrow\downarrow}$ towards the Bose-Einstein equilibrium distribution.

The transverse spin relaxation time is then given by

$$2/(\tau_s^{\perp})_k = 1/(\tau^{\uparrow\uparrow})_k + 1/(\tau^{\downarrow\downarrow})_k. \tag{2.22}$$

Given this relaxation time, the transverse spin conductivity is obtained by evaluating the integral

$$\eta_\perp = -\frac{\hbar^3}{m^2}\int \mathrm{d}\mathbf{k} k^2 \frac{(\tau_s^{\perp})_k}{1 + [(\tau_s^{\perp})_k \Delta/\hbar]^2}\frac{\partial f_0}{\partial \varepsilon_k}, \tag{2.23}$$

where f_0 is the sum of the equilibrium distributions of $\uparrow$ and $\downarrow$ particles and $\Delta = \mu^{\uparrow} - \mu^{\downarrow}$ is the exchange splitting. For a particular kind of atom, $\eta_\perp$ depends on the temperature and all the scattering lengths in the system. However, by fixing the inter-species T matrix $g_{\uparrow\downarrow}$, we can obtain a more general picture as a function of temperature and polarization as shown in Fig. 5.

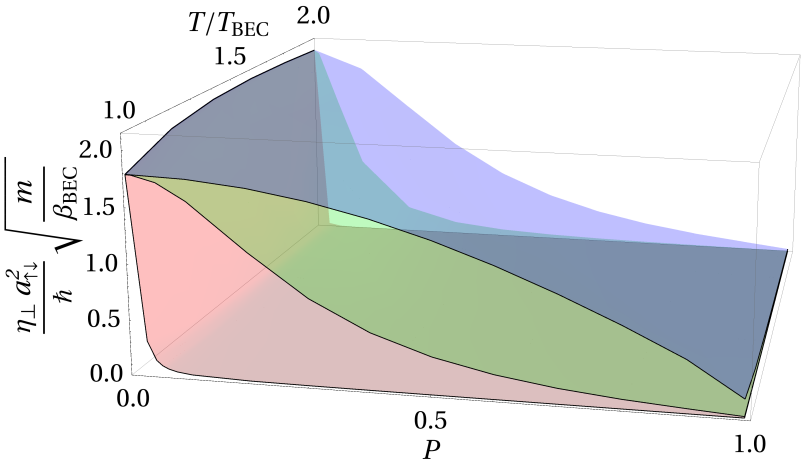

FIGURE 5: Transverse spin diffusion $\eta_\perp$ as a function of polarization P and temperature for a homogeneous gas. The three surfaces correspond to $ng_{\uparrow\downarrow}\beta_{\mathrm{BEC}} = 1$, 0.5 and 0.1 from top to bottom. Here $a_{\uparrow\downarrow}$ is the inter-species scattering length and $\beta_{\mathrm{BEC}} \equiv 1/k_B T_{\mathrm{BEC}}$.

2.6 DISCUSSION AND CONCLUSION

In summary, we have constructed a hydrodynamic theory for a ferromagnetic spin-1/2 Bose gas that is valid for any temperature relevant for cold-atom systems. We have also calculated all the input parameters for the hydrodynamic theory within the Bogoliubov approximation. Finally, we have considered dynamics of a topological spin texture (skyrmion) and found it to lead to a topological Hall effect.

To determine if the topological Hall effect can be observed experimentally, we estimate the skyrmion precession frequency ω_{sk} and the eigenvector parameter α. Considering a condensate of 10^4 ^{23}Na atoms in a pancake-like geometry with radial confinement $\omega_\perp/2\pi = 1\,\mathrm{Hz}$ and perpendicular confinement $\omega_z = 10\omega_\perp$, we estimate $\omega_{\mathrm{sk}} = \omega_\perp$ and $\alpha = 0.1$. This corresponds to a cloud size of $50\,\mu m$ and a Hall amplitude of $5\,\mu m$, which should be observable with current experimental techniques.

When it comes to the damping of spin waves, we consider a homogeneous ^{87}Rb gas ($|F = 1, m_f = -1\rangle$ and $|F = 2, m_f = 1\rangle$) with the density of 10^{16}

cm^{-3} as an example. In particular, at the Bose-Einstein condensation temperature and polarization $P = 1/2$ a spin wave with momentum $k = 1\,\mu m^{-1}$, which is within the reach of current experiments, has a damping time of 0.7 s.

In the future work, we plan to calculate $\eta_\perp$ in the superfluid phase ($T < T_{\mathrm{BEC}}$), which would complete the microscopic input for the parameters of the hydrodynamic theory in the entire temperature range. Moreover, it is worthwhile to apply the current approach to higher spin systems, where extra degrees of freedom such as the nematic tensor [56] enter the theory.

3

HYDRODYNAMIC MODES OF PARTIALLY-CONDENSED BOSE MIXTURES

We generalize the Landau-Khalatnikov hydrodynamic theory for superfluid helium to two-component (binary) Bose mixtures at arbitrary temperatures[1]. In particular, we include the spin-drag terms that correspond to viscous coupling between the clouds. Therefore, our theory not only describes the usual collective modes of the individual components, e.g., first and second sound, but also results in new collective modes, where both constituents participate. We study these modes in detail and present their dispersions using thermodynamic quantities obtained within the Popov approximation.

3.1 INTRODUCTION

The realization of a Bose-Einstein condensate (BEC) in ultracold alkali vapors [57, 43, 58] has ignited a rapid progress in the understanding of degenerate gases at low temperatures [59, 60]. A large part of this understanding has been gained through the study of collective modes [61, 62, 63]. In particular, it has been shown that for a weakly-interacting gas of bosons close to absolute zero temperature, the collective excitations are Bogoliubov quasiparticles [64, 65, 66, 67] that are responsible for fascinating properties of the system, including superfluidity and quantum depletion of the condensate.

Work building upon the single-component ultracold gases has provided access to even richer systems. In particular, considering mixtures of several species of particles with the same (Bose-Bose or Fermi-Fermi mixtures [68, 69]) or different statistics (Bose-Fermi mixtures [70]) has become possible. These systems are known as binary mixtures or two-component gases. Arguably the simplest of them is a mixture of two different hyperfine states of the same bosonic atom. However, even this simple system poses important questions concerning the nature of its ground state and the excitations. Therefore, much work has been carried out on the static and dynamic properties of the two-component Bose gas [71, 72, 73, 74, 75, 76, 77, 78, 79, 80, 81, 82, 83, 84], both in the uniform case, and also for the trapped case. Most of the effort has been concentrated on the zero-temperature physics, with only a few studies [85, 86] on the properties of binary Bose mixtures at non-zero temperature.

Having more than a single component in the gas also allows one to make a connection to the physics of spins, by introducing a pseudospin to distinguish the two components. In particular, one can consider ferromagnetic and

1 This chapter is directly based on J. Armaitis, H. T. C. Stoof, and R. A. Duine, *Hydrodynamic Modes of Partially-Condensed Bose Mixtures*, arXiv:1502.03138.

antiferromagnetic states [44, 45, 49] as well as spin dynamics [87, 88], and topological spin textures [89, 90, 91, 44, 45, 92, 93, 94, 24, 95]. One kinetic effect concerning the spin dynamics is the so-called spin drag [96, 53]. This recently observed [97, 98] effect corresponds to the relaxation of the difference of the velocities between the two components. Understanding the interplay between the BEC, the thermal particles, and the spin degrees of freedom in this relatively simple and well-controlled two-component Bose gas might also offer some insights for interacting spinful degenerate systems of a rather different nature, such as the condensate of magnons [99, 100].

In this paper we build upon our previous results for the ferromagnetic Bose gas [94], but now consider a different situation where two condensates are present in the miscible regime. We tackle the problem of the collective modes of the two-component mixture both in the uniform gas and in a trap, in an effort of making a connection with experiments. The structure of the paper is as follows. In Sec. II we describe the Popov theory of the binary Bose mixture, and present relevant thermodynamic functions in that approximation, including the equation of state. We study the effects of spin drag in Sec. III. In Sec. IV we develop a linear hydrodynamic model that makes use of our previous thermodynamic results and describes a two-component system accounting for spin drag. We present the results for the uniform and trapped gas in Sec. V. Finally, we conclude in Sec. VI.

3.2 MICROSCOPIC THEORY

In this section we briefly describe the microscopic Popov theory of the two-component Bose mixture. The Popov theory is an extension of the Bogoliubov theory to relatively high temperatures, which includes an improved treatment of the excitations. Specifically, the Bogoliubov excitations are allowed to interact, and their interactions are treated in the Hartree-Fock approximation. Multi-component gases of bosons have been treated in the Bogoliubov framework before [101]. In particular, two-component mixtures have been considered in Refs. [102, 76, 79], and some results from the Popov theory have been presented in Ref. [86]. The novelty of our results is twofold: we present the Popov analysis in the functional-integral formalism, and calculate the thermodynamic properties of the balanced binary Bose gas. Our discussion on the Bogoliubov transformation follows the usual grand-canonical treatment of the problem. The single-component situation has been treated in this way in, for instance, Refs. [103, 8].

3.2.1 *General binary mixture*

In general, a grand-canonical partition function for two bosonic fields ($\phi_\uparrow$ and $\phi_\downarrow$) that includes all the possible s-wave interactions is

$$Z = \int d[\phi_\uparrow^*] d[\phi_\uparrow] d[\phi_\downarrow^*] d[\phi_\downarrow] e^{-S[\phi_\uparrow^*, \phi_\uparrow, \phi_\downarrow^*, \phi_\downarrow]/\hbar}, \tag{3.1}$$

where the action is

$$\begin{aligned} S[\phi_\uparrow^*, \phi_\uparrow, \phi_\downarrow^*, \phi_\downarrow] &= \int_0^{\hbar\beta} d\tau \int d\boldsymbol{x} \\ &\times \left(\sum_{\sigma=\uparrow,\downarrow} \left[\phi_\sigma^* \left(\hbar\partial_\tau - \frac{\hbar^2 \boldsymbol{\nabla}^2}{2m_\sigma} - \mu_\sigma \right) \phi_\sigma \right. \right. \\ &\left. \left. + \frac{1}{2} g_{\sigma\sigma} \phi_\sigma^* \phi_\sigma^* \phi_\sigma \phi_\sigma \right] + g_{\uparrow\downarrow} \phi_\uparrow^* \phi_\downarrow^* \phi_\downarrow \phi_\uparrow \right), \end{aligned} \tag{3.2}$$

and all the fields are considered at the position $\boldsymbol{x}$ and the imaginary time τ. Moreover, $\beta = 1/k_B T$ is the inverse thermal energy, m_σ are the masses of the particles, and $g_{\sigma\sigma'}$ are the two-body T matrices describing the s-wave interactions.

From now on we focus on the symmetric case, where the masses are equal $m = m_\uparrow = m_\downarrow$, and the intra-species interactions are the same and described by a single scattering length a. Thus

$$g = g_{\uparrow\uparrow} = g_{\downarrow\downarrow} = \frac{4\pi\hbar^2 a}{m}. \tag{3.3}$$

The inter-species interactions are described by another scattering length $a_{\uparrow\downarrow}$ implying that

$$g_{\uparrow\downarrow} = \frac{4\pi\hbar^2 a_{\uparrow\downarrow}}{m}. \tag{3.4}$$

All the interactions are assumed to be repulsive, i.e., $g > 0$, and $g_{\uparrow\downarrow} > 0$. Furthermore, as opposed to our earlier work in Ref. [94], we here focus on the case with two separate condensates. In order for this to be possible, the condition

$$g > g_{\uparrow\downarrow} \tag{3.5}$$

has to be satisfied, as otherwise the two components demix [4].

We are now in a position to perform a fluctuation expansion for each species by putting

$$\phi_\sigma(\boldsymbol{x}, \tau) = \phi_{0\sigma}(\boldsymbol{x}) + \phi'_\sigma(\boldsymbol{x}, \tau), \tag{3.6}$$

where the fluctuations $\phi'_\sigma(\boldsymbol{x},\tau)$ are on average zero. Moreover, the fluctuations are orthogonal to the condensate $\langle\phi_\sigma(\boldsymbol{x},\tau)\rangle = \phi_{0\sigma}(\boldsymbol{x})$ of the same species which means that

$$\int d\boldsymbol{x}\left(\phi^*_{0\sigma}(\boldsymbol{x})\phi'_\sigma(\boldsymbol{x},\tau) + \phi_{0\sigma}(\boldsymbol{x})\phi'^*_\sigma(\boldsymbol{x},\tau)\right) = 0. \tag{3.7}$$

Since in what follows the relative phases of the condensates do not play a significant role, we choose both the condensate fields to be real:

$$\phi_{0\sigma}(\boldsymbol{x}) = \sqrt{n_{0\sigma}}, \tag{3.8}$$

where $n_{0\sigma}$ is the atomic (number) density of the condensed σ particles. Moreover, since we are considering the uniform case here, the condensate density has no spatial dependence. Expanding the fields in the action in this manner, we have for the action

$$S = S_0 + \sum_{\sigma=\uparrow,\downarrow} S_{1\sigma} + S_2 + S_3 + S_4, \tag{3.9}$$

where the zeroth-order (or Landau-free-energy) contribution is

$$\begin{aligned} S_0 = \hbar\beta V\big(&- \mu_\uparrow n_{0\uparrow} + g n_{0\uparrow}^2/2 \\ &- \mu_\downarrow n_{0\downarrow} + g n_{0\downarrow}^2/2 + g_{\uparrow\downarrow} n_{0\uparrow} n_{0\downarrow}\big), \end{aligned} \tag{3.10}$$

the term linear in fluctuations reads

$$\begin{aligned} S_{1\sigma}[\phi'^*_\sigma,\phi'_\sigma] = \int_0^{\hbar\beta} d\tau \int d\boldsymbol{x} \Big[\phi'^*_\sigma\big(&- \mu_\sigma + g n_{0\sigma} \\ &+ g_{\uparrow\downarrow} n_{0\bar{\sigma}}\big)\sqrt{n_{0\sigma}} + \text{c.c.}\Big], \end{aligned} \tag{3.11}$$

and the quadratic term is

$$\begin{aligned} &S_2[\phi'^*_\uparrow,\phi'_\uparrow,\phi'^*_\downarrow,\phi'_\downarrow] \\ &= \int_0^{\hbar\beta} d\tau \int d\boldsymbol{x} \sum_{\sigma=\uparrow,\downarrow} \left[\phi'^*_\sigma\left(\hbar\partial_\tau - \frac{\hbar^2\boldsymbol{\nabla}^2}{2m} - \mu_\sigma + 2g n_{0\sigma} + g_{\uparrow\downarrow} n_{0\bar{\sigma}}\right)\phi'_\sigma \right. \\ &\qquad \left. + \frac{g n_{0\sigma}}{2}\left(\phi'^*_\sigma \phi'^*_\sigma + \phi'_\sigma \phi'_\sigma\right)\right] \\ &\quad + g_{\uparrow\downarrow}\sqrt{n_{0\uparrow} n_{0\downarrow}} \int_0^{\hbar\beta} d\tau \int d\boldsymbol{x}\left(\phi'_\uparrow\phi'_\downarrow + \phi'^*_\uparrow\phi'_\downarrow + \phi'_\uparrow\phi'^*_\downarrow + \phi'^*_\uparrow\phi'^*_\downarrow\right), \end{aligned} \tag{3.12}$$

where all the fluctuation fields are evaluated at $(\boldsymbol{x}, \tau)$, and we have denoted the species opposite to σ by $\bar{\sigma}$. Furthermore, S_3 and S_4 terms describe the interactions between the fluctuations:

$$\begin{aligned} &S_3[\phi'^*_\uparrow, \phi'_\uparrow, \phi'^*_\downarrow, \phi'_\downarrow] \\ &= \int_0^{\hbar\beta} d\tau \int d\boldsymbol{x} \Bigg(\sum_{\sigma=\uparrow,\downarrow} g\sqrt{n_{0\sigma}} \left(\phi'^*_\sigma \phi'^*_\sigma \phi'_\sigma + \phi'_\sigma \phi'_\sigma \phi'^*_\sigma\right) \\ &+ g_{\uparrow\downarrow}\sqrt{n_{0\uparrow}}(\phi'^*_\downarrow \phi'_\downarrow \phi'_\uparrow + \phi'_\downarrow \phi'^*_\downarrow \phi'^*_\uparrow) + g_{\uparrow\downarrow}\sqrt{n_{0\downarrow}}(\phi'^*_\uparrow \phi'_\downarrow \phi'_\uparrow + \phi'_\uparrow \phi'^*_\downarrow \phi'^*_\uparrow)\Bigg), \end{aligned} \tag{3.13}$$

and

$$\begin{aligned} &S_4[\phi'^*_\uparrow, \phi'_\uparrow, \phi'^*_\downarrow, \phi'_\downarrow] = \\ &\int_0^{\hbar\beta} d\tau \int d\boldsymbol{x} \Bigg(\sum_{\sigma=\uparrow,\downarrow} \frac{g}{2} \phi'^*_\sigma \phi'^*_\sigma \phi'_\sigma \phi'_\sigma + g_{\uparrow\downarrow} \phi'^*_\uparrow \phi'^*_\downarrow \phi'_\downarrow \phi'_\uparrow \Bigg). \end{aligned} \tag{3.14}$$

Note that the terms S_3 and S_4 are neglected in the Bogoliubov theory.

We now perform the Hartree-Fock theory for the excitations, which involves the inclusion of the mean field

$$\langle \phi'^*_\sigma \phi'_\sigma \rangle = n'_\sigma, \tag{3.15}$$

where n'_σ is the density of the excitations of the σ species such that the total density of a species is

$$n_\sigma = n_{0\sigma} + n'_\sigma. \tag{3.16}$$

Note that we neglect the coherence between the two species and take $\langle \phi'^*_\sigma \phi'_{\bar{\sigma}} \rangle = 0$. Therefore, the appropriate mean-field substitutions are

$$\phi'^*_\sigma \phi'^*_\sigma \phi'_\sigma \phi'_\sigma \to 4n'_\sigma \phi'^*_\sigma \phi'_\sigma - 2{n'_\sigma}^2, \tag{3.17}$$

$$\phi'^*_\uparrow \phi'^*_\downarrow \phi'_\downarrow \phi'_\uparrow \to n'_\uparrow \phi'^*_\downarrow \phi'_\downarrow + n'_\downarrow \phi'^*_\uparrow \phi'_\uparrow - n'_\downarrow n'_\uparrow, \tag{3.18}$$

where the subtractions account for double counting in the quartic term of the action, whereas in the cubic terms no double-counting problems appear, as can be seen by applying Wick's theorem.

By requiring all the linear terms in ϕ'_σ and ϕ'^*_σ of the action to vanish, we obtain a set of two Gross-Pitaevskii equations for the uniform condensates that read

$$(-\mu_\uparrow + g n_{0\uparrow} + g_{\uparrow\downarrow} n_{0\downarrow} + 2g n'_\uparrow + g_{\uparrow\downarrow} n'_\downarrow)\sqrt{n_{0\uparrow}} = 0, \tag{3.19}$$

$$(-\mu_\downarrow + g n_{0\downarrow} + g_{\uparrow\downarrow} n_{0\uparrow} + 2g n'_\downarrow + g_{\uparrow\downarrow} n'_\uparrow)\sqrt{n_{0\downarrow}} = 0, \tag{3.20}$$

and from which the chemical potentials are obtained as

$$\mu_\uparrow = g n_{0\uparrow} + g_{\uparrow\downarrow} n_{0\downarrow} + 2g n'_\uparrow + g_{\uparrow\downarrow} n'_\downarrow, \tag{3.21}$$

$$\mu_\downarrow = g n_{0\downarrow} + g_{\uparrow\downarrow} n_{0\uparrow} + 2g n'_\downarrow + g_{\uparrow\downarrow} n'_\uparrow. \tag{3.22}$$

In order to diagonalize the quadratic part of the action, we perform a Fourier transformation, and then introduce Nambu space [8]. Since we want to rewrite the quadratic part of the action in the form

$$S_2[\phi'^*_\uparrow, \phi'_\uparrow, \phi'^*_\downarrow, \phi'_\downarrow] = -\frac{\hbar}{2} \sum_{\boldsymbol{k}\neq 0, n} \boldsymbol{\Phi}_{\boldsymbol{k}n} \cdot \boldsymbol{G}^{-1}_{\boldsymbol{k}n} \cdot \boldsymbol{\Phi}^\dagger_{\boldsymbol{k}n}, \tag{3.23}$$

where $\hbar\boldsymbol{k}$ is the momentum, n labels the Matsubara frequencies $\omega_n = 2\pi n/\hbar\beta$,

$$\boldsymbol{\Phi}_{\boldsymbol{k}n} = \left(\phi'^*_{\uparrow \boldsymbol{k}n}, \phi'_{\uparrow -\boldsymbol{k}n}, \phi'^*_{\downarrow \boldsymbol{k}n}, \phi'_{\downarrow -\boldsymbol{k}n}\right), \tag{3.24}$$

is a vector in the appropriate Nambu space in this case, and $\boldsymbol{G}^{-1}$ is the inverse Green's function of the system. Note that we have to take care to preserve the correct time ordering. The latter results in the following extra term in the action

$$\begin{aligned} S_{\mathrm{TO}} = &-\frac{\hbar\beta}{2} \sum_{\sigma, \boldsymbol{k}\neq 0, n} \left[\varepsilon_{\boldsymbol{k}} - \mu_\sigma + g(2n_{0\sigma} + 2n'_\sigma)\right. \\ &\left. + g_{\uparrow\downarrow}(n_{0\bar{\sigma}} + n'_{\bar{\sigma}})\right] = -\frac{\hbar\beta}{2} \sum_{\sigma, \boldsymbol{k}\neq 0, n} \left(\varepsilon_{\boldsymbol{k}} + g n_{0\sigma}\right), \end{aligned} \tag{3.25}$$

where $\varepsilon_{\boldsymbol{k}} = \hbar^2 k^2/2m$ is the kinetic energy. Therefore, plugging in the expressions for the chemical potentials μ_σ into the action we have

$$\begin{aligned} S = &-\hbar\beta V \left(g_{\uparrow\downarrow} n_\uparrow n_\downarrow + g(n^2_\downarrow + n^2_\uparrow) \right. \\ &\left. - g\frac{n^2_{0\downarrow} + n^2_{0\uparrow}}{2} \right) - \frac{\hbar\beta}{2} \sum_{\sigma, \boldsymbol{k}\neq 0} \left(\varepsilon_{\boldsymbol{k}} + g n_{0\sigma}\right) \\ &- \frac{\hbar}{2} \sum_{\boldsymbol{k}\neq 0, n} \boldsymbol{\Phi}_{\boldsymbol{k}n} \cdot \boldsymbol{G}^{-1}_{\boldsymbol{k}n} \cdot \boldsymbol{\Phi}^\dagger_{\boldsymbol{k}n}, \end{aligned} \tag{3.26}$$

where V is the volume of the system, while

$$-\hbar \boldsymbol{G}^{-1}_{\boldsymbol{k}n} = \begin{pmatrix} -\hbar G^{-1}_{\mathrm{B},\uparrow \boldsymbol{k}n} & \hbar\Sigma_{\uparrow\downarrow} \\ \hbar\Sigma_{\uparrow\downarrow} & -\hbar G^{-1}_{\mathrm{B},\downarrow \boldsymbol{k}n} \end{pmatrix}, \tag{3.27}$$

where $G^{-1}_{\mathrm{B},\uparrow \boldsymbol{k}n}$ and $\Sigma_{\uparrow\downarrow}$ are two-by-two submatrices (from now on two-by-two matrices are denoted by capital letters, while four-by-four matrices are denoted by bold capital letters). The submatrices on the diagonal are exactly the same as the Bogoliubov (single-component) inverse Green's functions, that is,

$$-\hbar G^{-1}_{\mathrm{B},\sigma \boldsymbol{k}n} = \begin{pmatrix} -i\hbar\omega_n + \varepsilon_{\boldsymbol{k}} + g n_{0\sigma} & g n_{0\sigma} \\ g n_{0\sigma} & i\hbar\omega_n + \varepsilon_{\boldsymbol{k}} + g n_{0\sigma} \end{pmatrix}, \tag{3.28}$$

and the off-diagonal matrix is the self-energy due to the interspecies coupling given by

$$\hbar\Sigma_{\uparrow\downarrow} = g_{\uparrow\downarrow}\sqrt{n_{0\uparrow}n_{0\downarrow}}\begin{pmatrix}1 & 1\\ 1 & 1\end{pmatrix}. \tag{3.29}$$

Anticipating the Bogoliubov transformation we define

$$\boldsymbol{I} = \begin{pmatrix}\sigma_z & 0\\ 0 & \sigma_z\end{pmatrix}, \tag{3.30}$$

where

$$\sigma_z = \begin{pmatrix}1 & 0\\ 0 & -1\end{pmatrix}. \tag{3.31}$$

Moreover, we define a matrix $\boldsymbol{\Gamma}_{\boldsymbol{k}}$ which is obtained by setting ω_n to zero in the inverse Green's function, i.e.,

$$\boldsymbol{\Gamma}_{\boldsymbol{k}} = -\hbar\boldsymbol{G}_{\boldsymbol{k}0}^{-1}. \tag{3.32}$$

We now proceed to diagonalize the matrix $\boldsymbol{\Gamma}_{\boldsymbol{k}}$ while keeping the bosonic character of the excitations, i.e., requiring that their operators obey bosonic commutation relations. In our formalism the preservation of the bosonic commutation relations is represented by the fact that the Matsubara-frequency terms are unaffected by the transformation. Hence, we look for real eigenvectors $\boldsymbol{w}$ of $\boldsymbol{I}\cdot\boldsymbol{\Gamma}_{\boldsymbol{k}}$:

$$\boldsymbol{I}\cdot\boldsymbol{\Gamma}_{\boldsymbol{k}}\cdot\boldsymbol{w}_{\pm,\boldsymbol{k}} = E_{\pm,\boldsymbol{k}}\boldsymbol{w}_{\pm,\boldsymbol{k}}, \tag{3.33}$$

satisfying the property

$$\boldsymbol{w}_{\pm,\boldsymbol{k}}\cdot\boldsymbol{I}\cdot\boldsymbol{w}_{\pm,\boldsymbol{k}} = 1. \tag{3.34}$$

The above-mentioned eigenvalues define the dispersions of the Bogoliubov quasiparticles

$$\begin{aligned}E_{\pm,\boldsymbol{k}}^2 =&\varepsilon_{\boldsymbol{k}}(\varepsilon_{\boldsymbol{k}} + g(n_{0\uparrow}+n_{0\downarrow}))\\ &\pm\varepsilon_{\boldsymbol{k}}\sqrt{g^2(n_{0\uparrow}-n_{0\downarrow})^2 + 4g_{\uparrow\downarrow}^2 n_{0\uparrow}n_{0\downarrow}}.\end{aligned} \tag{3.35}$$

The eigenvectors $\boldsymbol{w}_{\pm,\boldsymbol{k}}$ have the so-called Bogoliubov coherence factors as their entries, or explicitly

$$\boldsymbol{w}_{\pm,\boldsymbol{k}} = (u_{\pm,\boldsymbol{k}}^{\uparrow}, -v_{\pm,\boldsymbol{k}}^{\uparrow}, u_{\pm,\boldsymbol{k}}^{\downarrow}, -v_{\pm,\boldsymbol{k}}^{\downarrow}). \tag{3.36}$$

For the case at hand these coherence factors are rather involved functions of the momentum. Since they have been presented explicitly in Ref. [79], we do not write them out here.

The relation between the two original fluctuation fields and the new Bogoliubov quasiparticle fields is given by

$$\boldsymbol{\Phi}_{\boldsymbol{k}n} = \boldsymbol{W}_{\boldsymbol{k}} \cdot \boldsymbol{\Psi}_{\boldsymbol{k}n}, \tag{3.37}$$

where we have defined the Bogoliubov fields

$$\boldsymbol{\Psi}_{\boldsymbol{k}n} = \left(\psi^*_{+,\boldsymbol{k}n}, \psi_{+,-\boldsymbol{k}n}, \psi^*_{-,\boldsymbol{k}n}, \psi_{-,-\boldsymbol{k}n}\right), \tag{3.38}$$

and the transformation matrix

$$\boldsymbol{W}_{\boldsymbol{k}} = \begin{pmatrix} W^{\uparrow}_{+,\boldsymbol{k}} & W^{\uparrow}_{-,\boldsymbol{k}} \\ W^{\downarrow}_{+,\boldsymbol{k}} & W^{\downarrow}_{-,\boldsymbol{k}} \end{pmatrix}, \tag{3.39}$$

which consists of the submatrices

$$W^{\sigma}_{s,\boldsymbol{k}} = \begin{pmatrix} u^{\sigma}_{s,\boldsymbol{k}} & -v^{\sigma}_{s,\boldsymbol{k}} \\ -v^{\sigma}_{s,\boldsymbol{k}} & u^{\sigma}_{s,\boldsymbol{k}} \end{pmatrix}. \tag{3.40}$$

It is straightforward to check that this transformation leaves the Matsubara-frequency terms in the action unaffected, and therefore the Bogoliubov excitations are bosons. The action becomes

$$\begin{aligned} S = &-\hbar\beta V \left(g_{\uparrow\downarrow} n_{\uparrow} n_{\downarrow} + g(n^2_{\downarrow} + n^2_{\uparrow}) - g\frac{n^2_{0\downarrow} + n^2_{0\uparrow}}{2} \right) \\ &+ \frac{\hbar\beta}{2} \sum_{\boldsymbol{k}\neq 0} \left(E_{+,\boldsymbol{k}} + E_{-,\boldsymbol{k}} - 2\varepsilon_{\boldsymbol{k}} - g(n_{0\uparrow} + n_{0\downarrow}) \right) \\ &+ \sum_{s=\pm} \sum_{\boldsymbol{k}\neq 0,n} (-i\hbar\omega_n + E_{s,\boldsymbol{k}}) \psi^*_{s,\boldsymbol{k}n} \psi_{s,\boldsymbol{k}n}, \end{aligned} \tag{3.41}$$

where $(E_{+,\boldsymbol{k}} + E_{-,\boldsymbol{k}})$ in the second term is again due to the time ordering but this time of the $\psi_{\pm}$ fields.

In the last equation, the first term describes the condensate contribution to the action. The second term (after properly accounting for the fact that the contact potential does not fall off at high momenta) can be shown to describe the so-called Lee-Huang-Yang correction [104, 105] which is small for a weakly interacting gas, and can therefore be safely neglected. The last term describes the Bogoliubov excitations. Evaluating this path integral amounts to a Gaussian integration and can be performed exactly. Finally, we perform the remaining bosonic Matsubara sum [8]

$$\lim_{\eta\to 0^+} \sum_n \log\left[\beta(-i\hbar\omega_n + E_{s,\boldsymbol{k}})\right] e^{i\omega_n\eta} = \log(1 - e^{-\beta E_{s,\boldsymbol{k}}}), \tag{3.42}$$

and arrive at the following expression for the partition function

$$\begin{aligned} Z = \exp\Bigg[&\beta\left(g_{\uparrow\downarrow} n_{\uparrow} n_{\downarrow} + g(n^2_{\downarrow} + n^2_{\uparrow}) - g\frac{n^2_{0\downarrow} + n^2_{0\uparrow}}{2} \right) \\ &- \frac{1}{V} \sum_{s=\pm,\boldsymbol{k}\neq 0} \log(1 - e^{-\beta E_{s,\boldsymbol{k}}}) \Bigg]. \end{aligned} \tag{3.43}$$

The partition function is related to the pressure by

$$\begin{aligned} p(n_{0\uparrow}, n_{0\downarrow}, T) &= -\Omega/V = \frac{1}{\beta}\log(Z) \\ &= g_{\uparrow\downarrow} n_\uparrow n_\downarrow + g(n_\downarrow^2 + n_\uparrow^2) - g\frac{n_{0\downarrow}^2 + n_{0\uparrow}^2}{2} \\ &\quad - \frac{1}{\beta V}\sum_{s=\pm,\boldsymbol{k}\neq 0} \log(1 - e^{-\beta E_{s,\boldsymbol{k}}}), \end{aligned} \tag{3.44}$$

where Ω is the grand potential. We have obtained the (average) particle densities

$$n_\sigma = n_{\sigma 0} + \frac{1}{V}\sum_{s=\pm,\boldsymbol{k}\neq 0} \frac{|u_{s,\boldsymbol{k}}^\sigma|^2 + |v_{s,\boldsymbol{k}}^\sigma|^2}{e^{\beta E_s} - 1} \tag{3.45}$$

from the appropriate Green's functions, while the entropy per volume is[2]

$$\begin{aligned} \frac{S}{V} = -\left.\frac{\partial\Omega}{\partial T}\right|_{n'_\sigma, n_{0\sigma}} &= -\frac{k_B}{V}\sum_{s=\pm,\boldsymbol{k}\neq 0} \log(1 - e^{-\beta E_{s,\boldsymbol{k}}}) \\ &\quad + \frac{k_B}{V}\sum_{s=\pm,\boldsymbol{k}\neq 0} \frac{\beta E_{s,\boldsymbol{k}}}{e^{\beta E_{s,\boldsymbol{k}}} - 1}. \end{aligned} \tag{3.46}$$

For future convenience, we define the entropy per particle as

$$s \equiv \frac{S}{V}\frac{1}{n_\uparrow + n_\downarrow}, \tag{3.47}$$

and also the total chemical potential μ_{tot}, as well as the difference of the chemical potentials

$$\mu_{\text{tot}} = \mu_\uparrow + \mu_\downarrow, \tag{3.48}$$

$$\Delta\mu = \mu_\uparrow - \mu_\downarrow. \tag{3.49}$$

Similarly, we define the total particle density and the difference of the particle densities:

$$n_{\text{tot}} = n_\uparrow + n_\downarrow, \tag{3.50}$$

$$\Delta n = n_\uparrow - n_\downarrow. \tag{3.51}$$

Finally, it is also beneficial to define two additional T matrices

$$g_\pm = g \pm g_{\uparrow\downarrow} = g(1 \pm \gamma), \tag{3.52}$$

2 In the grand-canonical ensemble thermodynamic quantities are obtained by considering the grand potential Ω that explicitly depends on the chemical potentials. In that case, the density is $n_\sigma = -\partial\Omega/\partial\mu_\sigma|_T$, and the entropy per volume is $S/V = -\partial\Omega/\partial T|_{\mu_\sigma}$. We have checked that the quantities obtained that way match the ones given in the main text. The said calculation was not presented here in detail, since the relevant expressions (including the dispersions of the quasiparticles) become rather cumbersome.

where we have also introduced a dimensionless number γ which shows the relative strength between the inter-species and the intra-species repulsion. Note that in the miscible case that we discuss here, $\gamma < 1$.

3.2.2 *Balanced mixture*

Of particular interest is the balanced case, where the number of particles of the two species are equal: $n_\uparrow = n_\downarrow = n$. We consider it in this subsection. An obvious consequence of this limit is

$$n_{0\uparrow} = n_{0\downarrow} \equiv n_0, \tag{3.53}$$

and

$$\mu \equiv \mu_\uparrow = \mu_\downarrow = g_+ n + g n'. \tag{3.54}$$

Moreover, the dispersions of the quasiparticles become

$$E^2_{\pm,\boldsymbol{k}} = \varepsilon_{\boldsymbol{k}}(\varepsilon_{\boldsymbol{k}} + 2n_0 g_\pm), \tag{3.55}$$

and the Bogoliubov transformation matrix simplifies considerably to

$$\boldsymbol{W}_{\boldsymbol{k}} = \begin{pmatrix} W_{+,\boldsymbol{k}} & W_{-,\boldsymbol{k}} \\ W_{+,\boldsymbol{k}} & W_{-,\boldsymbol{k}} \end{pmatrix}, \tag{3.56}$$

which can be inverted to

$$\boldsymbol{W}^{-1}_{\boldsymbol{k}} = \frac{1}{2}\begin{pmatrix} W^{-1}_{+,\boldsymbol{k}} & W^{-1}_{+,\boldsymbol{k}} \\ -W^{-1}_{-,\boldsymbol{k}} & W^{-1}_{-,\boldsymbol{k}} \end{pmatrix}, \tag{3.57}$$

from which we can conclude that the $\psi_{+,\boldsymbol{k}n}$ field has equal contributions from the $\phi_{\uparrow\boldsymbol{k}n}$ and $\phi_{\downarrow\boldsymbol{k}n}$ fields, whereas the latter fields enter $\psi_{-,\boldsymbol{k}n}$ with a relative minus sign but with equal absolute weights. This implies that $\psi_{+,\boldsymbol{k}n}$ describes density-like excitations, whereas $\psi_{-,\boldsymbol{k}}$ describes spin-like excitations. The sub-matrices $W_{s,\boldsymbol{k}}$ in the above are

$$W_{s,\boldsymbol{k}} = \begin{pmatrix} u_{s,\boldsymbol{k}} & -v_{s,\boldsymbol{k}} \\ -v_{s,\boldsymbol{k}} & u_{s,\boldsymbol{k}} \end{pmatrix}, \tag{3.58}$$

where in this case the coherence factors are simple enough to be written out explicitly as

$$v^2_{\pm,\boldsymbol{k}} = \frac{1}{4}\left(\frac{\varepsilon_p + g_\pm n_0}{E_{\pm,\boldsymbol{k}}} - 1\right), \tag{3.59}$$

$$u^2_{\pm,\boldsymbol{k}} = \frac{1}{4}\left(\frac{\varepsilon_p + g_\pm n_0}{E_{\pm,\boldsymbol{k}}} + 1\right). \tag{3.60}$$

Note that the coherence factors are very similar to the single-species case. However, the prefactor (1/4) here is different from the single-species case (1/2), since the transformation now involves four fields instead of two.

We now proceed to discuss the thermodynamic functions of the balanced binary mixture. Throughout the discussion, we consider three different dimensionless interaction parameters $n^{1/3}a = 0.01$, 0.05, and 0.1. They have been chosen to correspond to the experimentally relevant weakly-interacting (far away from Feshbach resonances) ultracold gas situations. In particular, we consider the sodium atom which has several scattering lengths between the accessible hyperfine levels close to 50 Bohr radii [106]. Moreover, we are interested in the hydrodynamic regime, where the density in the center of the trap might become as high as 10^{21} m^{-3} [16] which corresponds to $n^{1/3}a \simeq 0.03$. Comparing thermodynamic quantities calculated within the Bogoliubov theory with the renormalization group results for the single-species case (see Ref. [107]) shows that the two agree very well all the way up to the condensation temperature T_c for $n^{1/3}a = 0.01$. Agreement for $n^{1/3}a = 0.05$ and particularly for 0.1 is less good. However, the qualitative features of the thermodynamic functions are preserved. We expect the situation to be similar for the two-species case.

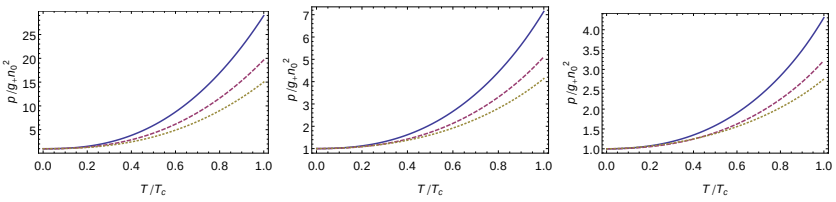

FIGURE 6: Pressure of the two-species balanced gas. The interaction parameter increases from left to right: $n^{1/3}a = 0.01$, 0.05, and 0.1. Inter-component interactions are zero ($\gamma = 0$) for the solid line, moderate ($\gamma = 1/2$) for the dashed line and strong ($\gamma \lesssim 1$) for the dotted line.

We present the equation of state (pressure) in Fig. 6. We scale the pressure plots with the zero-temperature pressure $g_+ n^2/2$ obtained from a Gross-Pitaevskii calculation [4]. For increasing interaction strength, the scaled pressure decreases, since the thermal energy becomes comparable with the interaction energy at higher temperature. For $\gamma = 0$, the pressure is equal to the pressure of a single species of gas with twice the density (see, e.g., Ref. [107] for comparison).

Note that for a fixed total number of particles, the pressure is not a monotonically increasing function of temperature in the Bogoliubov theory as opposed to the Popov theory. This spurious effect appears due to the competition between the depletion of the condensate (decreases pressure) and the population of the thermal states (increases pressure). Moreover, this leads to a spurious lack of avoided crossing of the first- and second-sound velocities,

therefore necessitating the use of at least the Popov theory to describe the sound velocities accurately.

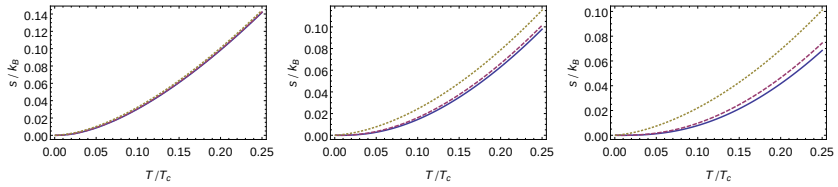

FIGURE 7: The entropy per particle of the two-species balanced gas. The interaction parameter increases from left to right: $n^{1/3}a = 0.01$, 0.05, and 0.1. Inter-component interactions are zero ($\gamma = 0$) for the solid line, moderate ($\gamma = 1/2$) for the dashed line and strong ($\gamma \lesssim 1$) for the dotted line. A limited temperature range is depicted to emphasize the difference between the curves.

The entropy per particle is presented in Fig. 7. Since the system is described by a mixture of non-interacting phonon gases at low temperatures, the entropy per particle shows a T^3 power law behavior at low temperatures. Furthermore, the phonon velocity scales with the interaction strength and therefore stronger-interacting gases have a higher entropy.

3.3 SPIN DRAG IN A PARTIALLY-CONDENSED BOSE GAS

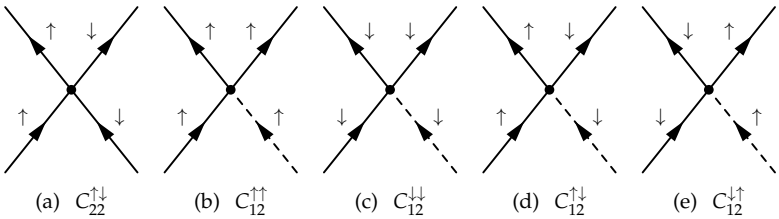

FIGURE 8: Diagrams corresponding to the relevant collision integrals. Full lines depict thermal atoms, while dashed lines represent condensed atoms.

In this section we investigate kinetic (incoherent) processes that contribute to density and velocity dynamics for the balanced binary Bose gas below the critical temperature. We start by generalizing the results of the kinetic theory for a uniform single-species Bose gas (see, for instance, Ref. [108]) to the two-species gas. The collision integrals that we consider below can be formally derived from the Heisenberg equations of motion for the atoms of the two different species. For a detailed discussion of that derivation for the case of a single species we refer to Ref. [109]. The collision integrals discussed in this section conserve the number of $\uparrow$ and $\downarrow$ particles separately.

Since the kinetic processes in question vanish for very low temperatures, and in order to avoid complications posed by the fact that the Bogoliubov transformation mixes the spin species, we work in the Hartree-Fock approximation in this section. The Hartree-Fock approximation is therefore valid for the whole range of temperatures where the collision processes play a significant role. Moreover, here we consider the "local equilibrium" situation where the chemical potentials of the thermal atoms and the condensates are equal to $\mu = g_+ n + g n'$. The thermal atoms thus feel the Hartree-Fock mean-field energy $(g_+ + g)n$. These considerations lead to a Bose-Einstein distribution with a non-zero average momentum $\boldsymbol{p}_{\mathrm{nc}\uparrow}$ ($\boldsymbol{p}_{\mathrm{nc}\downarrow}$) for the non-condensed $\uparrow$ ($\downarrow$) atoms:

$$f_i^{\alpha} = \frac{1}{e^{\beta(\boldsymbol{p}_i - \boldsymbol{p}_{\mathrm{nc}\sigma})^2/2m + \beta(g_+ + g)n - \beta\mu} - 1}, \tag{3.61}$$

where σ labels the spin species, and i labels the momentum variable $\boldsymbol{p}_i$ (the omission of the i label denotes the momentum variable $\boldsymbol{p}$). Furthermore, we allow for different non-zero momenta of the two condensates: the $\uparrow$ ($\downarrow$) condensate has a momentum of $\boldsymbol{p}_{\mathrm{c}\uparrow}$ ($\boldsymbol{p}_{\mathrm{c}\downarrow}$).

In the single species case only one collision process, namely C_{12} using the notation of Ref. [109], is responsible for the relaxation of the difference between the condensate velocity and the velocity of the thermal atoms. However, five different processes (see Fig. 8) can contribute to the dynamics of various densities and velocities in the two-species system leading to the following set of quantum kinetic equations for the distributions of the thermal particles, where we only consider the collisional contributions:

$$\partial_t f^{\uparrow}|_{\mathrm{coll}} = C_{22}^{\uparrow\downarrow} + C_{12}^{\uparrow\uparrow} + C_{12}^{\uparrow\downarrow} + \bar{C}_{12}^{\downarrow\uparrow}, \tag{3.62}$$

$$\partial_t f^{\downarrow}|_{\mathrm{coll}} = \bar{C}_{22}^{\uparrow\downarrow} + C_{12}^{\downarrow\downarrow} + \bar{C}_{12}^{\uparrow\downarrow} + C_{12}^{\downarrow\uparrow}. \tag{3.63}$$

We now discuss the individual collision terms present in these equations. We use a shorthand notation for the momentum integrals $\int_i \equiv \int d^3\boldsymbol{p}_i$ in order to simplify the following formulae. Firstly, we have a spin-drag term (Fig. 8 (a), c.f. Refs. [53, 98]) which only involves scattering between the thermal atoms, and thus exists both below and above the critical temperature:

$$C_{22}^{\uparrow\downarrow} = \int_{1234} A_{22}\left[\delta^{(3)}(\boldsymbol{p} - \boldsymbol{p}_4) - \delta^{(3)}(\boldsymbol{p} - \boldsymbol{p}_1)\right], \tag{3.64}$$

$$\bar{C}_{22}^{\uparrow\downarrow} = \int_{1234} A_{22}\left[\delta^{(3)}(\boldsymbol{p} - \boldsymbol{p}_3) - \delta^{(3)}(\boldsymbol{p} - \boldsymbol{p}_2)\right], \tag{3.65}$$

where we have denoted the common part of the integrand by

$$\begin{aligned} A_{22} = {} & \frac{g_{\uparrow\downarrow}^2}{(2\pi)^5\hbar^7}\delta^{(3)}(\boldsymbol{p}_1 + \boldsymbol{p}_2 - \boldsymbol{p}_3 - \boldsymbol{p}_4) \\ & \times\delta([\boldsymbol{p}_1^2 + \boldsymbol{p}_2^2 - \boldsymbol{p}_3^2 - \boldsymbol{p}_4^2]/2m) \\ & \times\left[f_1^{\uparrow} f_2^{\downarrow}(1+f_3^{\downarrow})(1+f_4^{\uparrow}) - (1+f_1^{\uparrow})(1+f_2^{\downarrow}) f_3^{\downarrow} f_4^{\uparrow}\right]. \end{aligned} \tag{3.66}$$

This term contributes to the relaxation of the difference of momenta $\boldsymbol{p}_{\mathrm{nc}\uparrow} - \boldsymbol{p}_{\mathrm{nc}\downarrow}$. Furthermore, we consider the following intra-species collision terms (Fig. 8 (b) & (c)), which explicitly depend on the condensate density, and thus only exist below the critical temperature:

$$C_{12}^{\uparrow\uparrow(\downarrow\downarrow)} = \int_{123} A_{12}^{\uparrow\uparrow(\downarrow\downarrow)} \big[\delta^{(3)}(\boldsymbol{p}-\boldsymbol{p}_1) - \delta^{(3)}(\boldsymbol{p}-\boldsymbol{p}_2) - \delta^{(3)}(\boldsymbol{p}-\boldsymbol{p}_3)\big], \tag{3.67}$$

where

$$\begin{aligned} A_{12}^{\uparrow\uparrow(\downarrow\downarrow)} =& \frac{2g^2 n_{0\uparrow(\downarrow)}}{(2\pi)^2\hbar^4}\delta^{(3)}(\boldsymbol{p}_1 + \boldsymbol{p}_{\mathrm{c}\uparrow(\downarrow)} - \boldsymbol{p}_2 - \boldsymbol{p}_3) \\ &\times\delta([\boldsymbol{p}_1^2 + \boldsymbol{p}_{\mathrm{c}\uparrow(\downarrow)}^2 - \boldsymbol{p}_2^2 - \boldsymbol{p}_3^2]/2m - g n_{0\uparrow(\downarrow)}) \\ &\times\big[f_1^{\uparrow(\downarrow)}(1+f_2^{\uparrow(\downarrow)})(1+f_3^{\uparrow(\downarrow)}) - (1+f_1^{\uparrow(\downarrow)})f_2^{\uparrow(\downarrow)}f_3^{\uparrow(\downarrow)}\big]. \end{aligned} \tag{3.68}$$

These terms contribute to the dynamics of the condensate fraction, and also describe the relaxation between the condensate velocity and the average thermal particle velocity of the same species. Moreover, we also have similar terms for the inter-species scattering, namely,

$$C_{12}^{\uparrow\downarrow(\downarrow\uparrow)} = \int_{123} A_{12}^{\uparrow\downarrow(\downarrow\uparrow)} \big[\delta^{(3)}(\boldsymbol{p}-\boldsymbol{p}_2) - \delta^{(3)}(\boldsymbol{p}-\boldsymbol{p}_1)\big], \tag{3.69}$$

$$\bar{C}_{12}^{\uparrow\downarrow(\downarrow\uparrow)} = \int_{123} A_{12}^{\uparrow\downarrow(\downarrow\uparrow)} \delta^{(3)}(\boldsymbol{p}-\boldsymbol{p}_3), \tag{3.70}$$

where

$$\begin{aligned} A_{12}^{\uparrow\downarrow(\uparrow\downarrow)} =& \frac{g_{\uparrow\downarrow}^2 n_{0\downarrow(\uparrow)}}{(2\pi)^2\hbar^4}\delta^{(3)}(\boldsymbol{p}_1 + \boldsymbol{p}_{\mathrm{c}\downarrow(\uparrow)} - \boldsymbol{p}_2 - \boldsymbol{p}_3) \\ &\times\delta([\boldsymbol{p}_1^2 + \boldsymbol{p}_{\mathrm{c}\downarrow(\uparrow)}^2 - \boldsymbol{p}_2^2 - \boldsymbol{p}_3^2]/2m - g n_{0\downarrow(\uparrow)}) \\ &\times\big[f_1^{\uparrow(\downarrow)}(1+f_2^{\uparrow(\downarrow)})(1+f_3^{\downarrow(\uparrow)}) - (1+f_1^{\uparrow(\downarrow)})f_2^{\uparrow(\downarrow)}f_3^{\downarrow(\uparrow)}\big]. \end{aligned} \tag{3.71}$$

The latter terms also describe the dynamics of the condensate fraction, as well as describing the relaxation of various velocities mediated by the condensate.

In order to obtain the equations for the change of the density and the momentum of the thermal particles, we perform the following integration of Eqs. (3.62) and (3.63) leading to

$$\partial_t n'_{\uparrow(\downarrow)} = \int \frac{d^3\boldsymbol{p}}{(2\pi\hbar)^3}\partial_t f_{\uparrow(\downarrow)}, \tag{3.72}$$

$$\partial_t (n'_{\uparrow(\downarrow)}\boldsymbol{p}_{\mathrm{nc}\uparrow(\downarrow)}) = \int \frac{d^3\boldsymbol{p}}{(2\pi\hbar)^3}\boldsymbol{p}\partial_t f_{\uparrow(\downarrow)}. \tag{3.73}$$

Adding the equations that change the thermal densities, and the equations that change the condensate densities obtained from straightforward considerations of the collision integrals, we have

$$\partial_t n'_\uparrow = \Gamma_{12}^{\uparrow\uparrow} + \bar{\Gamma}_{12}^{\downarrow\uparrow}, \tag{3.74}$$

$$\partial_t n'_\downarrow = \Gamma_{12}^{\downarrow\downarrow} + \bar{\Gamma}_{12}^{\uparrow\downarrow}, \tag{3.75}$$

$$\partial_t n_{0\uparrow} = -\Gamma_{12}^{\uparrow\uparrow} - \bar{\Gamma}_{12}^{\downarrow\uparrow}, \tag{3.76}$$

$$\partial_t n_{0\downarrow} = -\Gamma_{12}^{\downarrow\downarrow} - \bar{\Gamma}_{12}^{\uparrow\downarrow}, \tag{3.77}$$

where

$$\Gamma_{12}^{\uparrow\uparrow(\downarrow\downarrow)} = -\frac{1}{(2\pi\hbar)^3}\int_{123} A_{12}^{\uparrow\uparrow(\downarrow\downarrow)}, \tag{3.78}$$

$$\bar{\Gamma}_{12}^{\uparrow\downarrow(\downarrow\uparrow)} = \frac{1}{(2\pi\hbar)^3}\int_{123} A_{12}^{\uparrow\downarrow(\uparrow\downarrow)}, \tag{3.79}$$

and we see that the total densities $n_{\uparrow(\downarrow)}$ are conserved separately. In a similar manner, the equations for the change of momenta are

$$\begin{aligned}\partial_t(n'_\uparrow \boldsymbol{p}_{\mathrm{nc}\uparrow}) &= \frac{1}{(2\pi\hbar)^3}\int_{1234}(\boldsymbol{p}_4-\boldsymbol{p}_1)A_{22} - \boldsymbol{p}_{\mathrm{c}\uparrow}\Gamma_{12}^{\uparrow\uparrow} \\ &+\frac{1}{(2\pi\hbar)^3}\int_{123}(\boldsymbol{p}_2-\boldsymbol{p}_1)A_{12}^{\uparrow\downarrow} + \frac{1}{(2\pi\hbar)^3}\int_{123}\boldsymbol{p}_3 A_{12}^{\downarrow\uparrow},\end{aligned} \tag{3.80}$$

$$\begin{aligned}\partial_t(n'_\downarrow \boldsymbol{p}_{\mathrm{nc}\downarrow}) &= -\frac{1}{(2\pi\hbar)^3}\int_{1234}(\boldsymbol{p}_4-\boldsymbol{p}_1)A_{22} - \boldsymbol{p}_{\mathrm{c}\downarrow}\Gamma_{12}^{\downarrow\downarrow} \\ &+\frac{1}{(2\pi\hbar)^3}\int_{123}\boldsymbol{p}_3 A_{12}^{\uparrow\downarrow} + \frac{1}{(2\pi\hbar)^3}\int_{123}(\boldsymbol{p}_2-\boldsymbol{p}_1)A_{12}^{\downarrow\uparrow},\end{aligned} \tag{3.81}$$

$$\partial_t(n_{0\uparrow}\boldsymbol{p}_{\mathrm{c}\uparrow}) = \boldsymbol{p}_{\mathrm{c}\uparrow}\Gamma_{12}^{\uparrow\uparrow} + \boldsymbol{p}_{\mathrm{c}\uparrow}\Gamma_{12}^{\downarrow\uparrow}, \tag{3.82}$$

$$\partial_t(n_{0\downarrow}\boldsymbol{p}_{\mathrm{c}\downarrow}) = \boldsymbol{p}_{\mathrm{c}\downarrow}\Gamma_{12}^{\downarrow\downarrow} + \boldsymbol{p}_{\mathrm{c}\downarrow}\Gamma_{12}^{\uparrow\downarrow}. \tag{3.83}$$

Note that the total momentum is conserved, thus

$$\partial_t(n'_\uparrow \boldsymbol{p}_{\mathrm{nc}\uparrow} + n'_\downarrow \boldsymbol{p}_{\mathrm{nc}\downarrow} + n_{0\uparrow}\boldsymbol{p}_{\mathrm{c}\uparrow} + n_{0\downarrow}\boldsymbol{p}_{\mathrm{c}\downarrow}) = 0. \tag{3.84}$$

For the hydrodynamic theory in the subsequent chapter, we are interested in the linearization of the collision integrals in terms of the velocity differences. It is straightforward to show that all the $\Gamma_{12}^{\alpha\beta}$ integrals are at least quadratic in terms of the momenta, and, therefore, in linear response the densities stay constant for both species and $\partial_t n'_\alpha = \partial_t n_{0\alpha} = 0$. In addition, this result implies that the condensate momentum experiences no linear relaxation. This is consistent with the common physical intuition that the condensate motion should not decay in the lowest order, as the condensate motion corresponds to the flow of a superfluid.

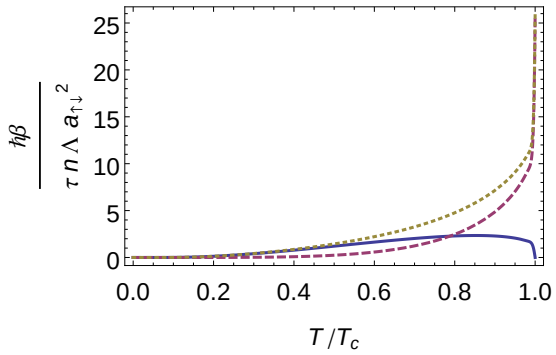

FIGURE 9: Condensate-assisted (solid line), thermal (dashed line), and total (dotted line) spin-drag rates for a system of sodium atoms at a density of 10^{21} m^{-3}, $\gamma \simeq 1$, $n^{1/3}a = 0.03$.

Nevertheless, the momentum difference between the two species of thermal particles experiences relaxation:

$$\begin{aligned}\partial_t(\boldsymbol{p}_{\mathrm{nc}\uparrow} - \boldsymbol{p}_{\mathrm{nc}\downarrow}) &= -\left(\frac{1}{\tau_{22}} + \frac{1}{\tau_{12}}\right)(\boldsymbol{p}_{\mathrm{nc}\uparrow} - \boldsymbol{p}_{\mathrm{nc}\downarrow}) \\ &= -\frac{1}{\tau_{\mathrm{sd}}}(\boldsymbol{p}_{\mathrm{nc}\uparrow} - \boldsymbol{p}_{\mathrm{nc}\downarrow}),\end{aligned} \tag{3.85}$$

where we have also defined the total spin-drag rate $1/\tau_{\mathrm{sd}}$ in terms of the thermal and condensate-assisted spin-drag relaxation rates $1/\tau_{22}$ and $1/\tau_{12}$, respectively. While the thermal spin-drag relaxation time

$$\begin{aligned}\frac{\hbar\beta}{\tau_{22} n \Lambda a_{\uparrow\downarrow}^2} &= \frac{1}{6\pi^2}\frac{1}{(n\Lambda^3)^2}\int_0^\infty \frac{dq\, d\omega\, q^2}{\sinh^2(\omega/2)} \\ &\times \log\left(\frac{e^{q^2/16\pi + \beta g n_0 - \omega/2 + \pi\omega^2/q^2} - e^{-\omega}}{e^{q^2/16\pi + \beta g n_0 - \omega/2 + \pi\omega^2/q^2} - 1}\right)^2\end{aligned} \tag{3.86}$$

has been calculated before in Ref. [110] for the temperatures above the condensation temperature, the condensate-assisted spin-drag rate

$$\begin{aligned}\frac{\hbar\beta}{\tau_{12} n \Lambda a_{\uparrow\downarrow}^2} &= \frac{64}{3(2\pi)^3}\frac{n_0}{n}\frac{a}{\Lambda}\int_0^\infty dp_1\, dp_3\, p_1\, p_3^3 \\ &\times \left(1 + \frac{1}{e^{(p_1^2+p_3^2)/4\pi + 2\beta g n_0} - 1}\right) \\ &\times \frac{1}{e^{p_1^2/4\pi + \beta g n_0} - 1}\frac{1}{e^{p_3^2/4\pi + \beta g n_0} - 1}\Theta\left(\frac{p_1 p_3}{2\pi} - \beta g n_0\right),\end{aligned} \tag{3.87}$$

where Θ denotes the Heaviside theta function, has not been investigated before. As we can expect, the thermal spin-drag rate $1/\tau_{22}$ dominates at high

temperatures, while the condensate-assisted spin-drag rate $1/\tau_{12}$ is more important at low temperatures (see Fig. 9). Even though in our approximation the thermal spin-drag rate has a maximum at the critical temperature, a more careful calculation leads to its suppression due to critical fluctuations [111] in a very narrow temperature window around T_c. Therefore, strictly speaking, $1/\tau_{12}$ and $1/\tau_{22}$ vanish both at $T = 0$ and $T = T_c$.

3.4 HYDRODYNAMIC THEORY FOR A BALANCED BINARY MIXTURE

The goal of this section is to derive a set of hydrodynamic equations for a balanced mixture of two components, where each of the components has a superfluid part and a normal part. Note that the following discussion is in principle not limited to weakly interacting Bose gases, since it is only based on conservation laws. However, we do not discuss various dissipative terms such as the thermal diffusivity or the (second) viscosity [1, 112, 16, 72], with the exception of the spin-drag term. Furthermore, in the previous section we have concluded that the spin-drag term only relaxes the non-condensate spin currents, whereas in what follows we discuss the hydrodynamics in terms of superfluid and non-superfluid (normal) currents. Therefore, we posit that the non-superfluid spin currents relax in exactly the same manner as the non-condensate spin currents. This is an approximation, which is only valid in weakly-interacting systems, where the condensate and the superfluid are very similar objects.

In the equilibrium situation, the particle densities of the two components are identical for both the superfluid ($n_\uparrow^{\mathrm{sf}} = n_\downarrow^{\mathrm{sf}} \equiv n^{\mathrm{sf}}$) and the normal fluid ($n_\uparrow^{\mathrm{nf}} = n_\downarrow^{\mathrm{nf}} \equiv n^{\mathrm{nf}}$), and therefore the total densities of each species are identical, too ($n_\uparrow = n_\uparrow^{\mathrm{sf}} + n_\uparrow^{\mathrm{nf}} = n_\downarrow$). Moreover, in equilibrium there are no particle currents $\boldsymbol{j}_\uparrow^{\mathrm{nf}} = \boldsymbol{j}_\downarrow^{\mathrm{nf}} = \boldsymbol{j}_\uparrow^{\mathrm{sf}} = \boldsymbol{j}_\downarrow^{\mathrm{sf}}$, as all the velocities vanish: $\boldsymbol{v}_\uparrow^{\mathrm{nf}} = \boldsymbol{v}_\downarrow^{\mathrm{nf}} = \boldsymbol{v}_\uparrow^{\mathrm{sf}} = \boldsymbol{v}_\downarrow^{\mathrm{sf}}$, where the normal current of the $\uparrow$ component is defined as $\boldsymbol{j}_\uparrow^{\mathrm{nf}} = n_\uparrow^{\mathrm{nf}} \boldsymbol{v}_\uparrow^{\mathrm{nf}}$, and the other currents are defined similarly. The current of each of the components is the sum of the superfluid and normal currents: $\boldsymbol{j}_\uparrow = \boldsymbol{j}_\uparrow^{\mathrm{sf}} + \boldsymbol{j}_\uparrow^{\mathrm{nf}}$.

In the non-equilibrium situation, however, both the velocities and the various densities can be non-zero and different from each other. In that case, it is useful to define variables pertaining to the combined motion of the whole gas, and contrast them to the variables that describe the relative motion. Therefore,

$$\boldsymbol{j}_{\mathrm{tot}}^{\mathrm{nf,sf}} = \boldsymbol{j}_\uparrow^{\mathrm{nf,sf}} + \boldsymbol{j}_\downarrow^{\mathrm{nf,sf}}, \tag{3.88}$$

are the total normal and superfluid currents of the combined motion, respectively. Adding these two currents up yields the total particle current $\boldsymbol{j}_{\mathrm{tot}} = \boldsymbol{j}_{\mathrm{tot}}^{\mathrm{nf}} + \boldsymbol{j}_{\mathrm{tot}}^{\mathrm{sf}}$. Furthermore, we are now in a position to define the combined velocities such that

$$\boldsymbol{j}_{\mathrm{tot}}^{\mathrm{nf}} \equiv n_{\mathrm{tot}}^{\mathrm{nf}} \boldsymbol{v}_{\mathrm{tot}}^{\mathrm{nf}}, \tag{3.89}$$

and

$$\boldsymbol{j}_{\mathrm{tot}}^{\mathrm{sf}} \equiv n_{\mathrm{tot}}^{\mathrm{sf}} \boldsymbol{v}_{\mathrm{tot}}^{\mathrm{sf}}. \tag{3.90}$$

Note also that thermodynamic functions (e.g., pressure and entropy) are defined for the whole system only, and not for the individual components. Moreover, due to time-reversal invariance, the lowest-order velocity corrections to thermodynamic functions are quadratic [1], and therefore do not enter linear equations. For example, the Gibbs-Duhem relation reads

$$n_{\uparrow} d\mu_{\uparrow} + n_{\downarrow} d\mu_{\downarrow} + s dT = dp \tag{3.91}$$

even in the case of non-zero velocities. Hence, we obtain the following linearized hydrodynamic equations for the combined (or in-phase) motion of the whole gas:

$$\partial_t n_{\mathrm{tot}} + \boldsymbol{\nabla} \cdot \boldsymbol{j}_{\mathrm{tot}} = 0, \tag{3.92}$$

$$\partial_t (n_{\mathrm{tot}} s) + n_{\mathrm{tot}} s \boldsymbol{\nabla} \cdot \boldsymbol{v}_{\mathrm{tot}}^{\mathrm{nf}} = 0, \tag{3.93}$$

$$m \partial_t \boldsymbol{j}_{\mathrm{tot}} + \boldsymbol{\nabla} p = 0, \tag{3.94}$$

$$m \partial_t \boldsymbol{v}_{\mathrm{tot}}^{\mathrm{sf}} + \boldsymbol{\nabla} \mu_{\mathrm{tot}} = 0. \tag{3.95}$$

These simple equations express particle conservation, entropy conservation, Newton's second law, and the Josephson relation, respectively. Note that the terms "in-phase" and "out-of-phase" in this paper refer to the motion of the two spin components, as opposed to the normal and the superfluid component, where the latter meaning is common in the literature concerning liquid helium.

We now turn our attention to the relative motion of the up and down particles. To that end, we define the normal and superfluid spin densities

$$\Delta n^{\mathrm{sf,nf}} = n_{\uparrow}^{\mathrm{sf,nf}} - n_{\downarrow}^{\mathrm{sf,nf}}, \tag{3.96}$$

as well as spin currents

$$\Delta \boldsymbol{j}^{\mathrm{sf,nf}} = \boldsymbol{j}_{\uparrow}^{\mathrm{nf,sf}} - \boldsymbol{j}_{\downarrow}^{\mathrm{nf,sf}}. \tag{3.97}$$

Using these newly defined quantities, the hydrodynamic spin equations are the following:

$$\partial_t \Delta n^{\mathrm{nf}} + \boldsymbol{\nabla} \cdot \Delta \boldsymbol{j}^{\mathrm{nf}} = 0, \tag{3.98}$$

$$\partial_t \Delta n^{\mathrm{sf}} + \boldsymbol{\nabla} \cdot \Delta \boldsymbol{j}^{\mathrm{sf}} = 0, \tag{3.99}$$

$$\partial_t \Delta \boldsymbol{j}^{\mathrm{nf}} + n_{\mathrm{tot}}^{\mathrm{nf}} \boldsymbol{\nabla} \Delta\mu / 2m = -\Delta \boldsymbol{j}^{\mathrm{nf}} / \tau_{sd}, \tag{3.100}$$

$$\partial_t \Delta \boldsymbol{j}^{\mathrm{sf}} + n_{\mathrm{tot}}^{\mathrm{sf}} \boldsymbol{\nabla} \Delta\mu / 2m = 0. \tag{3.101}$$

The four equations above state that both normal and superfluid spin densities are conserved, the normal spin current is driven by a chemical potential

difference and relaxes with the spin-drag rate, whereas the superfluid spin current is also driven by a chemical potential difference but does not relax.

By eliminating all the currents and velocities from the equations above and noticing that for the balanced case

$$\frac{\partial \Delta\mu}{\partial T} = \frac{\partial \Delta\mu}{\partial n} = 0, \tag{3.102}$$

we find that

$$m\partial_t^2 n_{\rm tot} = \boldsymbol{\nabla}^2 p, \tag{3.103}$$

$$m\partial_t^2 s = \frac{n^{\rm sf}}{n^{\rm nf}} s^2 \boldsymbol{\nabla}^2 T, \tag{3.104}$$

$$\partial_t^2 \Delta n^{\rm nf} + \frac{1}{\tau_{sd}}\partial_t \Delta n^{\rm nf} = \frac{n^{\rm nf}}{m}\frac{\partial \Delta\mu}{\partial \Delta n}\boldsymbol{\nabla}^2(\Delta n^{\rm nf} + \Delta n^{\rm sf}), \tag{3.105}$$

$$\partial_t^2 \Delta n^{\rm sf} = \frac{n^{\rm sf}}{m}\frac{\partial \Delta\mu}{\partial \Delta n}\boldsymbol{\nabla}^2(\Delta n^{\rm nf} + \Delta n^{\rm sf}). \tag{3.106}$$

We now employ a traveling-wave ansatz for the total density

$$n_{\rm tot} = n_{\rm tot,eq} + \delta n_{\rm tot}\exp(-i[\omega t - \boldsymbol{k}\cdot\boldsymbol{x}]), \tag{3.107}$$

where $n_{\rm tot,eq}$ is the total density in the equilibrium, and $\delta n_{\rm tot}$ is the amplitude of the wave. Proceeding similarly for the other quantities, we obtain the lowest-lying collective modes for the system. Note that in this balanced situation the in-phase collective modes (first and second sounds) are decoupled from the out-of-phase modes (spin modes).

3.5 RESULTS

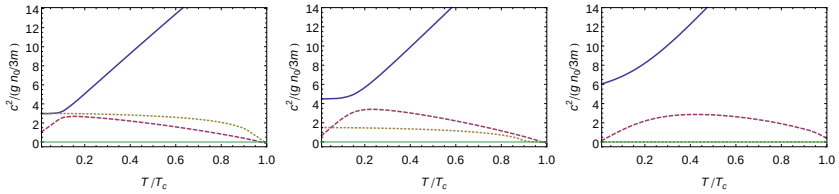

FIGURE 10: Square of the sound velocities of the two-species balanced Bose gas scaled to the zero-temperature second-sound velocity of a single species. Here $n^{1/3}a = 0.03$. The inter-component interactions are increasing from left to right: $\gamma = 0$ (left), $\gamma = 1/2$ (center), and $\gamma \lesssim 1$ (right). The latter corresponds to a mixture of hyperfine states of the sodium atom with the density of 10^{21} m^{-3}. The first-sound velocity is depicted by the thick solid line, the second-sound velocity is the dashed line. The spin-sound velocities are the dotted and the thin solid lines.

In this section we present the results of our calculations, most important of which are the sound velocities of the various modes. We discuss both the uniform and trapped cases. From the total number of hydrodynamic equations,

we expect four modes: two in-phase modes and two out-of-phase modes. The two in-phase modes are present in any system where entropy transport is distinct from density transport: they are the first- and the second-sound modes. It is worthwhile to note that the phenomenon of the second sound has been reported not only in superfluid helium, but in other systems as well, including solid helium [113], dielectric crystals [114], and more recently in a unitary Fermi gas [69]. Moreover, contrary to the case of superfluid helium, second sound in weakly interacting gases is not a pure entropy wave, as discussed below. On the other hand, the out-of-phase modes are similar to spin modes, and therefore only occur in systems with several species of particles.

3.5.1 *Collective modes in a uniform gas*

In the case of no spin drag, all the collective modes of the system have a linear dispersion

$$\omega = c_i k, \tag{3.108}$$

where c_i are the sound velocities. At zero temperature, the first-sound velocity can be calculated from the expression of pressure in Eq. (3.44), yielding

$$c_1^2 = \frac{g_+ n}{m} = \frac{(1+\gamma)gn}{m}. \tag{3.109}$$

Moreover, the second-sound velocity can be calculated in a manner similar to the single-component case (see Ref. [4] for an explicit calculation), the only difference being that instead of a single phonon gas, we have to consider a mixture of two non-interacting phonon gases, leading to

$$c_2^2 = \frac{gn}{3m} \frac{(1+\gamma)(1-\gamma)^{5/2} + (1-\gamma)(1+\gamma)^{5/2}}{(1-\gamma)^{5/2} + (1+\gamma)^{5/2}}. \tag{3.110}$$

When the two components are decoupled ($\gamma = 0$), we recover the single species result $c_2^2 = gn/3m$ from the formula above. Furthermore, in the strong-coupling limit ($\gamma \lesssim 1$), the sound velocity vanishes ($c_2^2 \simeq 0$), signaling the demixing transition. When it comes to the spin sounds, one of them always has a zero velocity, whereas the other one has the velocity

$$c_s^2 = \frac{g_- n}{m} = \frac{(1-\gamma)gn}{m}, \tag{3.111}$$

as can be seen from the difference of chemical potentials, in Eq. (3.22). Note that c_1 and c_s can also be obtained by expanding the energies of the Bogoliubov excitations in Eq. (3.55) to the lowest order in momentum. Therefore, the first sound and the spin sound can be thought of as both quasiparticles and collective modes at zero temperature.

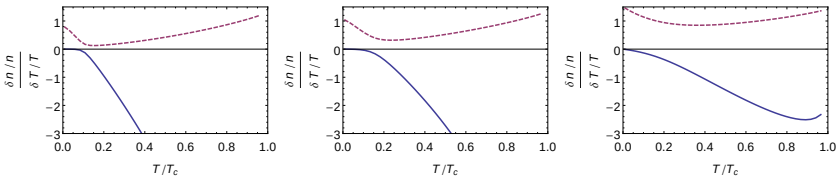

FIGURE 11: Ratio of density and temperature fluctuations present in first sound (solid line) and second sound (dashed line) for $n^{1/3}a = 0.03$. Inter-component interactions are increasing from left to right: $\gamma = 0$ (left), $\gamma = 1/2$ (center), and $\gamma \lesssim 1$ (right). The latter corresponds to a mixture of hyperfine states of the sodium atom with the density of 10^{21} m^{-3}.

We present the velocities of the sound modes for different temperatures in Fig. 10. In order to characterize the sound modes, we have calculated the amplitudes of the temperature and density perturbations from the eigenvectors of the linearized system (see Fig. 11). We observe that for the temperatures below the avoided crossing, first sound is mostly a temperature wave. However, above the avoided crossing temperature, first sound is predominantly a density wave. Second sound has comparable contributions from both relative temperature and density deviations for any temperature. Furthermore, second sound is a wave where density and temperature change in-phase, while first sound describes an out-of-phase change (the temperature increases with decreasing density), as signified by a minus sign in Fig. 11. When it comes to the spin modes, a zero-frequency mode exists, which corresponds to

$$\Delta n^{\mathrm{nf}} = -\Delta n^{\mathrm{sf}}, \tag{3.112}$$

and does not affect the total density of either component. The other spin mode, however, affects the total spin density, while the normal component contributes with the same relative weight as the superfluid component:

$$\frac{\Delta n^{\mathrm{nf}}}{n^{\mathrm{nf}}} = \frac{\Delta n^{\mathrm{sf}}}{n^{\mathrm{sf}}}. \tag{3.113}$$

Upon accounting for spin drag, we find that the zero-frequency modes split into two: one zero-frequency mode and one purely imaginary mode. The purely imaginary mode (c.f. Fig. 12) at low momenta is an excitation with only normal density fluctuations, whereas at higher momenta it preserves the total density of every component as the zero-frequency mode: $\Delta n^{\mathrm{nf}} = -\Delta n^{\mathrm{sf}}$. Furthermore, the dispersion of the other spin mode develops a quadratic imaginary part even though its real velocity c_s is almost unaffected by spin drag and the mode is still characterized by Eq. (3.113). The frequency ω of the latter mode at long wavelengths can be written as

$$\omega = c_s k - iDk^2, \tag{3.114}$$

where k is the wavenumber and D is the diffusion coefficient. Hence, we call this mode the complex spin mode in Fig. 12.

Since all the interaction strengths are similar ($\gamma \simeq 1$) in a sodium gas, when spin drag is absent, both spin modes have zero frequency. In particular, the spin sound has zero velocity at any temperature, $c_s \simeq 0$, which is consistent with the zero-temperature result in Eq. (3.111). When spin drag is present, the purely imaginary mode has a constant imaginary frequency $\omega = -i/\tau_{sd}$, while the complex mode frequency remains zero, and no imaginary part develops, so $D \simeq 0$ in this case. In a realistic sodium gas with a density of 10^{21} m^{-3} at half of the critical temperature, the total spin-drag rate is $1/\tau_{\rm sd} \simeq 1$ kHz, while in experiments of trapped sodium gas [98] above T_c typical rates are on the order of 0.1 kHz. Therefore, it should be experimentally possible to measure the spin-drag rate below the critical temperature by measuring the spin-wave decay time.

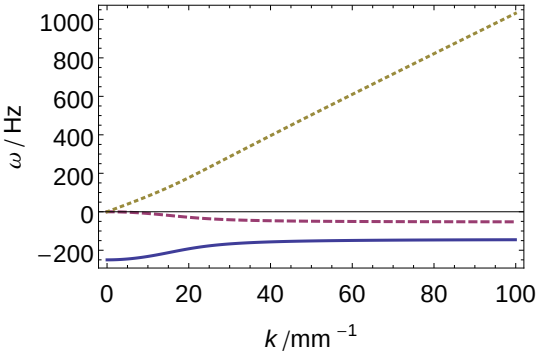

FIGURE 12: Spin modes in the $n^{1/3}a = 0.03$ case at $T = T_c/2$ for nonzero interspecies interactions ($\gamma = 1/2$, $1/\tau_{sd} = 0.25$kHz). The solid line depicts the imaginary mode, whereas the dashed and dotted lines depict the imaginary and the real parts of the complex spin mode. The horizontal axis corresponds to the physically relevant wavelengths down to about 10μm.

3.5.2 *Gas in a trap*

We now turn our attention to the experimentally relevant trapped case. Here we consider a cylindrically-symmetric trap which is highly anisotropic. This trap, where one (axial) direction is very shallow, and the other two (radial) directions are much more strongly confined, puts the gas in the hydrodynamic regime in the axial direction even in the presence of weak interactions. Therefore, we perform the trap average in the radial direction and analyze the propagation of excitations in the axial direction. To that end, we work in the semi-classical approximation (see Ref. [4] for more details). The condensate is treated in the Thomas-Fermi approximation and the excitations are treated in the Hartree-Fock approximation. Therefore, both components are treated in the local-density approximation. We consider the experimentally relevant sit-

uation [16] of $2 \cdot 10^9$ sodium atoms in a trap with an axial trapping frequency of $2\pi \times 2$ Hz and a radial trapping frequency of $2\pi \times 100$ Hz, and extract the radial profile at the center of the trap from this calculation. We then perform an average on all the thermodynamic quantities of the hydrodynamic Eqs. (3.103) – (3.106). The resulting sound velocities are presented in Fig. 13. At zero temperature, the first-sound velocity in a trap is suppressed by a factor of $\sqrt{2}$ as compared to the uniform case, since the average density in the trap is half of the peak density in the Thomas-Fermi approximation, i.e.,

$$\langle n_0 \rangle = n_0/2, \tag{3.115}$$

as first pointed out by Zaremba [115]. Since at zero temperature the second-sound velocity is also proportional to the square-root of the density, it is suppressed by the same factor of $\sqrt{2}$. This is not explicit for sodium atoms as the second sound at zero temperature vanishes. However, for a non-zero temperature we have not succeeded in finding a similar simple relation between the trapped and uniform gases. Finally, we also present the spin-drag rate dependence on temperature for a trapped system (Fig. 14). The curves are qualitatively similar to the uniform case, even though the rates are decreased by a factor of about 10.

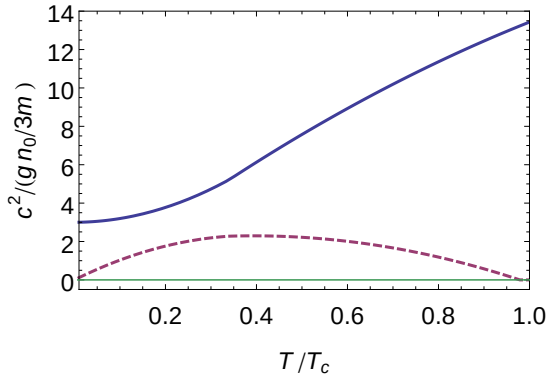

FIGURE 13: Trap averaged sound velocities normalized to the peak density in the trap with no damping (see text for details).

3.6 CONCLUSION

In summary, we have constructed a hydrodynamic theory of a balanced two-species Bose mixture. We have also calculated the microscopic thermodynamic parameters entering that theory using the Popov approximation, obtaining the equation of state on the way. Moreover, we have accounted for the relaxation of the normal current by the spin-drag mechanism, considering the condensate-mediated spin-drag term for the first time. Adding these com-

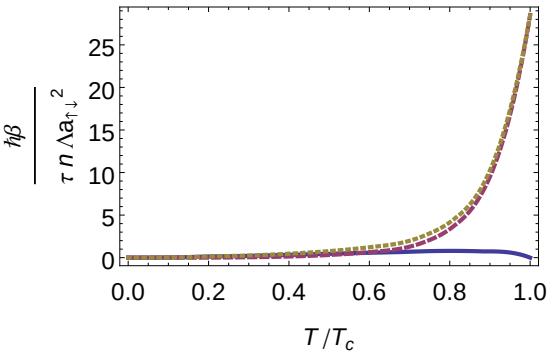

FIGURE 14: Trap averaged condensate-assisted (solid line), thermal (dashed line), and total (dotted line) spin-drag rates normalized to the peak density in the trap (see text for details).

ponents together we were able to calculate the sound velocities and spin-drag rates for the experimentally accessible system of sodium atoms in a trap. We hope that our analysis will stimulate experimental work on hydrodynamic modes and spin drag in a partially-condensed Bose mixture.

4

DEPENDENCE OF THE BOSE-EINSTEIN CONDENSATION TEMPERATURE ON THE PHASE-SPACE BERRY CURVATURE IN SYSTEMS WITH SYNTHETIC SPIN-ORBIT COUPLING

In this chapter we evaluate the dependence of the Bose-Einstein condensation temperature of a non-interacting gas in a trap on the phase-space Berry curvature using the gradient expansion of the Green's function.

4.1 INTRODUCTION

When a system is subjected to an adiabatic cycle, the slow change of the cyclic parameter results in a geometric phase of the wave function which is determined by the geometrical properties of parameter space [25]. This phase is called the Berry phase, and it appears in addition to the usual dynamical phase that is governed by the energy of the state. In the simplest case, the adiabatic parameter is the real-space coordinate of the particle. This situation is encountered, for instance, when a spinful particle passes through a region with a non-uniform magnetization. If the spin of the particle follows the position-dependent magnetization adiabatically, given a non-trivial geometry of the magnetization texture, a real-space Berry curvature is generated. The latter gives rise to geometric forces (see Chapter 2 and Ref. [116] for more details).

However, this phenomenon is more general. In particular, the Berry curvature does not have to come from the coordinate space. For example, a nonzero momentum-space (or reciprocal-space) Berry curvature can be produced by a particular form of the spin-orbit interaction [117] and result in, e.g., the anomalous Hall effect [118]. In some solid-state materials the spin-orbit interaction occurs naturally, but that is not the case in ultracold-atom systems where it has to be artificially engineered.

Recently, a lot of theoretical work concentrated on efficiently inducing different varieties of the spin-orbit interaction in ultracold-atom systems. Typically, lasers are used to couple different atomic states (see Ref. [31] for a review). A particular kind of the spin-orbit interaction (equal Rashba - Dresselhaus) has also been demonstrated experimentally in both Bose [119] and Fermi [120, 121] gases. Achieving a high level of control over the artificial spin-orbit interaction holds promise for realizing non-Abelian gauge potentials, dynamic gauge fields, topological states of matter, and creating analogs of exotic condensed-matter systems with ultracold gases [122]. Most of these

proposals rely on the ability to attain a certain momentum-space Berry curvature by designing the desirable form of the spin-orbit interaction.

Furthermore, Berry curvature in phase space (combined real-space and momentum-space) has been investigated as well in the context of solid-state materials. In particular, it has been shown to alter the density of states of the system [123, 124]. Moreover, it has been proposed that this change of the density of states in a skyrmion-lattice phase leads to redistribution of electrical charge in the vicinity of a skyrmion [125].

In ultracold bosonic systems, the obvious detector of the density of states is the Bose-Einstein condensation temperature. Indeed, the condensation temperature of a homogeneous Bose gas in a constant volume increases with the number of particles to the power $2/3$, while this power is $1/3$ in the harmonically trapped gas, a difference that is caused by the difference in energy dependence of the density of states [8]. Therefore, we expect that the Bose-Einstein condensation temperature is influenced by the phase-space Berry curvature. The aim of this chapter is to quantify this dependence in a harmonically trapped non-interacting Bose gas.

4.2 GRADIENT EXPANSION

We tackle the problem by means of a gradient expansion of the Green's function. A similar treatment for the Fermi gas was presented in Ref. [125]. The system that we consider is described by the following Hamiltonian:

$$H^{\alpha\beta} = \varepsilon_{\boldsymbol{p}}\delta^{\alpha\beta} + \Delta\boldsymbol{\sigma}^{\alpha\beta}\cdot\boldsymbol{m}, \tag{4.1}$$

where $\varepsilon_{\boldsymbol{p}} = \boldsymbol{p}^2/2M$ is the energy of a particle with the mass M and momentum $\boldsymbol{p}$, $\Delta\boldsymbol{m}$ is an effective magnetic field with magnitude Δ in the direction determined by the unit vector $\boldsymbol{m}$, and $\boldsymbol{\sigma}^{\alpha\beta}$ is the vector of the Pauli matrices, where the superscripts indicate the spin structure of the matrix. Note that the magnetic field here in general depends both on the position (real-space magnetic field) and the momentum (spin-orbit coupling) of the particle.

In what follows we consider various quantities after performing the Wigner transform (for further details on that subject we refer to Ref. [126]), and indicate these by tildes. In particular, the Wigner-transformed inverse Green's function $\tilde{K}$ obtained from the Hamiltonian is

$$\hbar\tilde{K}(\omega;\boldsymbol{R},\boldsymbol{p})^{\alpha\beta} = \left[\hbar\omega - \varepsilon_{\boldsymbol{p}}\right]\delta^{\alpha\beta} - \Delta(\boldsymbol{R},\boldsymbol{p})\boldsymbol{\sigma}^{\alpha\beta}\cdot\boldsymbol{m}(\boldsymbol{R},\boldsymbol{p}), \tag{4.2}$$

where we have emphasized that both the magnitude and the direction of the (effective) magnetic field can depend on the position and the momentum. The vector $\boldsymbol{R}$ here should be understood as the position of the center of the wavepacket of the particle. We now employ the following property of the Wigner transform

$$\widetilde{AB}(\omega;\boldsymbol{R},\boldsymbol{p}) = e^{i(\overleftarrow{\boldsymbol{\nabla}}_R\cdot\overrightarrow{\boldsymbol{\nabla}}_p - \overleftarrow{\boldsymbol{\nabla}}_p\cdot\overrightarrow{\boldsymbol{\nabla}}_R)/2}\tilde{A}(\omega;\boldsymbol{R},\boldsymbol{p})\tilde{B}(\omega;\boldsymbol{R},\boldsymbol{p}), \tag{4.3}$$

where $\overleftarrow{\nabla}^i_R$ denotes the position derivative in the i direction that is to be applied only on the first (left) term following the derivative, and similarly for the other derivatives. Specifically,

$$e^{i(\overleftarrow{\boldsymbol{\nabla}}_R\cdot\vec{\boldsymbol{\nabla}}_p-\overleftarrow{\boldsymbol{\nabla}}_p\cdot\vec{\boldsymbol{\nabla}}_R)/2}\tilde{K}^{\alpha\beta}\tilde{G}^{\beta\gamma}=\delta^{\alpha\gamma}. \tag{4.4}$$

Assuming that the spatial variation of $\tilde{K}$ and thus $\tilde{G}$ is small, we expand the Green's function up to the first order in gradients

$$\tilde{G}=\tilde{G}_0+\tilde{G}_1, \tag{4.5}$$

and we also expand Eq. (4.4) up to the first order:

$$\left[1+i(\overleftarrow{\boldsymbol{\nabla}}_R\cdot\vec{\boldsymbol{\nabla}}_p-\overleftarrow{\boldsymbol{\nabla}}_p\cdot\vec{\boldsymbol{\nabla}}_R)/2\right]\left[\tilde{K}^{\alpha\beta}(\tilde{G}_0+\tilde{G}_1)^{\beta\gamma}\right]=\delta^{\alpha\gamma}. \tag{4.6}$$

This expansion results in the point-wise (local) inverse of $\tilde{K}$ which is the lowest order of the Green's function, $\tilde{G}_0=\tilde{K}^{-1}$. If we take $\Delta>0$, the spin of the eigenstates is aligned along (and against) the direction of the effective magnetic field,

$$\boldsymbol{m}_\pm(\boldsymbol{R},\boldsymbol{p})\equiv\sum_{\beta,\gamma=1,2}\bar{\xi}^\beta_\pm\boldsymbol{\sigma}^{\beta\gamma}\xi^\gamma_\pm=\pm\boldsymbol{m}(\boldsymbol{R},\boldsymbol{p}), \tag{4.7}$$

where we have introduced dimensionless spinors $\xi^\alpha=\xi^\alpha(\boldsymbol{R},\boldsymbol{p})$, and the bar denotes the complex conjugate. Hence, the lowest-order Green's function is

$$\tilde{G}^{\beta\gamma}_0(\omega;\boldsymbol{R},\boldsymbol{p})=\sum_{\sigma=\pm}\frac{\xi^\beta_\sigma\bar{\xi}^\gamma_\sigma}{E_\sigma/\hbar}=\tilde{G}^{\beta\gamma}_{0+}(\omega;\boldsymbol{R},\boldsymbol{p})+\tilde{G}^{\beta\gamma}_{0-}(\omega;\boldsymbol{R},\boldsymbol{p}), \tag{4.8}$$

where we have introduced the energy denominators

$$E_\pm=\hbar\omega-[\varepsilon_{\boldsymbol{p}}\pm\Delta]. \tag{4.9}$$

The first correction to the Green's function due to a gradient of the effective magnetic field can be found from the equation

$$\tilde{K}\tilde{G}_1+\frac{i}{2}(\overleftarrow{\boldsymbol{\nabla}}_R\cdot\vec{\boldsymbol{\nabla}}_p-\overleftarrow{\boldsymbol{\nabla}}_p\cdot\vec{\boldsymbol{\nabla}}_R)\tilde{K}\tilde{G}_0=0. \tag{4.10}$$

Its solution can be written in a more compact form by introducing the following notation:

$$S^i_{ab}=\bar{\xi}^\alpha_a(\sigma^i)^{\alpha\beta}\xi^\beta_b, \tag{4.11}$$

where $i=x,y,z$ labels the components of the vector of matrices $\boldsymbol{S}_{ab}$. Furthermore, it can be shown that

$$\varepsilon^{ijk}S^i_{+-}S^j_{-+}=i(m^k_+-m^k_-)=2im^k, \tag{4.12}$$

where ε^{ijk} is the Levi-Civita tensor. Using these definitions, we find that

$$\begin{aligned}\tilde{G}_1^{\alpha\beta}/\hbar =&(\tilde{G}_{0-}^{\alpha\beta} - \tilde{G}_{0+}^{\alpha\beta})\frac{\Delta^2}{E_+E_-}\varepsilon^{abc}(\boldsymbol{\nabla}_R m^a)\cdot(\boldsymbol{\nabla}_p m^b)m^c \\ &+(\boldsymbol{\nabla}_p\varepsilon_p)\cdot(\boldsymbol{\nabla}_R\Delta m^a)\frac{i\Delta}{(E_-E_+)^2}\left[\xi_-^\alpha\bar{\xi}_+^\beta S_{-+}^a - \xi_+^\alpha\bar{\xi}_-^\beta S_{+-}^a\right] \\ &+(\boldsymbol{\nabla}_R m_a\cdot\boldsymbol{\nabla}_p\Delta - \boldsymbol{\nabla}_p m_a\cdot\boldsymbol{\nabla}_R\Delta) \\ &\times\frac{i\Delta(\hbar\omega-\varepsilon_p)}{(E_-E_+)^2}\left[\xi_-^\alpha\bar{\xi}_+^\beta S_{-+}^a - \xi_+^\alpha\bar{\xi}_-^\beta S_{+-}^a\right].\end{aligned} \tag{4.13}$$

Note that only the first term on the right-hand side has a non-zero trace over the spin labels. The change in particle density due to a correction to the Green's function is determined by [125]

$$\Delta n = -\frac{1}{\beta}\sum_{\omega_n}\int\frac{d^3\boldsymbol{p}}{(2\pi\hbar)^3}\,\mathrm{Tr}[\tilde{G}_1], \tag{4.14}$$

where the the sum runs over the bosonic Matsubara frequencies and the integration is performed over the momenta $\boldsymbol{p}$. Note that for a fermionic system, the minus sign in the preceding formula is replaced by a plus sign [125]. Performing the trace and the Matsubara sum yields

$$\begin{aligned}\Delta n = \frac{1}{2}\int\frac{d^3\boldsymbol{p}}{(2\pi\hbar)^3}\varepsilon^{abc}(\boldsymbol{\nabla}_R m^a)\cdot(\boldsymbol{\nabla}_p m^b)m^c\Big[&(n_B(\varepsilon_-) - n_B(\varepsilon_+)) \\ &+\Delta(n_B'(\varepsilon_-) + n_B'(\varepsilon_+))\Big],\end{aligned} \tag{4.15}$$

where $n_B(z) = (e^{\beta(z-\mu)}-1)^{-1}$ is the Bose-Einstein distribution function, the prime indicates a derivative with respect to energy, $\varepsilon_\pm = \varepsilon_{\boldsymbol{p}} \pm \Delta$ are the energy levels of the two spin states, and μ is the chemical potential. Using the common definition for the phase-space Berry curvature

$$\Omega_{Rp}^{ij} = \varepsilon^{abc}(\nabla_R^i m^a)(\nabla_p^j m^b)m^c, \tag{4.16}$$

and introducing the following notation for the remainder of the integrand,

$$F = \frac{n_B(\varepsilon_-) - n_B(\varepsilon_+) + \Delta[n_B'(\varepsilon_-) + n_B'(\varepsilon_+)]}{2}, \tag{4.17}$$

we can write the change of density in a short form as

$$\Delta n = \sum_{i=x,y,z}\int\frac{d^3\boldsymbol{p}}{(2\pi\hbar)^3}\Omega_{Rp}^{ii}F. \tag{4.18}$$

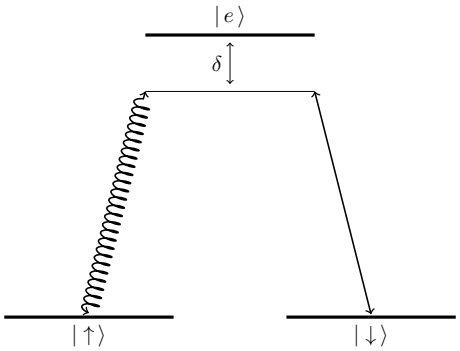

FIGURE 15: The Λ laser coupling scheme [31]. Two low-lying states $|\uparrow\rangle$ and $|\downarrow\rangle$ are coupled to an excited state $|e\rangle$ using a conventional laser (thick line with arrows) and a Laguerre-Gauss laser (coiled line with arrows) with the same detuning δ.

4.3 MODEL

In an effort of making a connection with experiments, we consider a concrete laser configuration and calculate the Berry curvature resulting from it. In particular, we consider a system of two laser beams (c.f. Fig. 15). The first one is propagating in the $y+z$ direction. It is described by the Rabi frequency

$$\omega_1 = |\omega_1| e^{ik(y+z)}, \tag{4.19}$$

where $k = 2\pi/\lambda$ is the wavenumber corresponding to the wavelength λ and $|\omega_1|$ is determined by the intensity of the first laser. The second laser beam propagates in the z direction and has the same wavelength. Each of the two lasers couple a pair of low-lying states with the same energy ($|\uparrow\rangle$ and $|\downarrow\rangle$) to an excited state ($|e\rangle$), where the low-lying states differ from the excited state by the principle quantum number (see Refs. [31, 119] for more details). However, the second laser has a Laguerre-Gauss beam profile. Hence, each of its photons carries an orbital angular momentum of $\hbar l$, and it is therefore characterized by

$$\omega_2 = |\omega_2| e^{ikz} e^{il\phi}, \tag{4.20}$$

where we have introduced the polar coordinates r and ϕ in the $x-y$ plane, and we choose $l = -1$. We will use both the polar coordinates (r, ϕ) and the Cartesian coordinates (x, y) to describe the same $x-y$ plane for brevity in what follows. The intensity of the second laser, $|\omega_2|$, vanishes in the center of the $x-y$ plane, where the phase is undetermined. Hence, in the simplest case $|\omega_2| = r \times \text{const}$. Furthermore, we have assumed that the cloud is localized enough in the z direction, such that we do not have to account for the spiral structure of the Laguerre-Gauss beam along its propagation axis. The laser detuning $\delta = \omega_L - \omega_A$ is defined as the difference between the laser-light

frequency ω_L (assumed identical for the two lasers) and the frequency of the atomic transition ω_A. When both lasers are detuned sufficiently far from the electronic transition $|\uparrow\rangle, |\downarrow\rangle \rightarrow |e\rangle$, the occupation of the excited level $|e\rangle$ is negligible. In that case, the excited level $|e\rangle$ can be integrated out in a straightforward manner, in the rotating-wave approximation, as its Green's function is equal to the inverse detuning frequency. Hence, we are left with an effective magnetic field

$$\Delta \boldsymbol{m} = \left(A_1 A_2 \cos[ky+\phi], A_1 A_2 \sin[ky+\phi], [A_1^2 - A_2^2]/2\right) \tag{4.21}$$

for the remaining ($|\uparrow\rangle$, $|\downarrow\rangle$) particles, where

$$A_j^2 = \hbar|\omega_j|^2/\delta \tag{4.22}$$

are the coupling amplitudes of the two lasers in terms of laser intensities and the detuning. We now perform the spin-basis rotation (exactly as in the case of Ref. [119]) around the z axis with the angle ky and obtain

$$\Delta \boldsymbol{m} = \left(A_1 A_2 x/r, A_1 A_2 y/r, [A_1^2 - A_2^2]/2 - \hbar^2 k p_y/M\right). \tag{4.23}$$

Note that a momentum dependence of the effective magnetic field has emerged after this step. This is the renowned synthetic spin-orbit interaction term. Intuitively, this dependence arises since the momentum operator in the kinetic-energy term of the Hamiltonian does not commute with a spatially-dependent spin-rotation operator. The magnetic field in Eq. (4.23) results in a non-zero phase-space Berry curvature in the y direction,

$$\Omega_{Rp}^{yy} = \frac{A_1^2 A_2^2 x}{r^2 \Delta^3} \frac{\hbar^2 k}{M}, \tag{4.24}$$

where the magnitude of the effective magnetic field is

$$\Delta^2 = \left(\hbar^2 k p_y/M + [A_2^2 - A_1^2]/2\right)^2 + A_1^2 A_2^2. \tag{4.25}$$

Note that introducing extra x or y dependence to A_i does not change the form of Ω_{Rk}^{yy}, as it enters the components of the effective magnetic field in a symmetric manner. We will use this property to consider beams with an intensity profile.

We are now in a position to describe a realistic system, where a cloud of atoms is confined to the $x-y$ plane with the trap frequency ω_z and trapped in a dipole trap with the frequency $\omega_\perp$ in that plane, in addition to being subject to the pair of spin-orbit-coupling lasers as described above but now with Gaussian intensity profiles,

$$\begin{aligned} A_1^2 &= a_1^2 e^{-(x-x_1)^2/R_1^2}, \\ A_2^2 &= a_2^2 e^{-r^2/R_2^2}, \end{aligned} \tag{4.26}$$

where the first laser beam has its intensity maximum at x_1, R_i are the radii, and a_i^2 are the peak intensity values of the two laser beams. The Hamiltonian of the atomic system is

$$H^{\alpha\beta} = (\varepsilon_{\boldsymbol{p}} + V)\delta^{\alpha\beta} + \Delta\boldsymbol{\sigma}^{\alpha\beta} \cdot \boldsymbol{m}, \tag{4.27}$$

where the trapping potential is $V = m(\omega_\perp^2 r^2 + \omega_z^2 z^2)/2$, and the effective magnetic field is given in Eq. (4.23). The total number of particles N at a certain chemical potential μ is given by the integral

$$N = \int d^3\boldsymbol{R} \int \frac{d^3\boldsymbol{k}}{(2\pi)^3} \left[n_B(\varepsilon_- + V) + n_B(\varepsilon_+ + V) \right]. \tag{4.28}$$

Since the gas is noninteracting, if the phase-space Berry-curvature effects are neglected, the condensation point is reached when the chemical potential in the center of the trap hits the lowest energy level from below, i.e., the critical chemical potential is $\mu_c = -\Delta$. The critical atom number N_c required for the condensation to occur is reached at this critical chemical potential.

The atom-number correction due to the phase-space Berry curvature at the Bose-Einstein transition point is

$$\Delta N_c = \int d^3\boldsymbol{R} \int \frac{d^3\boldsymbol{k}}{(2\pi)^3} \Omega_{Rp}^{yy} F, \tag{4.29}$$

where due to the local-density approximation the substitution $\varepsilon_i \to \varepsilon_i + V(r)$ is made in F, and F is evaluated at the critical chemical potential μ_c. The influence of the phase-space Berry curvature on the Bose-Einstein condensation transition is quantified by calculating the ratio

$$\rho = \frac{\Delta N_c}{N_c + \Delta N_c}. \tag{4.30}$$

4.4 DISCUSSION

We have carried out a numerical maximization of ρ, varying the relevant physical parameters (trap frequency, laser beam radii, laser intensities, laser wavelength, and atomic mass) in order to find the magnitude of the effect. We have discovered that ρ is always lower than 10^{-6}. Furthermore, in a three-dimensional harmonically trapped Bose gas a change of the critical number of atoms is related to the change of the condensation temperature [8],

$$\frac{\Delta T_c}{T_c} = \frac{1}{3}\frac{\Delta N_c}{N_c}, \tag{4.31}$$

where T_c is the condensation temperature without the Berry curvature, and hence the condensation temperature changes by approximately $10^{-6}T_c$, too.

Therefore, the effect of the phase-space Berry curvature on the critical atom number (or, equivalently, the condensation temperature) is very weak in the

regime of small magnetic-field grandients where the gradient expansion is applicable. Since the present experimental temperature resolution is on the order of $10^{-3}T_c$ [127], observing the predicted change is extremely challenging. Investigating effects of the phase-space Berry curvature on physical quantities that depend on the density of states stronger, however, might yield more promising results. Furthermore, going away from the regime where the gradient expansion is applicable and exploring strong spin-orbit coupling (for instance, using non-optical means [128, 129]) with large magnetic field gradients may lead to much greater effects. Both these directions are left for future research.

5

QUANTUM ROTOR MODEL FOR A BOSE-EINSTEIN CONDENSATE OF DIPOLAR MOLECULES

We show that a Bose-Einstein condensate of heteronuclear molecules in the regime of small and static electric fields is described by a quantum rotor model for the macroscopic electric dipole moment of the molecular gas cloud[1]. We solve this model exactly and find the symmetric, i.e., rotationally invariant, and dipolar phases expected from the single-molecule problem, but also an axial and planar nematic phase due to many-body effects. Investigation of the wavefunction of the macroscopic dipole moment also reveals squeezing of the probability distribution for the angular momentum of the molecules.

5.1 INTRODUCTION

A promising new direction in the field of ultracold quantum gases is the study of dipolar gases with heteronuclear molecules [130, 131, 132]. Recent progress in this direction has already contributed to such diverse research areas as atomic and molecular physics, quantum computation, and chemistry [133, 134, 135]. Indeed, the unique combination of strongly anisotropic long-range interactions and the quantum nature in these systems has brought to light a number of striking phenomena, such as tunneling-driven [22] and direction-dependent [23] ultracold chemical reactions, as well as the shape-dependent stability of the gas cloud [136].

The novel ingredient of heteronuclear molecules as compared to neutral atoms is their large permanent electric dipole moment, which opens the possibility for a strong dipole-dipole interaction. Neutral atoms typically do have a permanent magnetic dipole moment, but this leads to a dipole-dipole interaction that is much weaker than in the case of heteronuclear molecules, although it nevertheless has observable effects in certain cases [137, 138], in particular when the scattering length is made small using a Feshbach resonance [139, 140, 141]. In the absence of an external electric field, however, the average dipole moment in the laboratory frame is zero, since the rotational ground state of the molecule is spherically symmetric and the dipole moment is thus randomly oriented. For that reason, virtually all theoretical many-body studies are carried out in the limit of a large DC electric field. In that limit the molecules are completely polarized and the dipole moment in the laboratory frame is maximal [142]. One notable deviation from the large

1 This chapter is directly based on J. Armaitis, R. A. Duine, and H. T. C. Stoof, *Quantum Rotor Model for a Bose-Einstein Condensate of Dipolar Molecules*, Phys. Rev. Lett. 111, 215301 (2013).

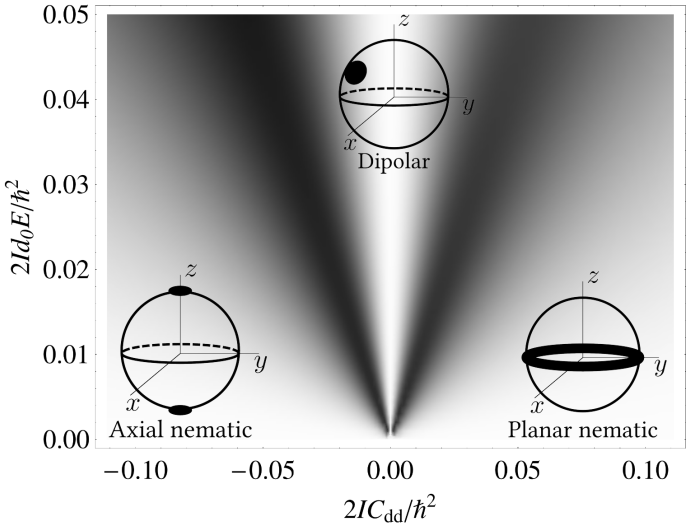

FIGURE 16: Phase diagram of the axially symmetric Bose-Einstein condensate of heteronuclear molecules, where the probability distributions for the dipole moment on the unit sphere in the non-trivial phases are schematically indicated by the black areas on the spheres. The vertical axis is the external electric field, while the horizontal axis is the dipole-dipole interaction strength. In this diagram, the fully symmetric phase exists only in the origin. Shading corresponds to the "squeezing" parameter σ in Eq. (5.9), which runs from zero (white) to 0.09 (gray). The electric field is at an $\pi/4$ angle to the symmetry axis of the cloud.

electric field limit is the discussion by Lin *et al.* [143], which considers the effects of an almost resonant AC electric field.

Going away from the large-field limit unmasks the subtle interplay between the quantum-mechanical rotation of the molecules, the long-range dipole-dipole interaction and the directing static electric field, which is the main topic of this chapter. In particular, the molecular Bose-Einstein condensate turns out to be a ferroelectric material that is fully disordered by quantum fluctuations in the absence of an electric field. This is illustrated by the phase diagram of a Bose-Einstein condensate of heteronuclear molecules in a harmonic uniaxial trap, that is shown in Fig. 16. The system possesses four phases: two nematic phases (a planar nematic and an axial nematic phase), a dipolar phase, and a fully symmetric phase, that are separated by smooth crossovers. Two order parameters are relevant for this system. Firstly, a non-zero average dipole moment $\langle d_i \rangle$ defines the dipolar phase. Secondly, in the absence of an average dipole moment the nematic (or quadrupole) tensor $Q_{ij} = \langle d_i d_j - \delta_{ij} \boldsymbol{d}^2/3 \rangle$ distinguishes the other three phases. In particular, the nematic tensor is equal to zero in the spherically symmetric phase. Two eigenvalues are positive and one is negative in the planar nematic phase, whereas

one eigenvalue is positive and two are negative in the axial nematic phase. It is worthwhile to notice that even in the absence of any electric field, many-body effects are crucial, giving rise to nematic ground states in strong contrast to the dipolar and fully symmetric ground states, expected from the single-molecule case. We finally remark that the predicted phase diagram is experimentally accessible by tuning three parameters in the laboratory, namely, the electric-field strength, the trap aspect ratio, and the number of particles.

5.2 MODEL

We start from the single-molecule Hamiltonian

$$H_{\mathrm{m}} = \frac{\boldsymbol{p}^2}{2m} + \frac{\boldsymbol{L}^2}{2I} - d_0 \hat{\boldsymbol{d}} \cdot \boldsymbol{E}, \tag{5.1}$$

where m is the mass of the molecule, $\boldsymbol{p} = -i\hbar\,\partial/\partial\boldsymbol{x}$ is the center-of-mass momentum operator with $\boldsymbol{x}$ the center-of-mass position, I is the moment of inertia of the molecule, $d_0\hat{\boldsymbol{d}}$ is the electric dipole moment operator, $\boldsymbol{L} = -i\hbar\hat{\boldsymbol{d}} \times \partial/\partial\hat{\boldsymbol{d}}$ is the angular momentum operator, associated with the rotation of the molecules, and $\boldsymbol{E}$ is the electric field. To describe the interactions between the molecules, we have to include both a contact (or s-wave) interaction term [8]

$$V_{\mathrm{s}} = \frac{4\pi\hbar^2 a}{m}\delta(\boldsymbol{r}), \tag{5.2}$$

and a dipole-dipole interaction term

$$V_{\mathrm{dd}} = -\frac{d_0^2}{4\pi\varepsilon_0 r^3}\left(3\,\hat{\boldsymbol{d}}_1 \cdot \hat{\boldsymbol{r}}\,\hat{\boldsymbol{d}}_2 \cdot \hat{\boldsymbol{r}} - \hat{\boldsymbol{d}}_1 \cdot \hat{\boldsymbol{d}}_2\right), \tag{5.3}$$

where δ is the Dirac delta function, a is the s-wave scattering length, ε_0 is the electric permittivity of vacuum, $d_0\hat{\boldsymbol{d}}_1$ and $d_0\hat{\boldsymbol{d}}_2$ are the dipole moments of the two interacting particles, $\boldsymbol{r}$ is the vector connecting them and r is the distance between the particles. Finally, we consider the molecular gas to be trapped in a harmonic axially-symmetric trapping potential

$$V_{\mathrm{trap}} = m\left[\omega_\perp^2(x^2+y^2) + \omega_z^2 z^2\right]/2, \tag{5.4}$$

where $\omega_\perp$ and ω_z are the radial and axial trapping frequencies, respectively.

For small electric fields, we are allowed to first solve for the spatial part of the condensate wavefunction by only including the effect of the s-wave interaction between the molecules. This leads to a Thomas-Fermi profile that depends on the s-wave scattering length [144]. The many-body ground state wavefunction is now $\Psi(\boldsymbol{r}_1, \boldsymbol{r}_2, \ldots, \boldsymbol{r}_N; \hat{\boldsymbol{d}}_1, \hat{\boldsymbol{d}}_2, \ldots, \hat{\boldsymbol{d}}_N) = \Pi_{i=1}^{N}\psi_{\mathrm{TF}}(\boldsymbol{r}_i) \times \psi(\hat{\boldsymbol{d}})$,

where N is the total number of molecules, and $\hat{\boldsymbol{d}}$ is the direction of $\boldsymbol{d} = (\sum_{i=1}^{N} \boldsymbol{d}_i)/N$. Hence, the dipole-dipole energy per particle is

$$V_{\mathrm{dd}}^{\mathrm{TF}} = -\frac{N d_0^2}{4\pi\varepsilon_0} \int \mathrm{d}\boldsymbol{r} P(\boldsymbol{r}) \frac{1}{r^5} \left(3\,(\hat{\boldsymbol{d}} \cdot \boldsymbol{r})^2 - \hat{\boldsymbol{d}}^2 r^2 \right), \tag{5.5}$$

where P is the probability to find two particles a certain distance apart. Subsequently, the many-body Hamiltonian per molecule in this so-called single-mode approximation [145] reduces to (c.f. the appendix)

$$H = \frac{\boldsymbol{L}^2}{2I} - d_0 \hat{\boldsymbol{d}} \cdot \boldsymbol{E} + C_{\mathrm{dd}} (3\hat{d}_z^2 - \hat{\boldsymbol{d}}^2), \tag{5.6}$$

where C_{dd} is the effective dipolar interaction strength

$$C_{\mathrm{dd}} = \frac{d_0^2 N}{4\varepsilon_0} \int \mathrm{d}z \rho\, \mathrm{d}\rho P(R) \frac{1}{r^3} \left(\frac{3}{2} \frac{\rho^2}{r^2} - 1 \right), \tag{5.7}$$

and we have introduced the radius in cylindrical coordinates $r^2 = \rho^2 + z^2$, the dimensionless radius $R^2 = (\rho/x_{\mathrm{TF}})^2 + (z/z_{\mathrm{TF}})^2$, the radial size of the cloud x_{TF}, the axial size $z_{\mathrm{TF}} = \lambda x_{\mathrm{TF}}$, and the aspect ratio $\lambda = \omega_\perp/\omega_z$. We emphasize that even though Eq. (5.6) describes the dipole degree of freedom of the three-dimensional many-body system, it actually has a form of a single-particle (and thus effectively zero-dimensional) Hamiltonian, and the whole Bose-Einstein condensate acts as a single quantum rotor.

In the Thomas-Fermi approximation the probability P can be calculated analytically: $P(R) = 15(R-2)^4 \left(32 + 64R + 24R^2 + 3R^3\right)/7168\pi\lambda x_{\mathrm{TF}}^3$ for $R < 2$ and zero otherwise. The analytic expression for $P(R)$ yields [146, 147]

$$\begin{aligned} C_{\mathrm{dd}} = &-5N d_0^2 / \left(56\pi\varepsilon_0 x_{\mathrm{TF}}^3 \lambda \left(\lambda^2 - 1\right)^2 \right) \\ &\times \left(\lambda^4 + \lambda^2 - 2 + 3\lambda\sqrt{1-\lambda^2}\,\mathrm{ArcCot}\left[\frac{\lambda}{\sqrt{1-\lambda^2}} \right] \right), \end{aligned} \tag{5.8}$$

which corresponds to one half of the mean-field dipolar energy per particle in the case of fully polarized electric dipoles ([146, 147]). Analogous results for magnetic dipoles were obtained by other authors for spinor Bose-Einstein condensates in the Gaussian approximation [148, 149]. Note that C_{dd} depends on the number of particles N and the trap aspect ratio λ. Thus, the only effect of varying the number of particles is the change in C_{dd}.

The Hamiltonian in Eq. (5.6) represents a quantum rotor model for the macroscopic dipole moment of the molecular Bose-Einstein condensate, whose derivation is the main result of this chapter. Interestingly, a similar Hamiltonian applies to an atomic ferromagnetic spinor Bose-Einstein condensate (c.f. Ref. [150] for a quantum rotor model of antiferromagnetic spinor condensates), but then without the quantum rotor term [148]. The reason for this difference is that the total (spin) angular momentum of the atoms is fixed,

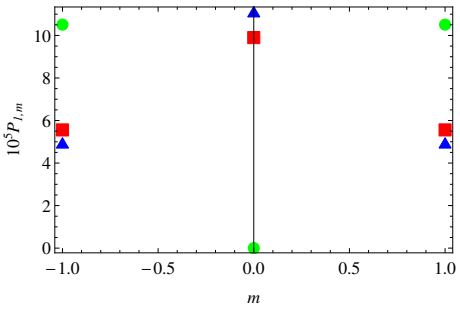

FIGURE 17: Probability $P_{1,m}$ of occupying a state with total angular momentum 1 and its projection m. We have chosen $C_{\mathrm{dd}} = 0.1\hbar^2/2I$ and $E = 0.05\hbar^2/2Id_0$ ($\boldsymbol{E}$ is at $\pi/4$ angle to the z axis) in order to maximize the anisotropy of the state. The red squares correspond to the x' direction, the green circles correspond to the y' direction, and the blue triangles correspond to the z' direction, where the axes are defined such that the $\langle \hat{d}_i \hat{d}_j \rangle$ matrix is diagonal and has its smallest eigenvalue in the z' direction.

whereas in the case of interest here the wavefunction of the molecules is in general a superposition of states with an arbitrary (rotational) angular momentum, whose energy splitting is determined by the finite moment of inertia. Next we are going to investigate the ground-state properties of this quantum rotor model.

5.3 RESULTS

We have obtained the exact phase diagram pertaining to this Hamiltonian by expanding the dipolar wavefunction in spherical harmonics (Fig. 16). For zero electric field and no dipole-dipole interaction, the ground state of the system is a trivial spherically symmetric (non-dipolar) state. However, turning on $\boldsymbol{E}$ or C_{dd} results in a very different state. For zero C_{dd} and non-zero $\boldsymbol{E}$, we obtain a dipolar state, where the probability distribution on the sphere is concentrated around the direction of the electric field. This state is classical in the sense that it is analogous to a classical dipole in the electric field. Another limiting case is $\boldsymbol{E} = \boldsymbol{0}$ and $C_{\mathrm{dd}} < 0$, where we have an axial nematic phase, and the probability is concentrated around the north and south poles of the sphere. Finally, we have a planar nematic phase for $\boldsymbol{E} = \boldsymbol{0}$, $C_{\mathrm{dd}} > 0$, where the high probability region is located around the equator of the sphere. The last two phases are quantum mechanical, as the ground state there is a coherent superposition of spherical harmonics with no average dipole moment. We observe smooth crossovers between the non-trivial phases, as expected due to the existence of quantum fluctuations in this effectively zero-dimensional situation.

In addition to the coordinate-space probability distribution $|\psi(\hat{\boldsymbol{d}})|^2$, we investigate the probability distribution with respect to angular momentum P_l. To that end, we expand our wavefunction in terms of spherical harmonics: $\psi(\hat{\boldsymbol{d}}) = \sum_{l,m} \alpha_{l,m} Y_{l,m}(\hat{\boldsymbol{d}})$. Hence, $P_l = \sum_{m=-l}^{l} P_{l,m}$, where $P_{l,m} = |\alpha_{l,m}|^2$ is the probability to occupy a state which has angular momentum quantum number l and azimuthal quantum number m. We find that this distribution has a peak at $l = 0$ for negative C_{dd}, and is peaked at $l \geq 0$ for positive C_{dd} or non-zero $\boldsymbol{E}$. For larger values of C_{dd} and $|E|$, the peak shifts towards larger values of l. Moreover, due to the nature of the dipole-dipole interaction that conserves parity, at zero electric field P_l is zero for odd l. We have also investigated the distribution of probability between different $|l, m\rangle$ states (Fig. 17). In general, this distribution is symmetric ($P_{l,m} = P_{l,-m}$) in every direction, implying that the average angular momentum $\langle \boldsymbol{L} \rangle$ is always zero, which is a consequence of time-reversal symmetry.

Noticing an anisotropic distribution of average dipole moment probability on the sphere in our system for certain parameters, it is natural to draw a parallel with the effect of spin squeezing [151]. To that end, we define a matrix $\langle L_i L_j \rangle$. This matrix describes the (Heisenberg) uncertainty in the angular momentum of the system. It has three eigenvalues, that we order as follows: $|\lambda_0| \leq |\lambda_-| \leq |\lambda_+|$. Hence, we define a measure of angular momentum "squeezing" as

$$\sigma = \frac{|\lambda_+| - |\lambda_-|}{|\lambda_+| + |\lambda_-|}, \tag{5.9}$$

which tells us how anisotropic the uncertainty of angular momentum is (c.f. Fig. 16). However, we must point out that, strictly speaking, this effect is not identical to squeezing in the usual sense, because $\langle L_i \rangle = 0$ and $P_{l,m}$ is not always a monotonically decreasing function of m (as can be seen from Fig. 17).

5.4 DISCUSSION AND CONCLUSION

It is interesting to compare the exact results described so far with mean-field theory techniques commonly employed for atomic Bose-Einstein condensates. Thus we turn to the Hartree approximation (which is equivalent to solving the Gross-Pitaevskii equation) for an analysis of the Hamiltonian in Eq. (5.6). To that end, we replace the operator $\hat{d}_i^2$ by $\hat{d}_i \langle \hat{d}_i \rangle$. The effect of the dipole-dipole interaction is then an additional static electric field of the form

$$\boldsymbol{E}_{\mathrm{dd}} = \frac{C_{\mathrm{dd}}}{d_0} (\langle \hat{d}_x \rangle, \langle \hat{d}_y \rangle, -2\langle \hat{d}_z \rangle)^T, \tag{5.10}$$

where the angle brackets indicate a quantum-mechanical average, and $N\langle \boldsymbol{d} \rangle \cdot \boldsymbol{E}_{\mathrm{dd}}$ is the total average (Hartree) energy of all the classical dipoles with a

density distribution given by the Thomas-Fermi profile. Therefore, we now have to solve the effective single-particle Hamiltonian

$$H_{\mathrm{MF}} = \frac{\boldsymbol{L}^2}{2I} - d_0 \hat{\boldsymbol{d}} \cdot \boldsymbol{E}_{\mathrm{eff}}, \tag{5.11}$$

where $\boldsymbol{E}_{\mathrm{eff}} = \boldsymbol{E} + \boldsymbol{E}_{\mathrm{dd}}$ is the effective electric field, which now depends on the cloud geometry and the average dipole moment.

The average dipole moment in this approach is determined in two steps. First, we calculate the average dipole moment of the ground state $\langle \boldsymbol{d} \rangle(\boldsymbol{E})$ from Eq. (5.11) (see e.g. Ref. [133]). Second, we write down a self-consistency condition, accounting for the effective electric field:

$$\langle \boldsymbol{d} \rangle = \langle \boldsymbol{d} \rangle(\boldsymbol{E}_{\mathrm{eff}}(\langle \boldsymbol{d} \rangle)). \tag{5.12}$$

In the well-known case of a single molecule, C_{dd} is zero, Eq. (5.12) has a single solution, and $\langle \boldsymbol{d} \rangle$ always points in the direction of $\boldsymbol{E}$. However, this is not the case for the whole $(C_{\mathrm{dd}}, \boldsymbol{E})$ space and therefore requires a more thorough analysis. For small non-zero $|C_{\mathrm{dd}}|$ and $\boldsymbol{E} = 0$, there still is only one solution, namely, $\langle \boldsymbol{d} \rangle = 0$. For $C_{\mathrm{dd}} < 0$ and $E_z \neq 0$, the average dipole moment is always non-zero (Eq. (5.12) has a single solution), as then we are dealing with an Ising-like (easy-axis) model, and E_z couples directly to the order parameter $\langle \boldsymbol{d} \rangle$. In contrast to this, three solutions exist for $E_z = 0$ and $C_{\mathrm{dd}}/|E_\perp|$ sufficiently large and negative. The two $\langle d_z \rangle \neq 0$ solutions are degenerate in energy, while the $\langle d_z \rangle = 0$ solution has a higher energy. On the other hand, for $C_{\mathrm{dd}} > 0$ we are dealing with an XY-like (easy-plane) model and thus in that case one obtains a similar non-trivial situation for $E_\perp = 0$ and $C_{\mathrm{dd}}/|E_z|$ large and positive.

When comparing the mean-field theory with the exact diagonalization of the Hamiltonian in Eq. (5.6), it is important to notice that the mean-field ansatz explicitly assumes that the average dipole moment is pointing in some direction. Therefore, the nematic phases are absent from the mean-field phase diagram. The fact that the dipole moment is zero under the asserted conditions can be intuitively understood, as the exact approach allows for a quantum superposition of states that have oppositely polarized dipole moments and are degenerate at the mean-field level. Finally, it is well known that the mean-field theory does not give reliable results in low dimensions because of the increased importance of quantum fluctuations. Since we are investigating an effectively zero-dimensional Hamiltonian, it is no surprise that the results of the mean-field theory differ significantly from the exact calculation.

In our analysis we have relied on the single-mode approximation, which is applicable to Bose-Einstein condensates with s-wave and dipole-dipole interactions [152]. However, we have not accounted for the dependence of the cloud aspect ratio $z_{\mathrm{TF}}/x_{\mathrm{TF}}$ on dipole-dipole interactions. This limits the ap-

plicability of our analysis to the regime, where the dipole-dipole interaction is much weaker than the mean-field s-wave interaction [148], i.e.,

$$|\langle \boldsymbol{d} \rangle|^2 m / 4\pi\hbar^2 \varepsilon_0 a \ll 1. \tag{5.13}$$

For a typical diatomic molecule with a mass of 80 atomic mass units, a scattering length of 5 Bohr radii and an electric dipole moment of 1 Debye, this limits the external electric field strength to $|\boldsymbol{E}| \ll 1\,\mathrm{kV/cm}$, which translates to $2Id_0E/\hbar^2 \ll 0.05$ in the units of Fig. 16. We have also estimated that for a cloud of 10^7 particles with a linear extent of around $1\mu m$, or radial trapping frequency of approximately $2\pi \times 80$ kHz, assuming a nearly two-dimensional trap with an aspect ratio of 1:10, $C_{\mathrm{dd}} \simeq 0.1 \times \hbar^2/2I$, which corresponds to the energy of $2\pi\hbar \times 1$ GHz.

Besides the single-mode approximation, we have also made an assumption that the s-wave scattering length is independent of the dipole moment. Even though it has been shown that such a dependence is present [153, 154, 155, 156], including it would merely add an extra self-consistency equation to our approach. Its effect would be to change the Thomas-Fermi radii and thus map the system to a different point in the phase diagram. Therefore, all our results remain qualitatively unaffected.

In summary, we have considered an interacting Bose-Einstein condensate of dipolar molecules in a small static electric field. We have solved this problem exactly in the single-mode approximation and have also compared this with the mean-field (Gross-Pitaevskii) approach. We have found that the two approaches to the problem yield qualitatively very different results. Finally, we have put forward an experimentally accessible phase diagram and investigated the exact ground-state wavefunction both in coordinate and angular-momentum space.

5.5 APPENDIX

5.5.1 *Single-mode approximation Hamiltonian*

In this section we provide a more detailed derivation of the SMA Hamiltonian [148] than the one given in the chapter. We start from a many-body Hamiltonian with interactions

$$\begin{aligned} H_{\mathrm{mb}} = &\sum_{i=1}^{N} \left(\frac{\boldsymbol{p}_i^2}{2m} + \frac{\boldsymbol{L}_i^2}{2I} - d_0 \hat{\boldsymbol{d}}_i \cdot \boldsymbol{E} + V_{\mathrm{trap}}(\boldsymbol{r}_i) \right) \\ &+ \sum_{i<j} \left(V_s(\boldsymbol{r}_i - \boldsymbol{r}_j) + V_{dd}(\hat{\boldsymbol{d}}_i, \hat{\boldsymbol{d}}_j, \boldsymbol{r}_i - \boldsymbol{r}_j) \right), \end{aligned} \tag{5.14}$$

where the s-wave interaction is

$$V_s(\boldsymbol{r}) = \frac{4\pi\hbar^2 a}{m} \delta(\boldsymbol{r}), \tag{5.15}$$

the trapping potential is

$$V_{\text{trap}}(\boldsymbol{r}) = m\left[\omega_\perp^2(x^2+y^2)+\omega_z^2 z^2\right]/2, \tag{5.16}$$

and where $\boldsymbol{r}_i$ is the center-of-mass position of molecule i, $d_0\hat{\boldsymbol{d}}_i$ is its electric dipole moment ($\hat{\boldsymbol{d}}_i$ is the direction of $\boldsymbol{d}_i$), and

$$\boldsymbol{L}_i = -i\hbar\hat{\boldsymbol{d}}_i \times \partial/\partial\hat{\boldsymbol{d}}_i \tag{5.17}$$

is its angular momentum. Moreover, the dipole-dipole interaction is

$$V_{dd}(\hat{\boldsymbol{d}}_i, \hat{\boldsymbol{d}}_j, \boldsymbol{r}) = -\frac{d_0^2}{4\pi\varepsilon_0 r^3}\left(3\,\hat{\boldsymbol{d}}_i\cdot\hat{\boldsymbol{r}}\,\hat{\boldsymbol{d}}_j\cdot\hat{\boldsymbol{r}} - \hat{\boldsymbol{d}}_i\cdot\hat{\boldsymbol{d}}_j\right), \tag{5.18}$$

where $r = |\boldsymbol{r}|$ and $\hat{\boldsymbol{r}} = \boldsymbol{r}/r$. We separate the Hamiltonian into two parts, the non-dipolar part

$$H_{\text{nd}} = \sum_{i=1}^{N}\left(\frac{\boldsymbol{p}_i^2}{2m} + V_{\text{trap}}(\boldsymbol{r}_i)\right) + \sum_{i<j} V_s(\boldsymbol{r}_i - \boldsymbol{r}_j) \tag{5.19}$$

and the dipolar part

$$H_{\text{d}} = \sum_{i=1}^{N}\left(\frac{\boldsymbol{L}_i^2}{2I} - d_0\hat{\boldsymbol{d}}_i\cdot\boldsymbol{E}\right) + \sum_{i<j} V_{dd}(\hat{\boldsymbol{d}}_i, \hat{\boldsymbol{d}}_j, \boldsymbol{r}_i - \boldsymbol{r}_j). \tag{5.20}$$

Since we consider a Bose-Einstein condensate such that all the bosons are in the same spatial single-particle state $\phi(\boldsymbol{r}_i)$, an accurate variational many-body wavefunction is

$$\Psi(\boldsymbol{r}_1, \boldsymbol{r}_2, \ldots, \boldsymbol{r}_N; \boldsymbol{d}_1, \boldsymbol{d}_2, \ldots, \boldsymbol{d}_N) = \psi_d(\boldsymbol{d}_1, \boldsymbol{d}_2, \ldots, \boldsymbol{d}_N)\prod_{i=1}^{N}\phi(\boldsymbol{r}_i), \tag{5.21}$$

where the single-particle wavefunction is normalized as

$$\int \mathrm{d}\boldsymbol{r}|\phi(\boldsymbol{r})|^2 = 1. \tag{5.22}$$

For small electric fields we can in first instance neglect the influence of the dipole-dipole interaction on the spatial wavefunction and $\phi(\boldsymbol{r})$ is determined by minimizing the non-dipolar part of the Hamiltonian. In that case, the energy including the Lagrange multiplier μ that enforces particle number N is given by

$$\begin{aligned}\langle H_{\text{nd}}\rangle - \mu N = N\int d\boldsymbol{r}\,\phi^*(\boldsymbol{r})\Big(&-\frac{\hbar^2\boldsymbol{\nabla}^2}{2m} + V_{\text{trap}}(\boldsymbol{r}) \\ &+ \frac{2(N-1)\pi\hbar^2 a}{m}|\phi(\boldsymbol{r})|^2 - \mu\Big)\phi(\boldsymbol{r}).\end{aligned} \tag{5.23}$$

Variation of $\langle H_{\rm nd}\rangle - \mu N$ with respect to $\phi^*(\boldsymbol{r})$ yields

$$\left(-\frac{\hbar^2\boldsymbol{\nabla}^2}{2m} + V_{\rm trap}(\boldsymbol{r}) + \frac{4\pi\hbar^2 a}{m}(N-1)|\phi(\boldsymbol{r})|^2 - \mu\right)\phi(\boldsymbol{r}) = 0. \tag{5.24}$$

For a large cloud ($N \gg 1$), the kinetic energy related to the spatial part of the many-body wavefunction is much smaller than the interaction energy or the trapping potential. Neglecting the kinetic energy is known as the Thomas-Fermi approximation [144], resulting in the wavefunction $\phi \equiv \psi_{\rm TF}$ with

$$|\psi_{\rm TF}(\boldsymbol{r})|^2 = n(\boldsymbol{r})/N = \frac{m}{4\pi\hbar^2 a}\frac{\mu - V_{\rm trap}(\boldsymbol{r})}{N}, \tag{5.25}$$

where $n(\boldsymbol{r})$ is the density of particles, and we have approximated $N-1 \simeq N$.

We continue by making a variational ansatz for the dipolar part of the wavefunction. To that end, we construct a superposition of wavepackets of the form

$$\Psi(\boldsymbol{r}_1, \boldsymbol{r}_2, \ldots, \boldsymbol{r}_N; \hat{\boldsymbol{d}}_1, \hat{\boldsymbol{d}}_2, \ldots, \hat{\boldsymbol{d}}_N) = \int \mathrm{d}\hat{\boldsymbol{d}} \prod_{i=1}^{N}\left[\psi_{\rm TF}(\boldsymbol{r}_i)\zeta(\hat{\boldsymbol{d}}_i - \hat{\boldsymbol{d}})\right]\psi(\hat{\boldsymbol{d}}), \tag{5.26}$$

where the wavefunction ζ has the property that individual dipoles point in the $\hat{\boldsymbol{d}}$ direction on average:

$$\int \mathrm{d}\hat{\boldsymbol{d}}_i\, |\zeta(\hat{\boldsymbol{d}}_i - \hat{\boldsymbol{d}})|^2 \hat{\boldsymbol{d}}_i = \hat{\boldsymbol{d}}. \tag{5.27}$$

Moreover, we require ζ to be sharply localized around $\hat{\boldsymbol{d}}$. Note that Ψ is not a mean-field wavefunction, except for the case of the strong electric field, where $\psi(\hat{\boldsymbol{d}})$ approaches a delta function.

We now come back to the part of $H_{\rm mb}$ that describes the dipolar degree of freedom and consider its expectation value per particle

$$\begin{aligned}\frac{\langle H_{\rm d}\rangle}{N} = \int \prod_{i=1}^{N}\left[\mathrm{d}\boldsymbol{r}_i\, \mathrm{d}\hat{\boldsymbol{d}}_i\right] \Psi^*(\boldsymbol{r}_1, \boldsymbol{r}_2, \ldots, \boldsymbol{r}_N; \hat{\boldsymbol{d}}_1, \hat{\boldsymbol{d}}_2, \ldots, \hat{\boldsymbol{d}}_N) \\ \times H_{\rm d}\Psi(\boldsymbol{r}_1, \boldsymbol{r}_2, \ldots, \boldsymbol{r}_N; \hat{\boldsymbol{d}}_1, \hat{\boldsymbol{d}}_2, \ldots, \hat{\boldsymbol{d}}_N)\end{aligned} \tag{5.28}$$

in order to derive the Hamiltonian for the direction of the macroscopic dipole moment $\boldsymbol{d}$. In what follows, we consider this expectation value term by term. We start with the rotation energy for a molecule, i.e.,

$$\begin{aligned}&\int \prod_{i=1}^{N}\left[\mathrm{d}\boldsymbol{r}_i\, \mathrm{d}\hat{\boldsymbol{d}}_i\right] \Psi^* \frac{\boldsymbol{L}_j^2}{2I}\Psi = \frac{-\hbar^2}{2I}\int \prod_{i=1}^{N}\left[\mathrm{d}\boldsymbol{r}_i\, \mathrm{d}\hat{\boldsymbol{d}}_i\right] \Psi^* \left(\hat{\boldsymbol{d}}_j \times \frac{\partial}{\partial \hat{\boldsymbol{d}}_j}\right)^2 \Psi \\ &\simeq \frac{-\hbar^2}{2I}\int \mathrm{d}\hat{\boldsymbol{d}}\, \mathrm{d}\hat{\boldsymbol{d}}'\, \psi^*(\hat{\boldsymbol{d}}')\left(\hat{\boldsymbol{d}} \times \frac{\partial}{\partial \hat{\boldsymbol{d}}}\right)^2 \delta(\hat{\boldsymbol{d}} - \hat{\boldsymbol{d}}')\,\psi(\hat{\boldsymbol{d}}) \\ &= \int \mathrm{d}\hat{\boldsymbol{d}}\, \psi^*(\hat{\boldsymbol{d}})\frac{\boldsymbol{L}^2}{2I}\psi(\hat{\boldsymbol{d}}),\end{aligned} \tag{5.29}$$

where $\boldsymbol{L}$ is the angular momentum operator for the average direction $\hat{\boldsymbol{d}}$ and we have used the localization property

$$\prod_{i=1}^{N}\left(\int \mathrm{d}\hat{\boldsymbol{d}}_i\,\zeta^*(\hat{\boldsymbol{d}}_i-\hat{\boldsymbol{d}}')\zeta(\hat{\boldsymbol{d}}_i-\hat{\boldsymbol{d}})\right)\simeq\delta(\hat{\boldsymbol{d}}-\hat{\boldsymbol{d}}'). \tag{5.30}$$

Since the electric field term follows from Eq. (5.27) in a straightforward manner, we are left with the dipole-dipole interaction term. Similarly to the wavefunction, it can be written as a product of the spatial part and the dipolar part:

$$V_{dd}(\hat{\boldsymbol{d}}_i,\hat{\boldsymbol{d}}_j,\boldsymbol{r}_i-\boldsymbol{r}_j)=\hat{\boldsymbol{d}}_i^{\alpha}A^{\alpha\beta}(\boldsymbol{r}_i-\boldsymbol{r}_j)\hat{\boldsymbol{d}}_j^{\beta}, \tag{5.31}$$

where α and β are the spatial indices and a sum over them is implied. We now rewrite the dipole-dipole interaction expectation value making the average dipole direction dependence explicit and having in mind that $i\neq j$:

$$\begin{aligned}
&\int\prod_{k=1}^{N}\left[\mathrm{d}\boldsymbol{r}_k\;\mathrm{d}\hat{\boldsymbol{d}}_k\right]\;\mathrm{d}\hat{\boldsymbol{d}}\,\mathrm{d}\hat{\boldsymbol{d}}'\,\Psi^*V_{dd}(\hat{\boldsymbol{d}}_i,\hat{\boldsymbol{d}}_j,\boldsymbol{r}_i-\boldsymbol{r}_j)\Psi\\
&=\frac{1}{N^2}\int\mathrm{d}\boldsymbol{r}_i\,\mathrm{d}\boldsymbol{r}_j n(\boldsymbol{r}_i)n(\boldsymbol{r}_j)A^{\alpha\beta}(\boldsymbol{r}_i-\boldsymbol{r}_j)\\
&\quad\times\int\mathrm{d}\hat{\boldsymbol{d}}\,\mathrm{d}\hat{\boldsymbol{d}}'\prod_{k=1}^{N}\left[\mathrm{d}\hat{\boldsymbol{d}}_k\zeta^*(\hat{\boldsymbol{d}}_k-\hat{\boldsymbol{d}}')\zeta(\hat{\boldsymbol{d}}_k-\hat{\boldsymbol{d}})\right]\hat{\boldsymbol{d}}_i^{\alpha}\hat{\boldsymbol{d}}_j^{\beta}\psi^*(\hat{\boldsymbol{d}}')\psi(\hat{\boldsymbol{d}})\\
&=\frac{1}{N^2}\int\mathrm{d}\boldsymbol{r}_i\,\mathrm{d}\boldsymbol{r}_j n(\boldsymbol{r}_i)n(\boldsymbol{r}_j)A^{\alpha\beta}(\boldsymbol{r}_i-\boldsymbol{r}_j)\int\mathrm{d}\hat{\boldsymbol{d}}\,\hat{\boldsymbol{d}}^{\alpha}\hat{\boldsymbol{d}}^{\beta}|\psi(\hat{\boldsymbol{d}})|^2,
\end{aligned} \tag{5.32}$$

where we have used the localization property again. Using the definition of the probability to find two particles a distance $\boldsymbol{r}$ apart

$$P(\boldsymbol{r})=\frac{1}{N^2}\int\mathrm{d}\boldsymbol{x}\,n(\boldsymbol{x})n(\boldsymbol{x}+\boldsymbol{r}) \tag{5.33}$$

and performing a sum over pairs of particles yields the following dipole-dipole interaction energy per particle:

$$V_{\mathrm{dd}}^{\mathrm{TF}}=-\frac{(N-1)d_0^2}{4\pi\varepsilon_0}\int\mathrm{d}\boldsymbol{r}P(\boldsymbol{r})\frac{1}{r^5}\left(3\,(\hat{\boldsymbol{d}}\cdot\boldsymbol{r})^2-\hat{\boldsymbol{d}}^2r^2\right). \tag{5.34}$$

Since $P(-\boldsymbol{r})=P(\boldsymbol{r})$, we rewrite the last expression as

$$V_{\mathrm{dd}}^{\mathrm{TF}}=-\frac{(N-1)d_0^2}{4\pi\varepsilon_0}\int\mathrm{d}\boldsymbol{r}P(\boldsymbol{r})\frac{1}{r^5}\hat{\boldsymbol{d}}^{\alpha}\left(3\boldsymbol{r}^{\alpha}\boldsymbol{r}^{\beta}-r^2\delta^{\alpha\beta}\right)\hat{\boldsymbol{d}}^{\beta}. \tag{5.35}$$

We find that only the diagonal terms survive the integration and after going to cylindrical coordinates we find that

$$\int\mathrm{d}\boldsymbol{r}P(\boldsymbol{r})\frac{1}{|r|^5}\left(3(r^x)^2-r^2\right)=2\pi\int\rho\,\mathrm{d}\rho\,\mathrm{d}zP(\rho,z)\frac{1}{r^3}\left[\frac{3}{2}\frac{\rho^2}{r^2}-1\right] \tag{5.36}$$

and

$$\int \mathrm{d}\boldsymbol{r} P(\boldsymbol{r}) \frac{1}{|r|^5} \left(3(r^z)^2 - r^2\right) = 2\pi \int \rho \, \mathrm{d}\rho \, \mathrm{d}z P(\rho, z) \frac{1}{r^3} \left[-3\frac{\rho^2}{r^2} + 2\right]. \quad (5.37)$$

Since $(\hat{\boldsymbol{d}}^x)^2 + (\hat{\boldsymbol{d}}^y)^2 - 2(\hat{\boldsymbol{d}}^z)^2 = (\hat{\boldsymbol{d}})^2 - 3(\hat{\boldsymbol{d}}^z)^2$, and by approximating $N - 1 \simeq N$ again we arrive at the final expression for the dipole-dipole interaction

$$V_{\mathrm{dd}}^{\mathrm{TF}} = -\frac{N d_0^2}{4\pi\varepsilon_0} \int \mathrm{d}\boldsymbol{r} P(\boldsymbol{r}) \frac{1}{r^5} \left(3\,(\hat{\boldsymbol{d}} \cdot \boldsymbol{r})^2 - \hat{\boldsymbol{d}}^2 r^2\right) = C_{\mathrm{dd}}(3\hat{d}_z^2 - \hat{\boldsymbol{d}}^2), \quad (5.38)$$

where C_{dd} is the effective dipolar interaction strength

$$C_{\mathrm{dd}} = \frac{d_0^2 N}{4\varepsilon_0} \int \mathrm{d}z \rho \, \mathrm{d}\rho P(R) \frac{1}{r^3} \left(\frac{3}{2}\frac{\rho^2}{r^2} - 1\right). \quad (5.39)$$

Hence, the expectation value of the dipolar part of the many-body Hamiltonian is

$$\frac{\langle H_{\mathrm{d}} \rangle}{N} = \int \mathrm{d}\hat{\boldsymbol{d}} \, \psi^*(\hat{\boldsymbol{d}}) \left(\frac{\boldsymbol{L}^2}{2I} - d_0 \hat{\boldsymbol{d}} \cdot \boldsymbol{E} + C_{\mathrm{dd}}(3\hat{d}_z^2 - \hat{\boldsymbol{d}}^2)\right) \psi(\hat{\boldsymbol{d}}). \quad (5.40)$$

Finally, we vary this expression with respect to $\psi^*(\hat{\boldsymbol{d}})$ and obtain the single-mode approximation Hamiltonian given in the chapter

$$H = \frac{\boldsymbol{L}^2}{2I} - d_0 \hat{\boldsymbol{d}} \cdot \boldsymbol{E} + C_{\mathrm{dd}}(3\hat{d}_z^2 - \hat{\boldsymbol{d}}^2), \quad (5.41)$$

where this last Hamiltonian is later used to determine the ground-state wavefunction $\psi(\hat{\boldsymbol{d}})$.

5.5.2 *Probability distribution*

We would like to point out that in order to draw any conclusions about the state of the system by comparing $P_{l,m}$ measurements, where $P_{l,m}$ is the probability to occupy a state with total angular momentum l and its projection m, it is important to diagonalize the $\langle \hat{d}_i \hat{d}_j \rangle$ matrix for each configuration of the electric field $\boldsymbol{E}$ and the dipolar interaction strength C_{dd}. To illustrate this point, we provide $P_{1,m}$ for two different situations: a "squeezed" state with both a finite electric field and a finite dipole-dipole interaction strength (Fig. 18 left) and a dipolar state, where the dipole-dipole interaction is zero (Fig. 18 center and right). The two situations give a qualitatively similar $P_{1,m}$ when viewed in the same coordinate system (Fig. 18 left and center). However, if one compares the probability distributions for the coordinate systems where $\langle \hat{d}_i \hat{d}_j \rangle$ is diagonal (Fig. 18 left and right), the difference is obvious.

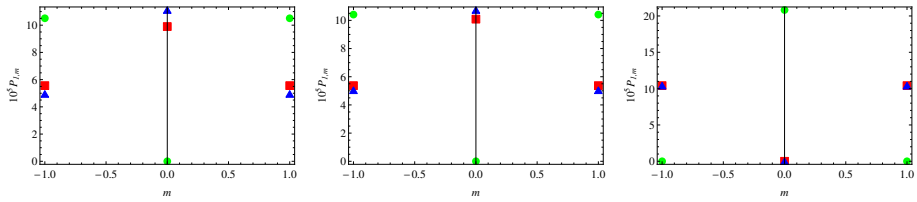

FIGURE 18: Probability $P_{1,m}$ of occupying a state with total angular momentum 1 and its projection m for the electric field $E = 0.05\hbar^2/2Id_0$ ($\boldsymbol{E}$ is at $\pi/4$ angle to the z axis). The left figure depicts a situation with a finite dipole-dipole interaction $C_{\mathrm{dd}} = 0.1\hbar^2/2I$, whereas the other figures are for the non-interacting ($C_{\mathrm{dd}} = 0$) case. The red squares correspond to the x' direction, the green circles correspond to the y' direction, and the blue triangles correspond to the z' direction. The axes are the same for the left and center figures, while they are different for the right figure. They are defined such that the $\langle \hat{d}_i \hat{d}_j \rangle$ matrix is diagonal and has its smallest eigenvalue in the z' direction for the $C_{\mathrm{dd}} = 0.1\hbar^2/2I$ case (left and center) or for $C_{\mathrm{dd}} = 0$ (right).

SUMMARY

This thesis explores certain theoretical aspects of experimentally accessible systems of ultracold gases. Since the topics presented in this thesis are rather far from everyday experience, it might be useful to discuss the terms contained in the title before summarizing the results of the work.

Hydrodynamic theories describe systems, where local equilibrium is readily established. Water at room temperature is a good example of such a system. For all practical purposes, water is a fluid, even though we know it is made up of discrete particles (molecules). Equations in hydrodynamic theories are mathematical statements of conservation laws. An example of a conservation law is the Newton's second law, which states that momentum is conserved. Typical quantities relevant for a hydrodynamic description are, for example, densities, currents, and temperatures.

In this work, low temperatures are important to unmask quantum properties of the particles that the gases in question consist of. In particular, two different types of particles exist in nature, namely, *Bose* and Fermi particles. The different nature, also known as (quantum) particle statistics, results in a distinct behavior at low temperatures. While Fermi particles populate states available to them "individually", Bose particles tend to occupy states "collectively". An extreme example of the latter behavior is Bose-Einstein condensation, a process where almost all the particles of the system end up in the same quantum state. In contrast to this low-temperature behaviour, Fermi and Bose particles act very similarly at high temperatures, as they adhere to the laws of classical physics. It turns out that quantum physics can be readily explored in a controlled manner using atomic and molecular *gases*, and hence they are the subject of this thesis.

In high-school physics atoms and molecules are often depicted as points. However, these particles actually have some additional structure. A collective name for these structure features is *internal degrees of freedom*. In particular, we consider spin and electric dipole moment. Spin is a quantum-mechanical property of particles with no classical equivalent, though it is related to rotation. The reason behind magnetic behavior of various materials is the fact that electrons, atoms, and molecules have spin. Electric dipole moment is one of the properties that describe how anisotropic the charge distribution in an object is. For example, molecules that consist of two different atoms have a nonzero electric dipole moment, since the electrons spend more time close to some atoms than the others. Therefore, in an electric field particles with an electric dipole moment align with the field lines.

We now proceed to summarize the results of the work described in the individual chapters in a more technical manner. In the Introduction of the

thesis we discuss some key physical concepts that are developed throughout the later chapters. To make the discussion more concrete, we present a simple (mean-field) theory of the ferromagnetic spin-1/2 Bose gas and calculate its phase diagram. Furthermore, we describe two ultracold-atom experiments, as one of the goals of the theoretical work presented here is to motivate and give predictions for present and future experiments.

In Chapter 2 we put forward a hydrodynamic theory that describes simultaneously all phases of spinor (including spin-1/2) Bose gases and includes both geometric and dissipative coupling between superfluid, ferromagnetic order parameter and quasiparticles. As an application of that theory, we show that the topological Hall effect due to the presence of a skyrmion manifests itself in the collective modes of the system.

In Chapter 3 we consider the spin-1/2 Bose gas again, but this time in the miscible (as opposed to ferromagnetic) regime. We provide a detailed study of thermodynamic properties of the system within the Popov approximation. In combination with a hydrodynamic description, the thermodynamic properties allow us to quantitatively describe the long-wavelength collective modes of the gas. We also account for the damping of the spin modes by accounting for kinetic processes (spin drag) in a partially-condensed gas.

In Chapter 4 we explore the effect that a magnetic field, which depends on both position and momentum, has on the Bose-Einstein condensation temperature. We also consider a realistic laser-coupling scheme that could be used to produce such an effect. We find that the effect is small but nonzero, since the phase-space Berry curvature alters the density of states in the system.

Finally, in Chapter 5 we describe a Bose-Einstein condensate of dipolar molecules in a weak static electric field. We show that the system is described by a quantum rotor model for the macroscopic electric dipole moment of the molecular gas cloud. Furthermore, we demonstrate that a Bose-Einstein condensate of dipolar molecules is a ferroelectric material disordered by quantum fluctuations, and that many-body interactions lead to nematic phases not available to classical ferroelectrics.

SAMENVATTING

In deze scriptie worden theoretische aspecten van ultrakoude gassen verkend[1]. Aangezien de aangesneden onderwerpen tamelijk ver van de dagelijkse belevingswereld af staan, is het wellicht nutting eerst de verschillende termen in de titel toe lichten, alvorens met de samenvatting te beginnen.

Hydrodynamische theorieën beschrijven systemen waar lokaal evenwicht gemakkelijk bereikt wordt. Water bij kamertemperatuur is een goed voorbeeld van zo'n systeem. Wat de praktijk betreft is water een vloeistof, ook al weten we dat het op kleine schaal uit losse deeltjes (moleculen) bestaat. In hydrodynamische theorieën nemen vergelijkingen veelal de vorm van behoudswetten aan. Een voorbeeld van een behoudswet is de tweede wet van Newton, die stelt dat impuls behouden is in een geisoleerd systeem. Voor een hydrodynamische beschrijving van een systeem zijn dichtheden, stromen en temperaturen typische relevante grootheden. In dit proefschrift, zijn lage temperaturen belangrijk om het kwantumgedrag van de deeltjes die het gas opbouwen te ontwaren. In het bijzonder bestaan er twee verschillende soorten deeltjes in de natuur, *Bose*- and Fermideeltjes. De verschillende aard van deze soorten deeltjes, ook bekend als hun deeltjesstatistiek, resulteert in sterk verschillend gedrag bij lage temperaturen. Waar Fermideeltjes de verschillende toestanden in een systeem "individueel"bezetten, neigen Bosedeeltjes ernaar om toestanden "collectief"te bezetten. Een extreem voorbeeld van dit laatste gedrag is de vorming van een Bose-Einstein condensaat, waar het merendeel van de deeltjes in het systeem dezelfde toestand bezet. In tegenstelling gedragen Fermi- en Bosedeeltjes zich nagenoeg identiek bij hoge temperaturen, waar ze allebei de wetten van de klassieke fysica volgen. Het blijkt dat de kwantumfysica gemakkelijk en gecontroleerd onthult kan worden door het gebruik van koude *gassen* van atomen of moleculen.

Op de middelbare school leert men bij natuur- en scheikunde dat atomen en moleculen nagenoeg puntvormige objecten zijn. Echter, deze deeltjes hebben een fijnere structuur. De term *interne vrijheidsgraden* vangt de eigenschappen van deze fijnere structuur. In het bijzonder beschouwen we hier de spin en het elektrisch dipoolmoment van de deeltjes. Spin is een louter kwantummechanische eigenschap van deeltjes die in de klassieke natuurkunde geen equivalent heeft, hoewel het beschouwd kan worden als een vorm van rotatie. De oorsprong van het magnetische gedrag van verscheidene materialen ligt erin dat elektronen, atomen en ook moleculen spin hebben. Het elektrisch dipoolmoment is een van de maten voor anisotropie van de ladingsverdeling in een object. Zo heeft bijvoorbeeld een molecuul dat uit twee verschillende atomen bestaat een dipoolmoment, omdat de elektronen erin zich vaker bij

1 The Dutch translation of the summary was kindly provided by Anton Quelle.

het ene dan het andere atoom bevinden. Ten gevolge hiervan lijnt het dipoolmoment van een deeltje zich uit met een eventueel aangelegd elektrisch veld.

We geven nu een meer technische samenvatting van de resultaten die in de verscheidene hoofdstukken van dit werk gepresenteerd worden. In de Introductie van dit werk behandelen we enkele belangrijke fysische concepten die in de latere hoofdstukken verder uitgewerkt worden. Om de discussie conreet te houden presenteren we een eenvoudige theorie van het ferromagnetische spin-1/2 Bose gas en berekenen we het bijbehorende fasediagram. Bovendien beschrijven we twee experimenten met ultrakoude gasse, aangezien een van de doelen van dit theoretische werk het doen van voorspellingen over zulke experimenten is.

In Hoofdstuk 2 introduceren we een hydrodynamische theorie die simultaan alle fasen van een spinor (incluus spin-1/2) Bose gassen beschrijft. Verder bevat deze theorie zowel de geometrische als de dissipatieve koppeling tussen een supervloeistof, de ferromagnetische ordeparameter en de quasideeltjes. Om deze theorie toe te passen, later we zien dat het topologische Hall effect, veroorzaakt door de aanwezigheid van een skyrmion, zichzelf manifesteert in de collectieve oscillaties van het systeem.

In Hoofdstuk 3 beschouwen we wederom het spin-1/2 Bose gas, maar ditmaal in het mengbare (in tegenstelling tot het ferromagnetische) regime. We leveren een gedetailleerde beschrijving van de thermodynamische eigenschappen van het systeem binnen de Popovbenadering. In combinatie met de hydrodynamische beschrijving, kunnen we de thermodynamische eigenschappen gebruiken om de collectieve trillingen van het gas met lange golflengtes kwalitatief de beschrijven. We nemen hiermee ook de uitdemping van de spinoscillaties mee door kinetische processen (spinweerstand) in een gedeeltelijk gecondenseerd gas in acht.

In Hoofdstuk 4 verkennen we het effect dat een magnetisch veld, welke van zowel positie als impuls afhangt, heeft op de temperatuur van een Bose-Einstein condensaat. We beschouwen ook een realistische methode om zo'n condensaat aan een laser te koppelen die dit effect induceert. Het resulterende effect is klein, maar ongelijk nul, aangezien de Berrykromming in de faseruimte de toestandsdichtheid van het systeem beinvloedt.

Ten slotte beschrijven we in Hoofdstuk 5 een Bose-Einstein condensaat van dipolaire moleculen in een zwak, statisch elektrisch veld. We tonen aan dat dit systeem beschreven wordt door een kwantumrotormodel voor het macroscopische elektrisch dipoolmoment van een moleculaire gaswolk. Bovendien demonstreren we dat een Bose-Einstein condensaat van dipolaire moleculen een ferroelektrisch materiaal is waarin kwantumfluctuaties voor wanorde zorgen, en waarin veeldeeltjesinteracties leiden tot nematische fases die niet in de klassieke ferroelektrica voorkomen.

ACKNOWLEDGMENTS

I would like to thank Henk and Rembert for their excellent job as my supervisors. Besides teaching me physics in an inspiring manner, they have always been approachable and encouraging. Crucially, they were never reluctant to give me detailed guidance when I asked for it, and also complete freedom when I needed the latter. Seldom a PhD student is lucky enough to have such supervisors!

I would also like to thank the rest of the permanent staff (both supporting and academic) and also all my colleagues in the Institute for Theoretical Physics for the discussions we had over the years, as well as for a friendly and relaxed atmosphere in the institute. I have also met a number of remarkable people outside the institute throughout the four years of graduate schools, conferences and workshops. Even though the following list is undoubtedly incomplete, I would still like to explicitly acknowledge Alessandro, Andrew, Andrey, Anja, Anna, Anne, Anton, Arie-Willem, Aron, Artem, Bart, Benedetta, Bram, Carolin, Chiara, Chris, Chris, Daniel, Dražen, Drian, Emilio, Emily, Erik, Flavio, Gerasimos, Gijs, Giuseppe, Guido, György, Hai-Qing, Hedwig, Huseyin, Ivano, Jaap, Jan, Jasper, Javier, Jeffrey, Jenneke, Jiansen Zheng, Jildou, Joris, Jules, Kiril, Lei Liao, Leihua Liu, Maarten, Marc, Marcos, Martijn, Mathijs, Michiel, Mikhail, Morten, Natalia, Nava, Nick, Niklas, Oleksandr, Olga, Panos, Phil, Philipp, Pieter, Pietro, Piotr, Rakpong, Ralph, Riccardo, Rick, Roberto, Sandeep, Sela, Shima, Simone, Stefan, Stefano, Stijn, Tara, Tatjana, Thessa, Thomas, Ties, Tomas, Vaidas, Val, Vivian, Vladimir, Watse, Wilke, and Wouter. I am especially grateful to Anton and Arie-Willem for their help with Dutch translations, and to Roberto for popularizing my research in Chile.

I would like to thank my friends Andreas, Aurimas, Christine, Christoph, Franz, Gediminas, Goda, Ieva, Jokūbas, Julius, Justas, Kerstin, Kęstutis, Krzysztof, Liudas, Luís, Lukasz, Mantas, Marco, Martynas, Romas, Simonas, Vytautas, and Žygimantas in Vilnius and elsewhere for keeping in touch with me despite the physical distance. I thank my German officemates Andreas and Christoph for their support during the thesis-writing period in particular, and for entertaining distractions outside the office. I appreciate the cover of the thesis very much and thank Aurimas for designing it. My six-year stay in Utrecht was extremely rewarding primarily because of the time spent with Franz, Luís, and Marco. Thank you, guys!

The decision to continue my physics studies was very much inspired by the discussions with various physicists working in Lithuania. I am particularly thankful for the guidance by Prof. dr. J. Matukas and by Dr. T. Gajdosik

during my bachelor studies and beyond, as well as the recent interactions with Prof. dr. G. Juzeliūnas.

Lastly, but perhaps most importantly, I would like to thank my family for their unwavering support. It would have been infinitely harder to complete this work without their encouragement.

CURRICULUM VITAE

I was born on 23 February, 1987 in Vilnius, Lithuania. I attended Vytautas Magnus Gymnasium in Klaipėda, Lithuania where I graduated in July 2005 with honors. During the time in the secondary school, I spent the academic year 2003/04 in Ehrensvärdska Gymnasium in Karlskrona, Sweden, and also attended the correspondence physics school "Fotonas" at Šiauliai University.

I have subsequently attended Vilnius University, and obtained a BSc in Applied Physics in July 2009. My bachelor thesis "Canonical Quantization and Renormalization of the ABC Theory" was supervised by Dr. T. Gajdosik. During the studies, I have also contributed to low-frequency electrical noise research under Prof. dr. J. Matukas.

Since September 2009 I have been based in Utrecht, The Netherlands. I was awarded a MSc in Theoretical Physics with honors in August 2011. My master thesis "Molecules and Polarons in Extremely Imbalanced Fermi Mixtures" was supervised by Dr. J. E. Baarsma and Prof. dr. ir. H. T. C. Stoof. I was offered a PhD candidate position in September 2011 under the joint supervision of Dr. R. A. Duine and Prof. dr. ir. H. T. C. Stoof. This thesis is an account of the work that has been accomplished since then.

BIBLIOGRAPHY

[1] I. M. Khalatnikov, *An Introduction To The Theory of Superfluidity* (Westview Press, 2000).

[2] L. Landau, Phys. Rev. **60**, 356 (1941).

[3] E. L. Andronikashvili and Y. G. Mamaladze, Rev. Mod. Phys. **38**, 567 (1966).

[4] C. J. Pethick and H. Smith, *Bose-Einstein Condensation in Dilute Gases; 2nd ed.* (Cambridge Univ. Press, Cambridge, 2008).

[5] E. L. Andonikashvili, *Reflections on Liquid Helium* (American Institute of Physics, N. Y., 1989).

[6] A. Griffin, "Bose-Einstein Condensation in Atomic Gases," (IOS Press, Amsterdam, 1999) Chap. A Brief History of Our Understanding of BEC: From Bose to Beliaev.

[7] S. Balibar, Journal of Low Temperature Physics **146**, 441 (2007).

[8] H. T. C. Stoof, K. B. Gubbels, and D. B. M. Dickerscheid, *Ultracold Quantum Fields* (Springer, Dordrecht, 2009).

[9] E. Tiesinga, B. J. Verhaar, and H. T. C. Stoof, Phys. Rev. A **47**, 4114 (1993).

[10] C. Chin, R. Grimm, P. Julienne, and E. Tiesinga, Rev. Mod. Phys. **82**, 1225 (2010).

[11] R. van Gelderen and S. Wolters, *Itinerant Ferromagnetism in an Ultracold Atom Bose Gas*, Bachelor thesis, Utrecht University (2006).

[12] Q. Gu, K. Bongs, and K. Sengstock, Phys. Rev. A **70**, 063609 (2004).

[13] L. E. Sadler, J. M. Higbie, S. R. Leslie, M. Vengalattore, and D. M. Stamper-Kurn, Nature **443**, 312 (2006).

[14] L. E. Sadler, *Dynamics of a Spin 1 Ferromagnetic Condensate*, Ph.D. thesis, University of California, Berkeley (2006).

[15] K. M. R. van der Stam, R. Meppelink, J. M. Vogels, and P. van der Straten, Phys. Rev. A **75**, 031602 (2007).

[16] R. Meppelink, R. van Rooij, J. M. Vogels, and P. van der Straten, Phys. Rev. Lett. **103**, 095301 (2009).

[17] R. Meppelink, S. B. Koller, and P. van der Straten, Phys. Rev. A **80**, 043605 (2009).

[18] R. Meppelink, S. B. Koller, J. M. Vogels, H. T. C. Stoof, and P. van der Straten, Phys. Rev. Lett. **103**, 265301 (2009).

[19] H. T. C. Stoof, A. M. L. Janssen, J. M. V. A. Koelman, and B. J. Verhaar, Phys. Rev. A **39**, 3157 (1989).

[20] U. Gasser, C. Eisenmann, G. Maret, and P. Keim, ChemPhysChem **11**, 963 (2010).

[21] G. M. Bruun and D. R. Nelson, Phys. Rev. B **89**, 094112 (2014).

[22] S. Ospelkaus, K.-K. Ni, D. Wang, M. H. G. de Miranda, B. Neyenhuis, G. Quéméner, P. S. Julienne, J. L. Bohn, D. S. Jin, and J. Ye, Science **327**, 853 (2010).

[23] M. H. G. de Miranda, A. Chotia, B. Neyenhuis, D. Wang, G. Quéméner, S. Ospelkaus, J. L. Bohn, J. Ye, and D. S. Jin, Nat. Phys. **7**, 502 (2011).

[24] J.-y. Choi, S. Kang, S. W. Seo, W. J. Kwon, and Y.-i. Shin, Phys. Rev. Lett. **111**, 245301 (2013).

[25] J. J. Sakurai, *Modern Quantum Mechanics*, Revised ed. (Addison-Wesley Publishing Company, Reading, 1994).

[26] Q. Zhang and B. Wu, Phys. Rev. Lett. **97**, 190401 (2006).

[27] M. V. Berry, Proceedings of the Royal Society of London. A. Mathematical and Physical Sciences **392**, 45 (1984).

[28] K. Y. Bliokh, A. Niv, V. Kleiner, and E. Hasman, Nat. Photon. **2**, 748 (2008).

[29] A. Neubauer, C. Pfleiderer, B. Binz, A. Rosch, R. Ritz, P. G. Niklowitz, and P. Böni, Phys. Rev. Lett. **102**, 186602 (2009).

[30] Y. Li, N. Kanazawa, X. Z. Yu, A. Tsukazaki, M. Kawasaki, M. Ichikawa, X. F. Jin, F. Kagawa, and Y. Tokura, Phys. Rev. Lett. **110**, 117202 (2013).

[31] J. Dalibard, F. Gerbier, G. Juzeliūnas, and P. Öhberg, Rev. Mod. Phys. **83**, 1523 (2011).

[32] S. E. Barnes and S. Maekawa, Phys. Rev. Lett. **98**, 246601 (2007).

[33] R. A. Duine, Phys. Rev. B **77**, 014409 (2008).

[34] Y. Tserkovnyak and C. H. Wong, Phys. Rev. B **79**, 014402 (2009).

[35] S. A. Yang, G. S. D. Beach, C. Knutson, D. Xiao, Q. Niu, M. Tsoi, and J. L. Erskine, Phys. Rev. Lett. **102**, 067201 (2009).

[36] M. Hayashi, J. Ieda, Y. Yamane, J.-i. Ohe, Y. K. Takahashi, S. Mitani, and S. Maekawa, Phys. Rev. Lett. **108**, 147202 (2012).

[37] S. Mühlbauer, B. Binz, F. Jonietz, C. Pfleiderer, A. Rosch, A. Neubauer, R. Georgii, and P. Böni, Science **323**, 915 (2009).

[38] X. Z. Yu, N. Kanazawa, Y. Onose, K. Kimoto, W. Z. Zhang, S. Ishiwata, Y. Matsui, and Y. Tokura, Nat. Mater. **10**, 106 (2011).

[39] J. Foros, A. Brataas, Y. Tserkovnyak, and G. E. W. Bauer, Phys. Rev. B **78**, 140402 (2008).

[40] S. Zhang and S. S.-L. Zhang, Phys. Rev. Lett. **102**, 086601 (2009).

[41] J. Gómez, F. Perez, E. M. Hankiewicz, B. Jusserand, G. Karczewski, and T. Wojtowicz, Phys. Rev. B **81**, 100403 (2010).

[42] M. H. Anderson, J. R. Ensher, M. R. Matthews, C. E. Wieman, and E. A. Cornell, Science **269**, 198 (1995).

[43] K. B. Davis, M. O. Mewes, M. R. Andrews, N. J. van Druten, D. S. Durfee, D. M. Kurn, and W. Ketterle, Phys. Rev. Lett. **75**, 3969 (1995).

[44] T.-L. Ho, Phys. Rev. Lett. **81**, 742 (1998).

[45] T. Ohmi and K. Machida, Journal of the Physical Society of Japan **67**, 1822 (1998).

[46] A. Lamacraft, Phys. Rev. A **77**, 063622 (2008).

[47] R. Barnett, D. Podolsky, and G. Refael, Phys. Rev. B **80**, 024420 (2009).

[48] Y. Kawaguchi and M. Ueda, Physics Reports **520**, 253 (2012).

[49] D. M. Stamper-Kurn and M. Ueda, Rev. Mod. Phys. **85**, 1191 (2013).

[50] G. E. Volovik, Journal of Physics C: Solid State Physics **20**, L83 (1987).

[51] A. Stern, Phys. Rev. Lett. **68**, 1022 (1992).

[52] Y. Tserkovnyak, E. M. Hankiewicz, and G. Vignale, Phys. Rev. B **79**, 094415 (2009).

[53] R. A. Duine and H. T. C. Stoof, Phys. Rev. Lett. **103**, 170401 (2009).

[54] B. I. Halperin and P. C. Hohenberg, Phys. Rev. **188**, 898 (1969).

[55] J.-y. Choi, W. J. Kwon, and Y.-i. Shin, Phys. Rev. Lett. **108**, 035301 (2012).

[56] E. Yukawa and M. Ueda, Phys. Rev. A **86**, 063614 (2012).

[57] M. H. Anderson, J. R. Ensher, M. R. Matthews, C. E. Wieman, and E. A. Cornell, Science **269**, 198 (1995).

[58] C. C. Bradley, C. A. Sackett, J. J. Tollett, and R. G. Hulet, Phys. Rev. Lett. **75**, 1687 (1995).

[59] A. J. Leggett, Rev. Mod. Phys. **73**, 307 (2001).

[60] I. Bloch, J. Dalibard, and W. Zwerger, Rev. Mod. Phys. **80**, 885 (2008).

[61] S. Stringari, Phys. Rev. Lett. **77**, 2360 (1996).

[62] D. S. Jin, J. R. Ensher, M. R. Matthews, C. E. Wieman, and E. A. Cornell, Phys. Rev. Lett. **77**, 420 (1996).

[63] M.-O. Mewes, M. R. Andrews, N. J. van Druten, D. M. Kurn, D. S. Durfee, C. G. Townsend, and W. Ketterle, Phys. Rev. Lett. **77**, 988 (1996).

[64] N. Bogoljubov, Il Nuovo Cimento **7**, 794 (1958).

[65] A. Griffin, Phys. Rev. B **53**, 9341 (1996).

[66] J. O. Andersen, Rev. Mod. Phys. **76**, 599 (2004).

[67] J. M. Vogels, K. Xu, C. Raman, J. R. Abo-Shaeer, and W. Ketterle, Phys. Rev. Lett. **88**, 060402 (2002).

[68] A.-C. Voigt, M. Taglieber, L. Costa, T. Aoki, W. Wieser, T. W. Hänsch, and K. Dieckmann, Phys. Rev. Lett. **102**, 020405 (2009).

[69] L. A. Sidorenkov, M. K. Tey, R. Grimm, Y.-H. Hou, L. Pitaevskii, and S. Stringari, Nature **498**, 78 (2013).

[70] F. Schreck, L. Khaykovich, K. L. Corwin, G. Ferrari, T. Bourdel, J. Cubizolles, and C. Salomon, Phys. Rev. Lett. **87**, 080403 (2001).

[71] W. Colson and A. Fetter, Journal of Low Temperature Physics **33**, 231 (1978).

[72] T.-L. Ho and V. Shenoy, Journal of Low Temperature Physics **111**, 937 (1998).

[73] R. Graham and D. Walls, Phys. Rev. A **57**, 484 (1998).

[74] B. D. Esry and C. H. Greene, Phys. Rev. A **59**, 1457 (1999).

[75] D. V. Skryabin, Phys. Rev. A **63**, 013602 (2000).

[76] P. Tommasini, E. J. V. de Passos, A. F. R. de Toledo Piza, M. S. Hussein, and E. Timmermans, Phys. Rev. A **67**, 023606 (2003).

[77] B. Dalton and S. Ghanbari, Journal of Modern Optics **59**, 287 (2012).

[78] M. Abad and A. Recati, The European Physical Journal D **67**, 148 (2013).

[79] K. Anoshkin, Z. Wu, and E. Zaremba, Phys. Rev. A **88**, 013609 (2013).

[80] M. J. Edmonds, K. L. Lee, and N. P. Proukakis, Phys. Rev. A **91**, 011602 (2015).

[81] D. S. Hall, M. R. Matthews, J. R. Ensher, C. E. Wieman, and E. A. Cornell, Phys. Rev. Lett. **81**, 1539 (1998).

[82] G. Modugno, M. Modugno, F. Riboli, G. Roati, and M. Inguscio, Phys. Rev. Lett. **89**, 190404 (2002).

[83] S. Beattie, S. Moulder, R. J. Fletcher, and Z. Hadzibabic, Phys. Rev. Lett. **110**, 025301 (2013).

[84] C. Hamner, Y. Zhang, J. J. Chang, C. Zhang, and P. Engels, Phys. Rev. Lett. **111**, 264101 (2013).

[85] C.-H. Zhang and H. A. Fertig, Phys. Rev. A **75**, 013601 (2007).

[86] Z.-Q. Yu, Phys. Rev. A **90**, 053608 (2014).

[87] M.-S. Chang, Q. Qin, W. Zhang, L. You, and M. S. Chapman, Nat. Phys. **1**, 111 (2005).

[88] L. E. Sadler, J. M. Higbie, S. R. Leslie, M. Vengalattore, and D. M. Stamper-Kurn, Nature **443**, 312 (2006).

[89] M. W. Ray, E. Ruokokoski, S. Kandel, M. Mottonen, and D. S. Hall, Nature **505**, 657 (2014).

[90] U. Al Khawaja and H. Stoof, Nature **411**, 918 (2001).

[91] H. T. C. Stoof, E. Vliegen, and U. Al Khawaja, Phys. Rev. Lett. **87**, 120407 (2001).

[92] H. Pu, S. Raghavan, and N. P. Bigelow, Phys. Rev. A **63**, 063603 (2001).

[93] L. S. Leslie, A. Hansen, K. C. Wright, B. M. Deutsch, and N. P. Bigelow, Phys. Rev. Lett. **103**, 250401 (2009).

[94] J. Armaitis, H. T. C. Stoof, and R. A. Duine, Phys. Rev. Lett. **110**, 260404 (2013).

[95] Y. Kawaguchi, M. Nitta, and M. Ueda, Phys. Rev. Lett. **100**, 180403 (2008).

[96] M. Polini and G. Vignale, Phys. Rev. Lett. **98**, 266403 (2007).

[97] A. Sommer, M. Ku, G. Roati, and M. W. Zwierlein, Nature **472**, 201 (2011).

[98] S. B. Koller, A. Groot, P. C. Bons, R. A. Duine, H. T. C. Stoof, and P. van der Straten, ArXiv e-prints (2012), arXiv:1204.6143 [cond-mat.quant-gas] .

[99] S. O. Demokritov, V. E. Demidov, O. Dzyapko, G. A. Melkov, A. A. Serga, B. Hillebrands, and A. N. Slavin, Nature **443**, 430 (2006).

[100] R. E. Troncoso and A. S. Núñez, Annals of Physics **346**, 182 (2014).

[101] W. H. Bassichis, Phys. Rev. **134**, A543 (1964).

[102] D. M. Larsen, Annals of Physics **24**, 89 (1963).

[103] G. M. Falco, A. Pelster, and R. Graham, Phys. Rev. A **75**, 063619 (2007).

[104] T. D. Lee and C. N. Yang, Phys. Rev. **105**, 1119 (1957).

[105] T. D. Lee, K. Huang, and C. N. Yang, Phys. Rev. **106**, 1135 (1957).

[106] S. Knoop, T. Schuster, R. Scelle, A. Trautmann, J. Appmeier, M. K. Oberthaler, E. Tiesinga, and E. Tiemann, Phys. Rev. A **83**, 042704 (2011).

[107] S. Floerchinger and C. Wetterich, Phys. Rev. A **79**, 063602 (2009).

[108] T. Nikuni, E. Zaremba, and A. Griffin, Phys. Rev. Lett. **83**, 10 (1999).

[109] E. Zaremba, T. Nikuni, and A. Griffin, Journal of Low Temperature Physics **116**, 277 (1999).

[110] H. van Driel, R. Duine, and H. Stoof, Phys. Rev. Lett. **105**, 155301 (2010).

[111] R. Kittinaradorn, R. A. Duine, and H. T. C. Stoof, New Journal of Physics **14**, 055007 (2012).

[112] T. Nikuni and A. Griffin, Phys. Rev. A **63**, 033608 (2001).

[113] C. C. Ackerman, B. Bertman, H. A. Fairbank, and R. A. Guyer, Phys. Rev. Lett. **16**, 789 (1966).

[114] T. F. McNelly, S. J. Rogers, D. J. Channin, R. J. Rollefson, W. M. Goubau, G. E. Schmidt, J. A. Krumhansl, and R. O. Pohl, Phys. Rev. Lett. **24**, 100 (1970).

[115] E. Zaremba, Phys. Rev. A **57**, 518 (1998).

[116] D. Xiao, M.-C. Chang, and Q. Niu, Rev. Mod. Phys. **82**, 1959 (2010).

[117] N. Nagaosa, J. Sinova, S. Onoda, A. H. MacDonald, and N. P. Ong, Rev. Mod. Phys. **82**, 1539 (2010).

[118] E. van der Bijl and R. A. Duine, Phys. Rev. Lett. **107**, 195302 (2011).

[119] Y.-J. Lin, K. Jimenez-Garcia, and I. B. Spielman, Nature **471**, 83 (2011).

[120] P. Wang, Z.-Q. Yu, Z. Fu, J. Miao, L. Huang, S. Chai, H. Zhai, and J. Zhang, Phys. Rev. Lett. **109**, 095301 (2012).

[121] L. W. Cheuk, A. T. Sommer, Z. Hadzibabic, T. Yefsah, W. S. Bakr, and M. W. Zwierlein, Phys. Rev. Lett. **109**, 095302 (2012).

[122] N. Goldman, G. Juzeliūnas, P. Öhberg, and I. B. Spielman, Reports on Progress in Physics **77**, 126401 (2014).

[123] G. Sundaram and Q. Niu, Phys. Rev. B **59**, 14915 (1999).

[124] D. Xiao, J. Shi, and Q. Niu, Phys. Rev. Lett. **95**, 137204 (2005).

[125] F. Freimuth, R. Bamler, Y. Mokrousov, and A. Rosch, Phys. Rev. B **88**, 214409 (2013).

[126] M. Hillery, R. O'Connell, M. Scully, and E. Wigner, Physics Reports **106**, 121 (1984).

[127] T. Donner, S. Ritter, T. Bourdel, A. Ottl, M. Kohl, and T. Esslinger, Science **315**, 1556 (2007).

[128] B. M. Anderson, I. B. Spielman, and G. Juzeliūnas, Phys. Rev. Lett. **111**, 125301 (2013).

[129] Z.-F. Xu, L. You, and M. Ueda, Phys. Rev. A **87**, 063634 (2013).

[130] C. Ospelkaus, S. Ospelkaus, L. Humbert, P. Ernst, K. Sengstock, and K. Bongs, Phys. Rev. Lett. **97**, 120402 (2006).

[131] K.-K. Ni, S. Ospelkaus, M. H. G. de Miranda, A. Pe'er, B. Neyenhuis, J. J. Zirbel, S. Kotochigova, P. S. Julienne, D. S. Jin, and J. Ye, Science **322**, 231 (2008).

[132] C.-H. Wu, J. W. Park, P. Ahmadi, S. Will, and M. W. Zwierlein, Phys. Rev. Lett. **109**, 085301 (2012).

[133] T. Lahaye, C. Menotti, L. Santos, M. Lewenstein, and T. Pfau, Reports on Progress in Physics **72**, 126401 (2009).

[134] L. D. Carr, D. DeMille, R. V. Krems, and J. Ye, New Journal of Physics **11**, 055049 (2009).

[135] R. Krems, B. Friedrich, and W. Stwalley, *Cold Molecules: Theory, Experiment, Applications* (Taylor & Francis, 2010).

[136] T. Koch, T. Lahaye, J. Metz, B. Frohlich, A. Griesmaier, and T. Pfau, Nat. Phys. **4**, 218 (2008).

[137] R. Heidemann, U. Raitzsch, V. Bendkowsky, B. Butscher, R. Löw, and T. Pfau, Phys. Rev. Lett. **100**, 033601 (2008).

[138] M. Lu, N. Q. Burdick, S. H. Youn, and B. L. Lev, Phys. Rev. Lett. **107**, 190401 (2011).

[139] A. Griesmaier, J. Werner, S. Hensler, J. Stuhler, and T. Pfau, Phys. Rev. Lett. **94**, 160401 (2005).

[140] S. E. Pollack, D. Dries, M. Junker, Y. P. Chen, T. A. Corcovilos, and R. G. Hulet, Phys. Rev. Lett. **102**, 090402 (2009).

[141] K. Aikawa, A. Frisch, M. Mark, S. Baier, A. Rietzler, R. Grimm, and F. Ferlaino, Phys. Rev. Lett. **108**, 210401 (2012).

[142] G. Pupillo, A. Micheli, H. P. Büchler, and P. Zoller, "Cold Molecules: Theory, Experiment, Applications," Chap. Condensed Matter Physics with Cold Polar Molecules, in [135] (2010).

[143] C.-H. Lin, Y.-T. Hsu, H. Lee, and D.-W. Wang, Phys. Rev. A **81**, 031601 (2010).

[144] C. J. Pethick and H. Smith, *Bose-Einstein Condensation in Dilute Gases; 2nd ed.* (Cambridge Univ. Press, Cambridge, 2008).

[145] C. K. Law, H. Pu, and N. P. Bigelow, Phys. Rev. Lett. **81**, 5257 (1998).

[146] S. Giovanazzi, A. Görlitz, and T. Pfau, Phys. Rev. Lett. **89**, 130401 (2002).

[147] S. Giovanazzi, P. Pedri, L. Santos, A. Griesmaier, M. Fattori, T. Koch, J. Stuhler, and T. Pfau, Phys. Rev. A **74**, 013621 (2006).

[148] S. Yi and H. Pu, in *Electromagnetic, Magnetostatic, and Exchange-Interaction Vortices in Confined Magnetic Structures*, edited by E. O. Kamenetskii (Research Signpost, India, 2009).

[149] S. Yi, L. You, and H. Pu, Phys. Rev. Lett. **93**, 040403 (2004).

[150] R. Barnett, J. D. Sau, and S. Das Sarma, Phys. Rev. A **82**, 031602 (2010).

[151] J. Ma, X. Wang, C. Sun, and F. Nori, Physics Reports **509**, 89 (2011).

[152] C. Eberlein, S. Giovanazzi, and D. H. J. O'Dell, Phys. Rev. A **71**, 033618 (2005).

[153] S. Yi and L. You, Phys. Rev. A **61**, 041604 (2000).

[154] S. Yi and L. You, Phys. Rev. A **63**, 053607 (2001).

[155] D. C. E. Bortolotti, S. Ronen, J. L. Bohn, and D. Blume, Phys. Rev. Lett. **97**, 160402 (2006).

[156] S. Ronen, D. C. E. Bortolotti, D. Blume, and J. L. Bohn, Phys. Rev. A **74**, 033611 (2006).